May 2015

Gravitational Waves from Rotating Neutron Stars and Compact Binary Systems

Leslie Wade
University of Wisconsin-Milwaukee

GRAVITATIONAL WAVES FROM ROTATING NEUTRON STARS AND COMPACT BINARY SYSTEMS

by

Leslie E Wade IV

A Dissertation Submitted in
Partial Fulfillment of the
Requirements for the degree of

Doctor of Philosophy
in Physics

at
The University of Wisconsin–Milwaukee
May 2015

ABSTRACT

GRAVITATIONAL WAVES FROM ROTATING NEUTRON STARS AND COMPACT BINARY SYSTEMS

The University of Wisconsin–Milwaukee, April 2015
Under the Supervision of Professors Xavier Siemens and Jolien Creighton

It is widely anticipated that the first direct detections of gravitational waves will be made by advanced gravitational-wave detectors, such as the two Laser Interferometer Gravitational-wave Observatories (LIGO) and the Virgo interferometer. In preparation for the advanced detector era, I have worked on both detection and post-detection efforts involving two gravitational wave sources: isolated rotating neutron stars (NSs) and compact binary coalescences (CBCs). My dissertation includes three main research projects: 1) a population synthesis study assessing the detectability of isolated NSs, 2) a CBC search for intermediate-mass black-hole binaries (IMBHBs), and 3) new methods for directly measuring the neutron-star (NS) equation of state (EOS).

Direct detections of gravitational waves will enrich our current astrophysical knowledge. One such contribution will be through population synthesis of isolated NSs. My collaborators and I show that advanced gravitational-wave detectors can be used to constrain the properties of the Galactic NS population. Gravitational wave detections can also shine light on a currently mysterious astrophysical object: intermediate mass black holes. In developing the IMBHB search, we performed a mock data challenge where signals with total masses up to a few hundred solar masses were injected into recolored data from LIGOs sixth science run. Since this is the first time a matched filter search has been developed to search for IMBHBs, I discuss what was learned during the mock data challenge and how we plan to improve the search going forward. The final aspect of my dissertation focuses on important post-detection science. I present results for a new method of directly measuring the NS EOS. This is done by estimating the parameters of a 4-piece polytropic EOS model that matches theoretical EOS candidates to a few percent. We show that advanced detectors will be capable of measuring the NS radius to within a

kilometer for stars with canonical masses. However, this can only be accomplished with binary NS waveform models that are accurate to the rich EOS physics that happens near merger. We show that the waveforms typically used to model binary NS systems result in unavoidable systematic error that can significantly bias the estimation of the NS EOS.

TABLE OF CONTENTS

LIST OF FIGURES

LIST OF TABLES

ACKNOWLEDGMENTS

I'd like to thank my wife Maddie for all the help and support she has given me throughout grad school and while writing this dissertation. I have relied upon and benefitted from Maddie's insight and encouragement countless times. I love you Maddie, thanks for everything!

I'd like to thank my daughter Ruth for providing relief from dissertation writing and stress. She may not realize it, but our afternoons together kept me from losing my mind! I'm so grateful to have Ruth in my life.

I'd like to thank my parents and mother-in-law for taking care of us, Ruth, and our dogs when we needed it most. Our trip to my parents' house was essential to finishing a draft of my dissertation, and my mother-in-law's weekend trip to Milwaukee before our defense kept me from embarrassing myself too badly during my defense. Thank you so much!

I'd like to thanks my advisors Jolien Creighton and Xavier Siemens. Your patience and insight have been invaluable. Thank you both for preparing me to accept a faculty position at Kenyon.

Lastly, I'd like to thank several professors, post-docs, and grad students that have collaborated with me or sacrificed their research time to help me. David Kaplan, Ilya Mandel, Patrick Brady, Ben Lackey, Chris Pankow, Evan Ochsner, Sarah Caudill, Laleh Sadeghian, Richard O'Shaughnessy, Vivien Raymond, Will Farr, Tyson Littenberg, Ben Farr, Brian Vlcek, Sydney Chamberlin, Tom Linz, Alex Urban, and Justin Ellis – thank you all!

Chapter 1

Introduction

Einstein's theory of general relativity (GR) reimagines gravity as a consequence of the curvature of spacetime caused by matter rather than an attractive force between objects with mass. Einstein realized that spacetime was not just a platform for but a participant in matter dynamics [2]. His field equations relate the motion of matter to the curvature of spacetime caused by matter. Essentially, GR explains objects falling under the "pull" of gravity and objects in orbit as merely those objects following the straightest possible path in curved spacetime.

One of the natural products of this new understanding of gravity is the existence of gravitational waves (GWs), which are oscillations in spacetime that carry information about changes to gravitating sources, thereby preserving causality as required by special relativity. As one might expect due to the relative weakness of the gravitational interaction, GWs and their effects are mostly unnoticeable. The only sources of GWs whose effects are large enough to notice are astrophysical. For example, the emission of GWs from binary neutron stars results in observable changes to the binary's orbital evolution. Most famously, the Hulse-Taylor pulsar's orbit is decaying at precisely the rate that GR predicts for orbital decay due to GW emission [3]. This discovery provides strong evidence for the existence of GWs and won Hulse and Taylor the Nobel Prize in 1993.

Though the effects of GWs have clearly been observed, GWs have yet to be directly detected. Kilometer-scale ground-based interferometers have been built in an effort to make the first direct GW detections. The United States is home to the two most sensitive

GW detectors, called the Laser Interferometric Gravitational-wave Observatory, or LIGO for short. One of the LIGO sites is located in Hanford, WA, and the other LIGO site is in Livingston, LA. The initial LIGO configuration referred to as iLIGO was online from 2002-2007 before it was upgraded to an enhanced configuration referred to as eLIGO, which was online from 2009-2010. Though no GWs were detected in these science runs, interesting upper limits were placed on certain GW sources [4–7]. The LIGO instruments were again upgraded to an advanced configuration referred to as aLIGO, which will be performing its first observing run in Fall 2015. It is widely anticipated that the first direct GW detections will be made by the time the LIGO instruments reach design sensitivity c. 2019 [8], and likely much sooner!

The most promising GW sources for aLIGO are compact binary coalescences (CBC) involving black holes (BHs) and/or neutron stars (NSs). A CBC system consists of two dense and massive astrophysical objects that are caught in orbit and continuously lose energy to GWs before eventually colliding. Theoretical models of the form of a CBC GW, or its waveform, depend on a systems source parameters. Such parameters include, but are not limited to, the mass and spin of each component in the binary, the distance between the binary and each detector, and the relative orientation of the binary to each detector. By adjusting the values of the model's source parameters, the form of the modeled wave will change.

To search for CBC signals in detector data, we filter the data through a bank of theoretically produced gravitational waveform models and calculate how well each template matches the data. We can then estimate the probability that a GW signal exists in the data.

Analysis does not end at a detection. Instead, we hope to use GW signals to study their astrophysical sources. After a detection is made, the data around that time can be more thoroughly analyzed to find the most probable combinations of waveform parameters that resulted in the detected signal. This process is called parameter estimation, and is discussed in more detail in Sec. 4.3. GW observatories will work like another type of telescope for studying astrophysical objects.

Several other ground-based interferometers have been built for detecting GWs. Most

notably, the VIRGO detector located in Tuscany, Italy can reach sensitivities comparable to the LIGO detectors. It too is undergoing upgrades to an advanced configuration, called Advanced VIRGO. Advanced VIRGO will play an important role in GW detection and parameter estimation because it can be used to increase the significance of events for detection as well as better localize sources in the sky resulting in improved parameter estimation.

In Ch. 1, we introduce the theory behind GWs and briefly describe ground-based interferometric detectors. In Ch. 2, we discuss GW emission from another source: isolated rotating NSs. Isolated neutron stars that are not axisymmetric will continuously emit GWs as they rotate. In this chapter, we discuss a project in which we simulated the Milky Way's NS population to determine how well advanced detectors can constrain certain properties of NSs. In Ch. 3, we discuss development for a CBC search for intermediate-mass BH binaries (IMBHBs). Due to the improved low-frequency sensitivity, more massive binary systems such as IMBHBs that merge at relatively low frequencies might be detectable with advanced detectors. In Ch. 4, we outline a parameter estimation approach for estimating the size of tidal effects in merging NSs, which is intimately related to the NS equation of state (EOS). In addition, we outline the statistical and systematic errors associated with such measurements. We then improve upon this approach in Ch. 5 by reparameterizing from tidal parameters to EOS parameters in order to make direct EOS measurements. This approach has the added benefit of being able to combine information from many BNS detections as well as include any observational or physical restrictions on the NS EOS. We end with a discussion in Ch. 6.

In this chapter, we briefly review the major pieces of gravitational-wave theory. In Sec. 1.1, we start with how GWs fall out of Einstein's equations, then describe how GWs affect matter and can be detected by an interferometer, and finish with how GWs are sourced. In Sec. 1.2, we discuss two types of gravitating systems: isolated rotating neutron stars and compact binary coalescences. In particular, we discuss a model for their waveform. We finish by briefly discussing ground-based interferometers and their properties in Sec. 1.3.

1.1 Gravitational wave review[1]

The Einstein field equations

$$G_{\alpha\beta} = \frac{8\pi G}{c^4} T_{\alpha\beta}, \tag{1.1.1}$$

which distinguish GR from other metric theories of gravity, relate the curvature of spacetime to the source of the curvature, which is matter. Here, $G_{\alpha\beta}$ is the Einstein tensor

$$G_{\alpha\beta} = R_{\alpha\beta} - \frac{1}{2} g_{\alpha\beta} R, \tag{1.1.2}$$

where the Ricci tensor $R_{\alpha\beta} = g^{\mu\nu} R_{\alpha\mu\beta\nu} = R_{\alpha\mu\beta}{}^{\mu}$, the Ricci scalar $R = g^{\mu\nu} R_{\mu\nu} = R_{\mu}{}^{\mu}$, and $R_{\alpha\beta\gamma\delta}$ is the Riemann curvature tensor. The metric tensor (or the metric for short) defines the distance s between two points in spacetime via

$$ds^2 = g_{\mu\nu} dx^{\mu} dx^{\nu}. \tag{1.1.3}$$

It is therefore fundamental to any metric theory of gravity, such as GR, since it defines the entire geometry of the spacetime. For flat spacetime in rectilinear coordinates, the metric is:

$$g_{\alpha\beta} = \eta_{\alpha\beta} = \begin{bmatrix} -c^2 & 0 & 0 & 0 \\ 0 & 1 & 0 & 0 \\ 0 & 0 & 1 & 0 \\ 0 & 0 & 0 & 1 \end{bmatrix}. \tag{1.1.4}$$

The matter stress energy tensor $T_{\alpha\beta}$ has the following parts:

$$T^{tt} = \rho \tag{1.1.5}$$

$$T^{ti} = T^{it} = J^i \tag{1.1.6}$$

$$T^{ij} = S^{ij}, \tag{1.1.7}$$

where ρ is the mass density, J^i are the components of the momentum density, and S^{ij} are the components of the stress tensor. Another way of writing this is

[1] The entirety of this section closely follows Refs. [2] and [9].

$$T^{\alpha\beta} = \begin{bmatrix} \rho & \leftarrow & J^i & \rightarrow \\ \uparrow & \nwarrow & \uparrow & \nearrow \\ J^i & \leftarrow & S^{ij} & \rightarrow \\ \downarrow & \swarrow & \downarrow & \searrow \end{bmatrix}.$$

1.1.1 Linearized gravity

Assuming the gravitational field is weak, which is referred to as linearized gravity, the metric $g_{\alpha\beta}$ is just a perturbation $h_{\alpha\beta}$ to the flat-space metric $\eta_{\alpha\beta}$:

$$g_{\alpha\beta} = \eta_{\alpha\beta} + h_{\alpha\beta}. \tag{1.1.8}$$

Under this assumption and only keeping terms to first order, the Einstein field equations become:

$$-\Box\bar{h}_{\alpha\beta} - \eta_{\alpha\beta}\frac{\partial^2\bar{h}^{\mu\nu}}{\partial x^\mu \partial x^\nu} + \frac{\partial^2\bar{h}^{\mu}_{\beta}}{\partial x^\alpha \partial x^\mu} + \frac{\partial^2\bar{h}^{\mu}_{\alpha}}{\partial x^\mu \partial x^\beta} \approx \frac{16\pi G}{c^4}T_{\alpha\beta}, \tag{1.1.9}$$

where $\Box = \eta^{\mu\nu}\partial^2/(\partial x^\mu \partial x^\nu)$ is the d'Alembertian operator and $\bar{h}_{\alpha\beta} = h_{\alpha\beta} - \frac{1}{2}\eta_{\alpha\beta}h$ is the trace-reversed metric perturbation, where $h = \eta^{\mu\nu}h_{\mu\nu} = h_{\mu}{}^{\mu}$. By moving to another gauge in which the divergence of the trace-reversed metric is zero ($\partial\bar{h}^{\mu\alpha}/\partial x^\mu = 0$), which is called the Lorenz gauge, the Einstein field equations simply become:

$$-\Box\bar{h}_{\alpha\beta} \approx \frac{16\pi G}{c^4}T_{\alpha\beta}. \tag{1.1.10}$$

It can be shown that a Lorenz gauge can always be found.

1.1.2 Linearized gravity + vacuum spacetime = gravitational waves

In a spacetime in which there is no matter, the linearized vacuum Einstein field equations in the Lorenz gauge become:

$$\Box\bar{h}_{\alpha\beta} \approx 0. \tag{1.1.11}$$

Such a spacetime would be a good approximation to being hit by weak GWs in an otherwise empty area of spacetime far from a gravitating source. A solution to Eq. (1.1.11) is the plane wave solution, and the Lorenz condition $\partial\bar{h}^{\mu\alpha}/\partial x^\mu = 0$ ensures that the plane wave is transverse, meaning that its amplitude is perpendicular to its propagation.

There is enough gauge freedom left within the Lorenz gauge to choose a gauge that also makes the trace-reversed metric perturbation traceless ($\delta^{ij}h_{ij} = 0$) and completely spatial ($h_{\alpha t} = 0$), and this is called the transverse traceless (TT) gauge. In the TT gauge, $\bar{h}_{\alpha\beta} = h_{\alpha\beta} \equiv h^{\mathrm{TT}}_{\alpha\beta}$ since the perturbation is traceless. Additionally, if we align the z-axis along the direction of propagation of the transverse plane wave, Eq. (1.1.11) indicates that the components of the perturbation must be functions of the retarded time $t - z/c$. Therefore, in the TT gauge, the solution of the vacuum Einstein field equations for the metric perturbation are transverse plane waves traveling at the speed of light, and these are called gravitational waves.

The TT gauge reveals that GWs only have two polarizations in GR. For a GW traveling in the z-direction, the Lorenz condition (now $\partial\bar{h}^{ij}/\partial x^i = 0$ since the perturbation is purely spatial) implies that $\partial\bar{h}^{zi}/\partial x^z = 0$, meaning $\bar{h}_{zi}(t - z/c) = h_{zi}(t - z/c) = h^{\mathrm{TT}}_{zi}(t - z/c) =$ constant. We can take this constant to be zero. The non-zero components are h^{TT}_{xx}, h^{TT}_{xy}, h^{TT}_{yx}, and h^{TT}_{yy}. Since the perturbation is symmetric,

$$h^{\mathrm{TT}}_{xy} = h^{\mathrm{TT}}_{yx} \equiv h_{\times}(t - z/c), \tag{1.1.12}$$

and since the perturbation is traceless and $h^{\mathrm{TT}}_{zz} = 0$,

$$h^{\mathrm{TT}}_{xx} = -h^{\mathrm{TT}}_{yy} \equiv h_{+}(t - z/c). \tag{1.1.13}$$

We refer to these two polarizations as "plus" and "cross" because of how they affect masses, which can be seen in Fig. 1 and is touched on in the following subsection.

1.1.3 How GWs affect test masses (and detector)[2]

The equations of motion for objects under the influence of gravity are the geodesic equations

$$\frac{d^2x^\alpha}{d\tau^2} = -\Gamma^\alpha_{\mu\nu}\frac{dx^\mu}{d\tau}\frac{dx^\nu}{d\tau}, \tag{1.1.14}$$

where τ is the proper time. The coordinate acceleration can be found by taking coordinate time derivatives instead of proper time derivatives. Assuming linearized gravity with the non-flat components of the metric dominated by a GW in the TT gauge, and

[2]The example used in this subsection is from Ref. [2]

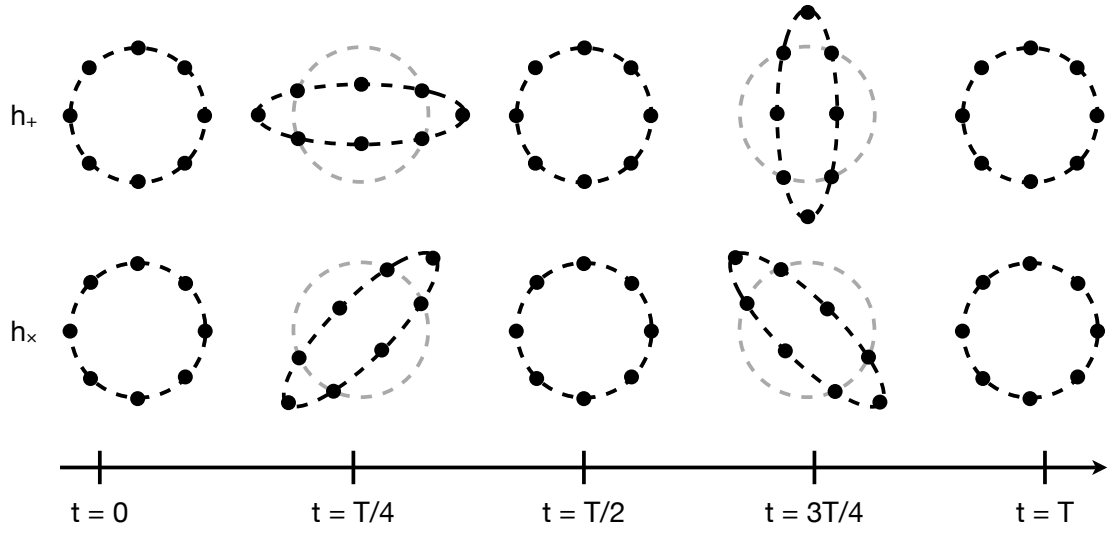

Figure 1 : GWs in GR have two polarizations: plus (top) and cross (bottom). The proper separations of particles in a ring will be affected by a GW traveling into the page as depicted, where the axis is time and T is the period of the GW.

assuming non-relativistic motion for a test-particle undergoing a coordinate acceleration, Eq. (1.1.14) reduces to

$$\frac{d^2x^i}{dt^2} = -\Gamma^i_{tt} = 0. \tag{1.1.15}$$

This does not mean that test particles are unaffected by GWs. It just means that the coordinate acceleration of test particles is zero in the TT gauge. This means that the TT gauge is a gauge whose coordinates move with the GW, thus conserving the coordinate separation between freely falling test particles.

To determine the proper separation between two test particles in the presence of a GW, consider two test particles located on the x-axis at $z = 0$ and separated by coordinate distance L_c. The proper distance between the two freely falling test particles is

$$\begin{aligned} L(t) &= \int_0^{L_c} \sqrt{g_{xx}}\, dx && (1.1.16)\\ &= \int_0^{L_c} \sqrt{1 + h^{TT}_{xx}(t)}\, dx && (1.1.17)\\ &\approx \left[1 + \frac{1}{2}h^{TT}_{xx}(t)\right] \int_0^{L_c} dx && (1.1.18)\\ &= L_c \left[1 + \frac{1}{2}h^{TT}_{xx}(t)\right]. && (1.1.19) \end{aligned}$$

The above integral was so easily computed because the coordinate separation does not

change over time for freely falling particles in the TT gauge. While GWs do not affect coordinate separations between freely falling particles, they do affect proper separations. Therefore, GWs can be directly observed by measuring the proper distance between freely falling test masses, which can be accomplished with an interferometer.

To see this, consider a simple Michelson interferometer whose arms are aligned with the x-axis and y-axis of a rectilinear coordinate system. Imagine that the beam splitter is located at the origin of the coordinate system, and the two mirrors are located at $(x = L, y = 0, z = 0)$ and $(x = 0, y = L, z = 0)$. We refer to the length of the interferometer arm aligned with the x-axis as L_x and the length of the interferometer aligned with the y-axis as L_y. The end mirrors can be considered to be the test masses of the previous example, so the change in the proper separation between the end mirror and the beam splitter along the x-axis is

$$\frac{\Delta L_x(t)}{L} \approx \frac{1}{2} h_{xx}^{\mathrm{TT}}(t) \approx \frac{1}{2} h_+(t). \tag{1.1.20}$$

Likewise, the change in the proper separation between the end mirror and the beam splitter along the y-axis is

$$\frac{\Delta L_y(t)}{L} \approx \frac{1}{2} h_{yy}^{\mathrm{TT}}(t) \approx -\frac{1}{2} h_+(t). \tag{1.1.21}$$

Therefore, the difference in the arm lengths is

$$\frac{\Delta L(t)}{L} = \frac{\Delta L_x(t) - \Delta L_y(t)}{L} \approx h_+(t). \tag{1.1.22}$$

The quantity $\Delta L/L$ is called the GW strain.

GWs from astrophysical sources will not be perfectly aligned with an interferometer. Instead, the interferometer will be affected by some linear combination of the plus and cross polarizations of the GW, which will depend on its sky location and relative orientation to the instrument. In general, the GW strain is

$$\frac{\Delta L}{L} \approx h(t) = F_+(\alpha, \delta, \psi, t) h_+(t; \iota) + F_\times(\alpha, \delta, \psi, t) h_\times(t; \iota), \tag{1.1.23}$$

where the source's sky position is given in terms of the right ascension α and declination δ, ι is the inclination angle between the separation vector between the GW source and the detector and a vector perpendicular to the polarization plane, and the polarization

angle ψ is the angle at which the polarization axis is rotated about the separation vector. F_+ and $F_\times$ are called the antenna patterns.

1.1.4 How GWs are generated

The source for GWs is the matter term on the right-hand side of the linearized Einstein field equations

$$\Box\bar{h}_{\alpha\beta} = -\frac{16\pi G}{c^4}T_{\alpha\beta} + O(h^2), \tag{1.1.24}$$

where the higher-order terms $O(h^2)$ had not been previously indicated in Eq. (1.1.10). The exact field equations can be written in terms of the effective stress-energy tensor $\tau^{\alpha\beta}$ which treats the $O(h^2)$ terms as additional source terms to the linear perturbation:

$$\Box\bar{h}_{\alpha\beta} = -\frac{16\pi G}{c^4}\tau_{\alpha\beta}. \tag{1.1.25}$$

The solution to $\bar{h}_{\alpha\beta}$ for the exact field equations can be found using a Green's function, and the solution is

$$\bar{h}_{\alpha\beta}(t,\vec{x}) = \frac{4G}{c^4}\int \frac{\tau_{\alpha\beta}(t-|\vec{x}-\vec{x}'|/c,\vec{x}')}{|\vec{x}-\vec{x}'|}\,d^3\vec{x}'. \tag{1.1.26}$$

This integral simplifies when analyzed in the "far zone", which is where GW detectors are located relative to astrophysical sources. The properties of the far zone are that the size of the source R is much less than the GW wavelength λ, which is much less than the distance to the GW source D. In the far zone and exploiting an identity of the effective stress energy tensor, Eq. (1.1.26) becomes

$$\bar{h}_{ij}(t,\vec{x}) \approx \frac{2G}{c^4 D}\ddot{I}_{ij}(t-D/c), \tag{1.1.27}$$

where the quadrupole tensor is defined

$$I_{ij}(t) = \int x_i x_j \tau^{00}(t,\vec{x})\,d^3\vec{x}. \tag{1.1.28}$$

In the TT gauge, the far-zone solution for the metric perturbation is

$$h_{ij}^{\mathrm{TT}}(t) \approx \frac{2G}{c^4 D}\ddot{I}_{ij}^{\mathrm{TT}}(t-D/c). \tag{1.1.29}$$

Here, the transverse-traceless quadrupole tensor is

$$I_{ij}^{\mathrm{TT}}(t) = P_{ik}I^{kl}P_{lj} - \frac{1}{2}P_{ij}P_{kl}I^{kl}, \tag{1.1.30}$$

the transverse projection operator is

$$P_{ij} = \delta_{ij} - \hat{n}_i \hat{n}_j, \tag{1.1.31}$$

and the unit vector in the direction of propagation is $\hat{n}_i = x_i/D$.

1.1.5 Energy and angular momentum in GWs

There are two other useful relationships to review: the GW luminosity and the amount of angular momentum radiated by a gravitating system. The GW stress-energy is given by

$$T^{\rm GW}_{\alpha\beta} = \frac{c^4}{32\pi G} \left\langle \frac{\partial h^{ij}_{\rm TT}}{\partial x^\alpha} \frac{\partial h^{\rm TT}_{ij}}{\partial x^\beta} \right\rangle. \tag{1.1.32}$$

The GW luminosity can be calculated from this quantity and is

$$L = -\frac{dE}{dt} = \frac{1}{5}\frac{G}{c^5} \left\langle \dddot{\mathcal{I}}_{ij} \dddot{\mathcal{I}}^{ij} \right\rangle, \tag{1.1.33}$$

where

$$\mathcal{I}_{ij} = \int \left(x_i x_j - \frac{1}{3} r^2 \delta_{ij} \right) \tau^{00}(t, \vec{x}) d^3\vec{x}. \tag{1.1.34}$$

Note that $\mathcal{I}^{\rm TT}_{ij} = I^{\rm TT}_{ij}$ since the only difference between the two quantities is that $\mathcal{I}_{ij}$ is traceless. From this, the amount of angular momentum radiated is

$$\frac{dJ_i}{dt} = -\frac{2}{5}\frac{G}{c^5} \epsilon_{ijk} \left\langle \ddot{\mathcal{I}}^{jl} \dddot{\mathcal{I}}^{k}_{l} \right\rangle, \tag{1.1.35}$$

where

$$\epsilon_{ijk} = \begin{cases} +1 & \text{if } (i,j,k) \text{ is } (1,2,3), (3,1,2), \text{or } (2,3,1) \\ -1 & \text{if } (i,j,k) \text{ is } (3,2,1), (1,3,2), \text{or } (2,1,3) \\ 0 & \text{if } i=j, i=k, \text{or } j=k \end{cases}. \tag{1.1.36}$$

1.2 A couple astrophysical GW sources

(The entirety of this section closely follows [9].)

For my Ph.D. research, I have considered two types of GW sources: isolated, rotating NSs and CBCs. In general, the GW strain as measured in an interferometric detector is

$$h = F_+ h_+ + F_\times h_\times, \tag{1.2.1}$$

The antenna patterns just depend on the source's position in the sky and its relative orientation to the detector. This section reviews the form of the two GW polarizations h_+ and $h_\times$ for isolated, rotating NSs and CBC systems.

1.2.1 Isolated rotating NS waveform and frequency evolution

An isolated, rotating NS can be modeled by a rotating ellipsoid. If the ellipsoid is not axisymmetric, it will emit GWs because its quadrupole will change over time. The far-zone solution to the linearized Einstein field equations is

$$h_{ij}^{\mathrm{TT}}(t) = \frac{2G}{c^4 D}\ddot{I}_{ij}^{\mathrm{TT}}(t - D/c). \tag{1.2.2}$$

The second time derivative of the transverse-traceless quadrupole tensor for an ellipsoid rotating about the z-axis with rotational frequency ν observed at an inclination ι is

$$\ddot{I}_{ij}^{\mathrm{TT}} = 8\pi^2 \epsilon I \nu^2 \begin{bmatrix} -\left(\frac{1+\cos^2\iota}{2}\right)\cos(4\pi\nu t) & \cos\iota\sin(4\pi\nu t) & 0 \\ \cos\iota\sin(4\pi\nu t) & \left(\frac{1+\cos^2\iota}{2}\right)\cos(4\pi\nu t) & 0 \\ 0 & 0 & 0 \end{bmatrix},$$

where the ellipticity $\epsilon = (I_1 - I_2)/I$, $I_3 \equiv I$, and I_1, I_2, and I_3 are the principle axes of inertia. Therefore, the GW takes the form

$$h_{ij}^{\mathrm{TT}} = \frac{16\pi^2 G\epsilon I\nu^2}{c^4 D} \begin{bmatrix} -\left(\frac{1+\cos^2\iota}{2}\right)\cos(4\pi\nu t) & \cos\iota\sin(4\pi\nu t) & 0 \\ \cos\iota\sin(4\pi\nu t) & \left(\frac{1+\cos^2\iota}{2}\right)\cos(4\pi\nu t) & 0 \\ 0 & 0 & 0 \end{bmatrix},$$

and the two polarizations are

$$h_+(t) = -\frac{16\pi^2 G\epsilon I\nu^2}{c^4 D}\left(\frac{1+\cos^2\iota}{2}\right)\cos(4\pi\nu t) \tag{1.2.3}$$

$$h_\times(t) = \frac{16\pi^2 G\epsilon I\nu^2}{c^4 D}\cos\iota\sin(4\pi\nu t). \tag{1.2.4}$$

For the work presented in Ch. 2, it is important to note that the GW amplitude for such systems is

$$h = \frac{16\pi^2 G\epsilon I\nu^2}{c^4 D}. \tag{1.2.5}$$

An isolated, rotating NS will continuously slow down due to GW emission. The amount of angular momentum radiated is

$$\frac{dJ}{dt} = -\frac{1024\pi^5}{5}\frac{G}{c^5}\epsilon^2 I^2 \nu^5. \tag{1.2.6}$$

Since $J = I\omega = 2\pi I\nu$, the rotational frequency evolution is

$$\dot{\nu} = -\frac{512\pi^4}{5}\frac{GI}{c^5}\epsilon^2\nu^5. \tag{1.2.7}$$

This assumes that the system only radiates angular momentum through GW emission.

1.2.2 CBC waveform

A compact binary coalescence can be modeled by two orbiting point particles (or black holes) having component masses m_1 and m_2. Again, the quadrupole tensor changes over time as the bodies orbit one another resulting in GW emission. The far-zone solution to the linearized Einstein field equations is

$$h_{ij}^{\mathrm{TT}}(t) = \frac{2G}{c^4 D}\ddot{I}_{ij}^{\mathrm{TT}}(t - D/c). \tag{1.2.8}$$

The second time derivative of the transverse-traceless quadrupole tensor for a CBC system is

$$\ddot{I}_{ij}^{\mathrm{TT}} = -2\mu v^2 \begin{bmatrix} \left(\frac{1+\cos^2\iota}{2}\right)\cos 2\phi & \cos\iota\sin 2\phi & 0 \\ \cos\iota\sin 2\phi & -\left(\frac{1+\cos^2\iota}{2}\right)\cos 2\phi & 0 \\ 0 & 0 & 0 \end{bmatrix},$$

where $\mu = m_1 m_2/M$, $M = m_1 + m_2$, $v = (\pi M G f_{\mathrm{gw}})^{1/3}$, f_{gw} is the GW frequency, and the orbital phase $\phi = \omega t = \pi f_{\mathrm{gw}} t = v^3 t/(GM)$. Therefore, the GW takes the form

$$h_{ij}^{\mathrm{TT}} = -\frac{4G\mu}{c^2 D}\left(\frac{v}{c}\right)^2 \begin{bmatrix} \left(\frac{1+\cos^2\iota}{2}\right)\cos(2\phi(v)) & \cos\iota\sin(2\phi(v)) & 0 \\ \cos\iota\sin(2\phi(v)) & -\left(\frac{1+\cos^2\iota}{2}\right)\cos(2\phi(v)) & 0 \\ 0 & 0 & 0 \end{bmatrix}, \tag{1.2.9}$$

and the functional form for the system's energy and luminosity can be used to solve for $\phi(v)$ and v in term of t.

Newtonian chirp waveform

In the Newtonian limit of GW, the energy and luminosity of a CBC system are

$$E(v) = -\frac{1}{2}c^2 M\eta\left(\frac{v}{c}\right)^2 \tag{1.2.10}$$

$$L(v) = \frac{32}{5}\frac{c^5}{G}\eta^2\left(\frac{v}{c}\right)^{10}, \tag{1.2.11}$$

where $\eta = \mu/M$. Since the luminosity is the amount of energy lost over time, $L = -dE/dt$. Therefore, using this relationship and the chain rule,

$$\frac{dt}{dv} = \frac{dt}{dE}\frac{dE}{dv} = -\frac{E'}{L}, \tag{1.2.12}$$

where the prime indicates a derivative with respect to v. Additionally, since $\phi = \omega t = v^3 t/(GM)$,

$$\frac{d\phi}{dv} = \frac{d\phi}{dt}\frac{dt}{dv} = -\frac{v^3}{GM}\frac{E'}{L}. \tag{1.2.13}$$

Integrating Eqs. (1.2.12) and (1.2.13) to some reference v, $v_{\rm ref}$, gives

$$t = t_{\rm ref} + \int_v^{v_{\rm ref}} \frac{E'(u)}{L(u)} du, \tag{1.2.14}$$

$$\phi = \phi_{\rm ref} + \int_v^{v_{\rm ref}} \frac{u^3}{GM}\frac{E'(u)}{L(u)} du. \tag{1.2.15}$$

The binary loses energy to gravitational waves as its components orbit. The result is that the orbit continually tightens and the orbital speed continually increases until the bodies eventually coalesce. Using Eqs. (1.2.10) and (1.2.11) in Eqs. (1.2.14) and (1.2.15) and solving for $t(v)$ and $\phi(v)$ where coalescence "c" is chosen for the reference "ref" gives

$$t(v) = t_{\rm c} - \frac{5}{256}\frac{GM}{\eta c^3}\left(\frac{v}{c}\right)^{-8}, \tag{1.2.16}$$

$$\phi(v) = \phi_{\rm c} - \frac{1}{32\eta}\left(\frac{v}{c}\right)^{-5}. \tag{1.2.17}$$

Inverting Eq. (1.2.16) to find $v(t)$, substituting this into Eq. (1.2.17) to find $\phi(t) = \phi(v(t))$, and putting $v(t)$ and $\phi(t)$ into Eq. (1.2.9) gives the GW perturbation as a function of time. The two polarizations are

$$h_+(t) = -\frac{G\mathcal{M}}{c^2 D}\left[\frac{c^3(t_{\rm c}-t)}{5G\mathcal{M}}\right]^{-1/4}\frac{1+\cos^2\iota}{2}\cos\left(2\phi_{\rm c} - 2\left[\frac{c^3(t_{\rm c}-t)}{5G\mathcal{M}}\right]^{5/8}\right) \tag{1.2.18}$$

$$h_\times(t) = -\frac{G\mathcal{M}}{c^2 D}\left[\frac{c^3(t_{\rm c}-t)}{5G\mathcal{M}}\right]^{-1/4}\cos\iota\,\sin\left(2\phi_{\rm c} - 2\left[\frac{c^3(t_{\rm c}-t)}{5G\mathcal{M}}\right]^{5/8}\right), \tag{1.2.19}$$

where $t < t_{\rm c}$. This is referred to as a "chirp" waveform because its frequency and amplitude both increase with time. If the wave properties were converted to sound, it would chirp. The Newtonian chirp only depends on mass through the parameter $\mathcal{M} = \eta^{3/5} M$, which is referred to as the chirp mass.

The GW strain seen in an interferometric detector from a CBC signal in the Newtonian limit is given by Eqs. (1.2.1), (1.2.18), and (1.2.19). It is convenient to express $h(t)$ in terms of the time and phase at which the signal terminates in the detector instead of the coalescence time and phase. To do this, realize that

$$h(t+t_0) = F_+(\alpha,\delta,\psi,t+t_0)h_+(t+t_c) + F_\times(\alpha,\delta,\psi,t+t_0)h_\times(t+t_c), \tag{1.2.20}$$

where t_0 is the termination time. For a Newtonian chirp, this can be compactly written in the following way:

$$h(t) = -\frac{G\mathcal{M}}{c^2 D_{\rm eff}}\left[\frac{c^3(t_0-t)}{5G\mathcal{M}}\right]^{-1/4}\cos\left(2\phi_0 - 2\left[\frac{c^3(t_0-t)}{5G\mathcal{M}}\right]^{5/8}\right), \tag{1.2.21}$$

where

$$2\phi_0 = 2\phi_c - \arctan\left(\frac{F_\times}{F_+}\frac{2\cos\iota}{1+\cos^2\iota}\right) \tag{1.2.22}$$

$$D_{\rm eff} = D\left[F_+^2\left(\frac{1+\cos^2\iota}{2}\right)^2 + F_\times^2\cos^2\iota\right]^{-1/2}, \tag{1.2.23}$$

$t < t_0$, and $F_{\times,+} = F_{\times,+}(\alpha,\delta,\psi,t)$. Here, ϕ_0 is the phase at termination. The effective distance $D_{\rm eff}$ is a distance parameter that takes into account the relative orientations of the binary and detector. If the binary and detector are optimally oriented, $D_{\rm eff} = D$, otherwise $D_{\rm eff} > D$.

The CBC waveform is often written in the frequency domain. The Fourier transform of the Newtonian chirp waveform under the stationary phase approximation is

$$\tilde{h}(f_{\rm gw}) = \sqrt{\frac{5\pi}{24}}\frac{G^2\mathcal{M}^2}{c^5 D_{\rm eff}}\left[\frac{\pi\mathcal{M}Gf_{\rm gw}}{c^3}\right]^{-7/6}\exp\left[-i\psi(f_{\rm gw})\right], \tag{1.2.24}$$

where

$$\psi(f_{\rm gw}) = 2\pi f_{\rm gw}t_c - 2\phi_c - \frac{\pi}{4} + \frac{3}{128}\left[\frac{\pi\mathcal{M}Gf_{\rm gw}}{c^3}\right]^{-5/3}. \tag{1.2.25}$$

The Fourier transform conventions used here and in the rest of this dissertation are

$$\tilde{x}(f) = \int_{-\infty}^{\infty} x(t)e^{-2\pi i f t}dt \tag{1.2.26}$$

$$x(t) = \int_{-\infty}^{\infty} \tilde{x}(f)e^{2\pi i f t}dt. \tag{1.2.27}$$

1.2.3 Post-Newtonian chirp waveform

Eqs. (1.2.24)–(1.2.25) and (1.2.21)–(1.2.23) model the inspiral portion of the CBC waveform in the time domain (TD) and the frequency domain (FD) at Newtonian order. However, the systems ground-based interferometers are most sensitive to will be relativistic and strongly gravitating. Post-Newtonian (PN) theory adds relativistic corrections to the Newtonian results presented in Sec. 1.2.2. The GR equations of motion are expanded in orders of the characteristic speed of the system. The CBC waveform becomes more accurate at high frequencies by adding more PN correction terms to the Newtonian waveform.

PN corrections to the CBC energy and luminosity functions have been calculated to 3.5PN order [10]:

$$\begin{aligned} E(x) &= -\frac{1}{2}c^2 M\eta x\left[1-\left(\frac{3}{4}+\frac{1}{12}\eta\right)x\right. \\ &\quad -\left(\frac{27}{8}-\frac{19}{8}\eta+\frac{1}{24}\eta^2\right)x^2 \\ &\quad \left.-\left(\frac{675}{64}-\left(\frac{34445}{576}-\frac{205}{96}\pi^2\right)\eta+\frac{155}{96}\eta^2+\frac{35}{5184}\eta^3\right)x^3\right] \qquad (1.2.28) \\ L(x) &= \frac{32}{5}\frac{c^5}{G}\eta^2 x^5\left[1-\left(\frac{1247}{336}+\frac{35}{12}\eta\right)x+4\pi x^{3/2}\right. \\ &\quad -\left(\frac{44711}{9072}-\frac{9271}{504}\eta-\frac{65}{18}\eta^2\right)x^2-\left(\frac{8191}{672}+\frac{583}{24}\eta\right)\pi x^{5/2} \\ &\quad +\left(\frac{6643739519}{69854400}+\frac{16}{3}\pi^2-\frac{1712}{105}\gamma-\frac{856}{105}\ln(16x)\right. \\ &\quad \left.+\left(\frac{41}{48}\pi^2-\frac{134543}{7776}\right)\eta-\frac{94403}{3024}\eta^2-\frac{775}{324}\eta^3\right)x^3 \\ &\quad \left.-\left(\frac{16285}{504}-\frac{214745}{1728}\eta-\frac{193385}{3024}\eta^2\right)\pi x^{7/2}\right]. \qquad (1.2.29) \end{aligned}$$

Here, the PN order corresponds to the highest power of the PN expansion parameter $x = (\pi M G f_{\rm gw}/c^3)^2$ in the square brackets (i.e. beyond leading Newtonian order) and $\gamma = 0.5772156649\ldots$ is the Euler constant.

The PN expansion of the energy and luminosity are used as inputs for finding the form of the PN CBC waveform, much like was done in Sec. 1.2.2. As will be shown in Sec. 4.A, this can be done in several ways.

PN waveforms are a good approximation to the inspiral portion of the complete CBC

waveform at low frequencies (early inspiral) and become less reliable near merger. They are commonly used to model BNS waveforms, which have very long inspiral portions and typically merge out-of-band, meaning at frequencies so high that shot noise dominates over signal (see Sec. 1.3). However, PN models are not effective at modeling BBH and IMBHB systems where merger happens in-band and therefore the merger and ringdown portion of the waveform become much more important. For these systems, effective-one-body waveforms calibrated to NR simulations are typically used instead [11].

1.2.4 Effective-one-body CBC waveform

Effective-one-body (EOB) waveforms are found by joining an inspiral waveform to a merger-ringdown waveform. The two-body CBC problem is first cast into an effective-one-body problem, much like what is done in classical mechanics. A PN resummed Hamiltonian is used to find the orbital evolution of the inspiral portion of the waveform [12]. The later stages of the inspiral right before merger can be adjusted to more closely match NR simulations by adding pseudo 4PN and pseudo 5PN coefficients and calibrating their values so that the waveform matches these simulations. EOB waveforms calibrated in this way are called EOBNR waveforms. A superposition of BH quasi-normal modes are used to construct the merger-ringdown waveform. The inspiral and merger-ringdown waveforms are then joined near the time at which the EOB orbital frequency is at a maximum [11].

EOBNR waveforms describe all three phases of a CBC signal and match high-accuracy NR simulations. However, they are relatively expensive to compute compared to the Taylor-expanded PN waveforms. Typically, Taylor-expanded PN waveforms are used to model BNSs and EOBNR waveforms are used to model BBH waveforms.

1.3 Dominant LIGO noise components

The entirety of this dissertation is geared toward searching for GWs in LIGO-VIRGO data and estimating source parameters or source population parameters given detection. To do this, GW signal models are compared to the data to check how well the models match the data, essentially comparing how much signal is in the noise. Therefore, it is important

to understand and incorporate the general characteristics of the detector noise, and we do this through the power spectral density (PSD) and the amplitude spectral density (ASD).

The one-sided power spectral density S of a detector is defined by

$$S(|f|)\frac{1}{2}\delta(f-f') = \langle \tilde{n}^*(f')\tilde{n}(f)\rangle, \tag{1.3.1}$$

where the $\langle \dots \rangle$ is an ensemble average over noise realizations. The ASD is the square root of the PSD. Fig. 2 plots sample ASDs from initial and enhanced LIGO and the design ASD for aLIGO.

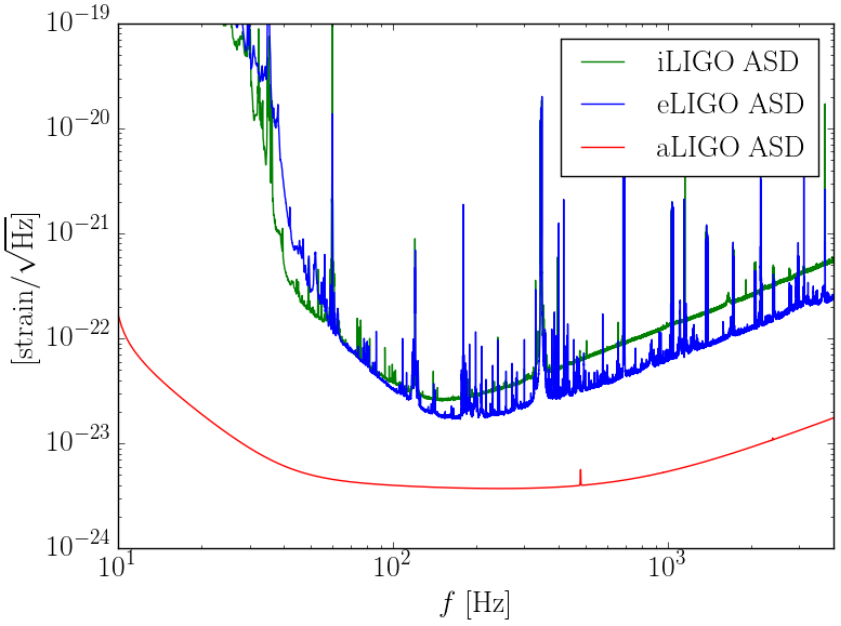

Figure 2 : The ASD for iLIGO and eLIGO, and the anticipated design ASD for aLIGO.

The distinct shape of the ASD is mainly the result of the following three dominant noise components, from which all ground-based interferometric detectors suffer.

1. **Seismic noise:** Seismic noise refers to Earth-based activity that vibrates an interferometer's end mirrors resulting in detector noise. Seismic vibrations typically manifest at low frequencies (up to tens of Hertz) and cause the steep low-frequency wall in the ASD. Examples of seismic activity known to affect the LIGO instruments include earthquakes, nearby traffic, airplanes, logging, and tumbleweed, but LIGO is mostly affected by microseismic activity. Great effort has been taken to isolate

the end mirrors in order to reduce seismic noise through an intricate pendulum system. Using a pendulum system introduces noise at the harmonic frequencies of the suspension wires. However, these noise spikes, which are clearly visible in the ASD, are extremely narrow and well-understood.

2. **Thermal noise:** The Brownian motion of particles in the suspension wires and in the end mirror coatings changes the effective arm length of the instrument. Since the amount of motion depends on temperature, this is called thermal noise. Thermal noise is dominant in the mid-frequency range from tens of Hertz to hundreds of Hertz. High-quality mirrors and suspension wires are used to minimize this noise source.

3. **Shot noise:** The interferometer measures changes in the light detected at a photodiode due to changes in the length of the interferometer arms. A photodiode essentially counts the number of photons hitting it over time, which is a Poisson process. Since it is a Poisson process, there is noise associated with this counting process, and this noise is called shot noise. Shot noise dominates at high frequencies (above roughly 100 Hz). A technique referred to as squeezing light can reduce the effects shot noise.

Chapter 2

Continuous Gravitational Waves from Isolated Galactic Neutron Stars in the Advanced Detector Era[1]

2.1 Background and motivation

Isolated neutron stars with non-axisymmetric deformations will continuously emit gravitational waves as they rotate [14]. Neutron stars also have strong dipolar magnetic fields that accelerate particles to relativistic energies [15]. Since these neutron stars can lose energy through the emission of electromagnetic and gravitational radiation, their rotational frequency slowly decreases over time. The gravitational wave strain amplitude of rotating neutron stars has a strong dependence on the star's rotational frequency. Though no gravitational wave detection has yet been reported, rapidly rotating isolated Galactic neutron stars are one of the most promising sources of continuous gravitational waves for ground based gravitational wave detectors.

Attempts to assess the detectability of gravitational waves from the Galactic neutron star population began with rough analytic estimates. An argument presented in Ref. [16] by Thorne but credited to Blandford models the Galactic neutron star population as a uniformly populated two-dimensional disk of gravitars (neutron stars with gravitationally

[1]This chapter was published in Ref. [13]

dominated frequency evolutions) all born at very high frequencies. Using this simplistic model, he estimated a rough upper bound on the possible gravitational wave strain amplitude from a Galactic neutron star, $h_{\max} \sim 10^{-25}$ [16]. Blandford also surprisingly observed that the maximum gravitational wave amplitude is independent of the size of the star's deformation and rotational frequency. His argument was revised in Ref. [17] and again in Ref. [18], which both found $h_{\max} \sim 10^{-24}$.

This work was followed by more comprehensive attempts to assess the detectability of the Galactic neutron star population through population synthesis. If the neutron star population can be accurately simulated, then the detectability of Galactic neutron stars can be determined. In Ref. [19] Palomba was the first to assess the detectability of a simulated gravitar population by first and second generation gravitational wave detectors. He incorporated realistic spatial, age, birth frequency, and kick velocity distributions, as well as a possible ellipticity distribution (though this is still largely unconstrained [19]). He estimated the fraction of the neutron star population that would likely have to be gravitars in order for first or second generation detectors to make a direct gravitational wave detection. Continued efforts by Knispel and Allen extended Blandford's argument to a simulated gravitar population similar to Palomba's [18]. They found that the maximum gravitational wave strain amplitude *does* have a strong dependence on the star's frequency and size of deformation when considering a more realistic neutron star population. They set upper bounds, which depend on the population's ellipticity (a measure of a star's deformation) and rotational frequency, on the gravitational wave strain amplitude of the nearest source.

In this chapter, we include electromagnetic emission as well as gravitational wave emission in the frequency evolution of neutron stars and investigate its effect on the population's detectability. We use the simulated neutron star population in Ref. [18] and assign every neutron star a dipolar magnetic field as well as an ellipticity. We then allow each star's frequency to evolve through the emission of both gravitational and electromagnetic radiation. The chapter is organized as follows. In Section 2.2 we review the spin and strain evolution of neutron stars and revisit the upper bounds from the gravitar case. In Section 2.3 we outline a Monte Carlo simulation used to assess

the detectability of the Galactic neutron star population. The results are then used to bound the magnetic field strength and ellipticity parameter space of isolated neutron stars with or without a direct gravitational wave detection. In Section 2.4 we present a rough analytic argument to which we compare our numerical results. In Section 2.5 we summarize our main results.

2.2 Spin and strain evolution of neutron stars

We use the simulated neutron star population from Ref. [18] to assess the detectability of gravitational waves emitted by isolated Galactic neutron stars. It is important to note that, while the simulated population does not explicitly include recycled millisecond pulsars, it does not necessarily exclude them either. Each star in our population is assigned a birth frequency, initial position, kick velocity, and age. Stars are then independently evolved through the Galaxy's gravitational potential (see Ref. [18] for a more detailed description of the population). Therefore an old star that has been recently recycled can just be thought of as a young star born with a high frequency. We also consider a large enough range in magnetic field strength to accommodate recycled pulsars. In this section, we review methods to find the spin frequency and gravitational wave strain amplitude of each star in our simulated population in order to assess its detectability.

If neutron stars only lose energy through gravitational and electromagnetic emission, their rotational frequency evolution is given by

$$\dot{\nu} = -\frac{512\pi^4}{5}\frac{GI}{c^5}\epsilon^2\nu^5 - \frac{8\pi^2}{3}\frac{R^6}{c^3 I}B^2\sin^2\alpha\,\nu^3, \tag{2.2.1}$$

in Gaussian units [18; 20; 21]. Here, G is the gravitational constant, c is the speed of light, ν is the star's rotational frequency, R is the star's radius, $I = kMR^2$ is the moment of inertia about its rotational axis with M being the star's mass and $k \approx 2/5$ [15], $\epsilon = (I_1 - I_2)/I$ is the ellipticity with I_1 and I_2 being the moments of inertia about the star's other two principle axes, B is the dipolar magnetic field strength at the magnetic equator, and α is the angle between its magnetic pole and its axis of rotation[2]. We choose

[2]The second term in Eq. (2.2.1), which is the frequency evolution due to electromagnetic emission, is derived from the simple model of a rotating dipole. In Ref. [22] Spitkovsky corrects this term such that a

the canonical values of $R = 10$ km and $M = 1.4M_\odot$ for all neutron stars [15]. Because we only concern ourselves with order of magnitude estimates, we set $\sin^2\alpha = 1$.

Eq. (2.2.1) can be solved analytically for $\nu(t, \nu_0)$ in the limits where $\epsilon = 0$ or $B = 0$. If $B = 0$, a neutron star will only emit gravitationally. Its frequency is

$$\nu(t, \nu_0) = \left({\nu_0}^{-4} - 4\gamma_{\rm gw} t\right)^{-1/4}, \tag{2.2.2}$$

where t is the neutron star's age, $\nu_0 = \nu(t = 0)$ is the neutron star's birth frequency, and $\gamma_{\rm gw} = -512\pi^4 G I c^{-5}\epsilon^2/5$. Eq. (2.2.2) is a good approximation for the frequency of a gravitar. The characteristic timescale (the approximate time for a neutron star with birth frequency $\nu_0 \gg \nu$ to spin down to a frequency ν) for gravitationally dominated emission is

$$\tau_{\rm gw} = -\frac{\nu}{4\dot{\nu}} \approx 290 \text{ Myrs} \left(\frac{10^{-7}}{\epsilon}\right)^2 \left(\frac{100 \text{ Hz}}{\nu}\right)^4. \tag{2.2.3}$$

If $\epsilon = 0$, a neutron star will only emit electromagnetically. Its frequency is

$$\nu(t, \nu_0) = \left({\nu_0}^{-2} - 2\gamma_{\rm dip} t\right)^{-1/2}, \tag{2.2.4}$$

where $\gamma_{\rm dip} = -8\pi^2 R^6 c^{-3} I^{-1} B^2 \sin^2\alpha/3$. Eq. (2.2.4) is a good approximation for the frequency of a neutron star whose evolution is dominated by electromagnetic emission and whose characteristic timescale is

$$\tau_{\rm dip} = -\frac{\nu}{2\dot{\nu}} \approx 1,600 \text{ yrs} \left(\frac{10^{12} \text{ G}}{B}\right)^2 \left(\frac{100 \text{ Hz}}{\nu}\right)^2. \tag{2.2.5}$$

While ϵ is unknown, the dramatically different timescales between Eqs. (2.2.3) and (2.2.5) illustrate the difficultly in detecting isolated neutron stars: stars with reasonable magnetic fields spin down to low frequencies too rapidly to detect. Therefore, gravitational wave detectors will likely only detect neutron stars with small magnetic fields or young neutron stars that have not yet spun down to low frequencies.

Not all neutron stars will have their frequency evolution dominated by either gravitational or electromagnetic emission. For these stars, $\dot{\nu}$ cannot be integrated over time to solve for an analytic solution for $\nu(t, \nu_0|\epsilon, B)$. However, Ref. [18] shows that Eq. (2.2.1) can instead be inverted to solve for $t(\nu, \nu_0|\epsilon, B)$. Following Ref. [18], we rewrite Eq. (2.2.1)

neutron star will still emit electromagnetically even if its magnetic pole and rotational axis are aligned.

as

$$\dot{\nu} = \gamma_{\rm gw}\nu^5 + \gamma_{\rm dip}\nu^3 \tag{2.2.6}$$

$$= \gamma_{\rm dip}\left(\gamma\nu^5 + \nu^3\right), \tag{2.2.7}$$

where $\gamma = \gamma_{\rm gw}/\gamma_{\rm dip}$. Eq. (2.2.7) can be solved for

$$t(\nu,\nu_0) = \frac{1}{2|\gamma_{\rm dip}|}\left[\frac{{\nu_0}^2-\nu^2}{{\nu_0}^2\nu^2} + \gamma\ln\left(\frac{\nu^2}{{\nu_0}^2}\left(\frac{1+{\nu_0}^2\gamma}{1+\nu^2\gamma}\right)\right)\right]. \tag{2.2.8}$$

If ν_0, t, $\gamma_{\rm gw}$, and $\gamma_{\rm dip}$ are known, Eq. (2.2.8) can be solved numerically to find ν using root finding techniques [23].

The strain amplitude of gravitational waves emitted by a neutron star at a radial distance r away from a detector is given by

$$h = 16\pi^2\frac{GI}{c^4}\frac{\epsilon\nu^2}{r} \tag{2.2.9}$$

$$\approx 4\times10^{-25}\left(\frac{\epsilon}{10^{-7}}\right)\left(\frac{\nu}{100\text{ Hz}}\right)^2\left(\frac{1\text{ kpc}}{r}\right), \tag{2.2.10}$$

assuming that the neutron star's sky location intersects a line normal to the plane of the detector arms and its axis of rotation is parallel to that line (optimal mutual orientation). Since we only concern ourselves with order of magnitude estimates, we assume optimal mutual orientation for all neutron stars [18], which overestimates the detectable amplitude by about a factor of four on average.

For a population of neutron stars whose radial distance from Earth r, age t, birth frequency ν_0, ellipticity ϵ, and magnetic field strength B are known, Eq. (2.2.2), (2.2.4), or (2.2.8) can be used to determine each star's spin frequency ν. Eq. (2.2.2) is used when $\gamma_{\rm gw}\nu^5 \gg \gamma_{\rm dip}\nu^3$, which we conservatively choose to be when $\gamma > 40$ s^2; Eq. (2.2.4) is used when $\gamma_{\rm gw}\nu^5 \ll \gamma_{\rm dip}\nu^3$, which we conservatively choose to be when $\gamma < 4\times10^{-9}$ s^2; Eq. (2.2.8) is used otherwise[3]. Eq. (2.2.9) can further be used to determine each star's gravitational wave strain amplitude h as measured in our detector. We compare each star's frequency and strain amplitude to a scaled gravitational wave detector's noise curve

[3]To determine the two γ cutoffs, we assume that one term will dominate over the other if it is at least three orders of magnitude greater than the other. Eq. (2.2.2) can be used when $\gamma \gg 1/\nu^2$. Therefore, we choose $\gamma > 10^3/\nu^2 = 40$ s^2 for $\nu = 5$ Hz. Eq. (2.2.4) can be used when $\gamma \ll 1/\nu^2$. Therefore, we choose $\gamma < 10^{-3}/\nu^2 = 4\times10^{-9}$ s^2 for $\nu = 500$ Hz.

in order to assess the detectability of the neutron star population. We explain how we derive the scaling factor in Section 2.3.

While Eq. (2.2.9) for the gravitational wave strain amplitude h does not depend explicitly on the magnetic field, B *does* help to determine ν through Eq. (2.2.1). There are two related effects. First, Figure 3 shows that, all other things being equal, neutron stars with large magnetic fields will spin down to low frequencies (high periods) much faster than neutron stars with small magnetic fields. Consequently, large magnetic fields will result in smaller and smaller gravitational wave amplitudes over time. Second, since gravitational wave detectors are sensitive to finite frequency ranges, neutron stars with large magnetic fields will rapidly spin through a detector's sensitive frequencies, which makes them less likely to be detected. Therefore, neutron stars with small magnetic fields are more likely to be detected than neutron stars with large magnetic fields. In this way, assuming we know the population's ellipticity, we can place lower bounds on the magnetic field of neutron stars in the absence of a gravitational wave detection.

We can gain intuition into the detectability of Galactic neutron stars by setting $B = 0$. This places an upper bound on h for fixed ϵ values. In Figure 4, we plotted the maximum gravitational wave strain amplitude $h_{\max}$ versus gravitational wave frequency $f = 2\nu$ of the simulated neutron star population presented in Ref. [18] with $B = 0$ and $\epsilon = 10^{-9}$, 10^{-8}, 10^{-7}, and 10^{-6}. A single point $(f, h_{\max})$ corresponds to the population's maximum gravitational wave amplitude $h_{\max}$ measured in the frequency band $[f, ef]$ where e is Euler's number.[4]

Our numerical result in Figure 4 is consistent with the result in Ref. [18], which was derived using a semi-analytical integration technique. Considering a distribution in frequency and a three-dimensional spatial distribution results in a clear dependence of $h_{\max}$ on both frequency and ellipticity [18]. The effect of the frequency distribution manifests itself in the overall shape of the four curves in Figure 4. Since stars with large ellipticities spin down much faster than stars with small ellipticities (Eq. (2.2.3)),

[4]To find $h_{\max}$, we considered 200 logarithmically spaced overlapping frequency bands and constructed histograms for the strain amplitude from the neutron stars in each band. We then solved for $h_{\max}$ using a linear fit in $\log_{10}$-space to the tail (largest h values) of each histogram. We used this method to minimize statistical fluctuations.

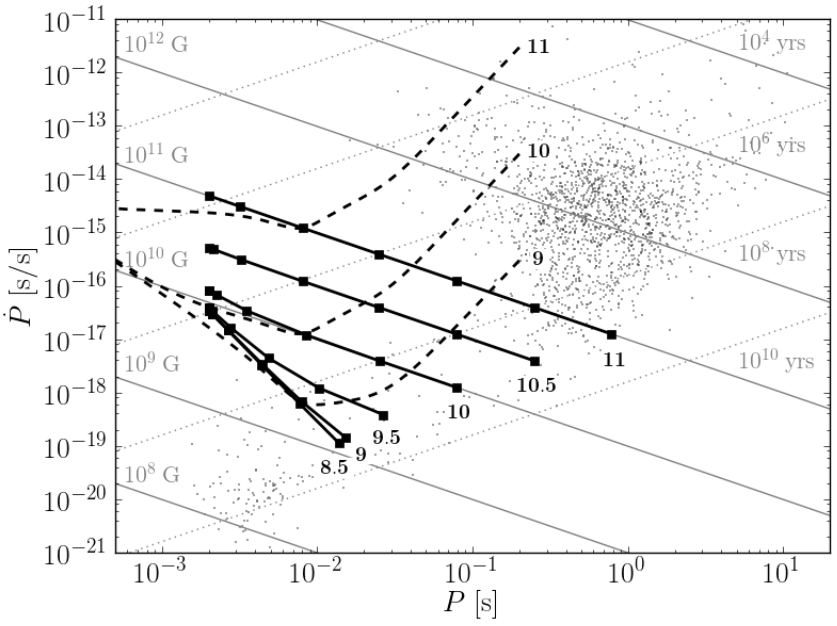

Figure 3 : This figure shows the period evolution of neutron stars. The dots represent observed pulsars from the ATNF catalog [24]. The thin, negatively sloped solid contours are lines of constant magnetic field strength (labels on the left), and the thin, positively sloped dotted contours are lines of constant characteristic age (labels on the right) assuming only electromagnetic emission. The thick, solid lines with square ticks track the period evolution of a neutron star that emits both electromagnetic and gravitational radiation. These lines, which are labelled by the logarithm of the star's magnetic field in units of Gauss, correspond to a neutron star with $\epsilon = 10^{-7}$ (all lines) and $B = 10^{8.5} - 10^{11}$ with steps of 1/2 dex. The square ticks represent logarithmic steps in age. The leftmost tick labels $t = 0$, and the subsequent ticks range from $t = 10^4 - 10^9$ yrs. The thick, dashed lines, which are labelled by the logarithm of the star's magnetic field in units of Gauss, are characteristic aLIGO sensitivity curves for neutron stars with $\epsilon = 10^{-7}$ located 100 pc away from Earth. Neutron stars below their associated aLIGO sensitivity curve are undetectable. Neutron stars with large magnetic fields spin down to low frequencies (high periods) much faster than stars with small magnetic fields; consequently, they spend less of their lives emitting gravitational waves with frequencies that aLIGO is most likely to detect.

a neutron star population with large ellipticities more densely populates low frequency bands than a neutron star population with small ellipticities. Therefore, while each curve in Figure 4 has a similar shape, the large ellipticity curves are shifted to the left relative to the small ellipticity curves. The subtle kink in the $\epsilon = 10^{-9}$ and 10^{-8} curves between the nearly flat, high frequency region and the more positively sloped, low frequency region corresponds to a kink in the population's frequency distribution, which is described in Ref. [18].[5] The $\epsilon = 10^{-7}$ and 10^{-6} curves also exhibit the same behavior but at

[5]Since we consider a continuous distribution in birth frequency, and a single star cannot be older than the Galaxy, neutron stars with high birth frequencies will not have existed long enough to have spun

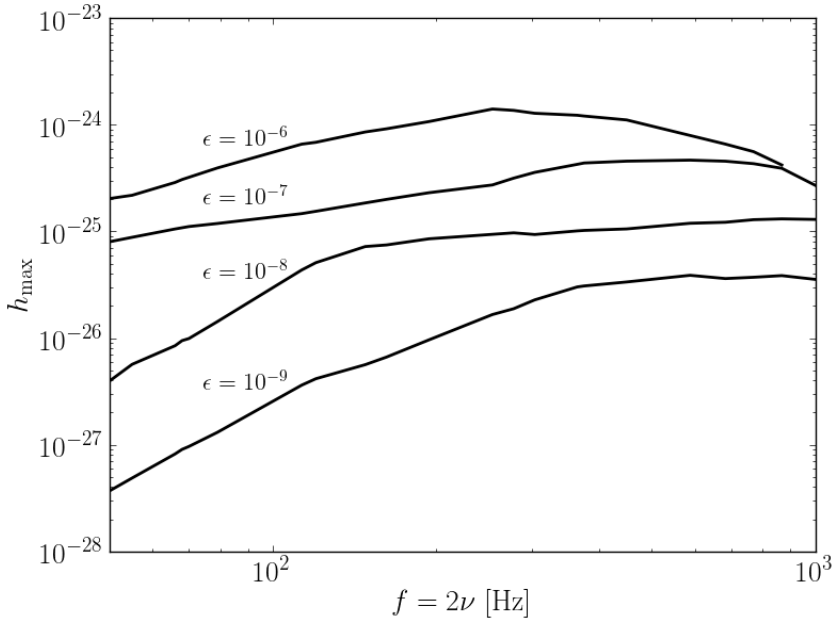

Figure 4 : We plot the maximum gravitational wave strain amplitudes $h_{\max}$ as a function of gravitational wave frequency $f = 2\nu$ of a population of gravitars (neutron stars with $B = 0$) with $\epsilon = 10^{-9}$, 10^{-8}, 10^{-7}, and 10^{-6}. A single point $(f, h_{\max})$ corresponds to the population's maximum gravitational wave amplitude $h_{\max}$ measured in the frequency band $[f, ef]$. We used the gamma initial radial distribution from Ref. [18] to simulate the neutron star population.

smaller frequencies than those plotted. If we had considered a two-dimensional spatial distribution, $h_{\max}$ would have been independent of the ellipticity in the region to the right of the kink. Here, the frequency distribution is in a nearly steady state. Considering a three-dimensional spatial distribution breaks this degeneracy between $h_{\max}$ and the population's ellipticity. Note that the gravitational wave strain amplitude will decrease when magnetic fields are considered.

2.3 Neutron-star detectability and constraints

To assess the detectability of the Galactic neutron star population, we use the methods outlined in Section 2.2 to find the spin frequency ν and gravitational wave strain amplitude h of every neutron star in our simulated population. The population used in our analysis is described in detail in Ref. [18]. Although [18] presents three different initial

down past a certain frequency. Neutron stars will accumulate near this frequency causing a kink in the population's frequency distribution, as seen in Ref. [18].

radial distributions, we choose to present our results using just the "gamma initial radial distribution". We expect minimal deviation in our results if we were to consider the other two distributions presented in Ref. [18]. The code that creates our simulated population provides the final position, which is easily turned into a distance from Earth r, and age t of each neutron star. Since a star's magnetic field strength B and ellipticity ϵ dictate its frequency evolution, we must also choose what values of each to assign to the stars in our population. We fix ϵ and B to a single value so that every neutron star in our population has the same ϵ–B combination. While this approach will not mimic a realistic neutron star population, it is an important first step that provides valuable intuition for considering a more realistic population in the future. Lastly, we assign each star a birth frequency $\nu_0 = 1/P_0$, where P_0 is randomly drawn from the lognormal birth period distribution in Ref. [18]:

$$\rho_{\mathrm{P}_0}(P_0) = \frac{1}{\sqrt{2\pi}\sigma P_0} \exp\left[-\frac{1}{2\sigma^2}\left(\ln P_0 - \ln \bar{P}_0\right)^2\right].$$

Here, $P_0 > 0.5$ ms is the birth period, $\bar{P}_0 = 5$ ms is the mean, and $\sigma = 0.69$ is the standard deviation. Given r, t, ν_0, ϵ, and B, we can use the methods outlined in Section 2.2 to find $\nu(t, \nu_0|\epsilon, B)$ and $h(r, \nu|\epsilon)$ for every neutron star in our simulated population.

Once ν and h are found for every neutron star, we can determine whether or not we expect a gravitational wave detector to detect our population. For simplicity, we only consider detection by a single Advanced Laser Interferometer Gravitational-wave Observatory (aLIGO) detector. We use the aLIGO noise curve for a single detector from Ref. [25], which is the expected sensitivity of aLIGO as a function of gravitational wave frequency. To estimate the strain, we assume that we have a year of aLIGO data, and that the data is analyzed coherently in short 72 hr stretches, with the short stretches combined incoherently. This assumes the LIGO Scientific Collaboration will be doing similar searches to the ones currently done by Einstein@Home [26] in the aLIGO era. An overall trials factor of 100 is applied, which is considered a conservative estimate. We then compare each neutron star to the estimated noise curve to determine the number of neutron stars in our population that aLIGO will be able to detect. We assume that a neutron star will be detected if its strain is above the aLIGO noise curve. To assess the

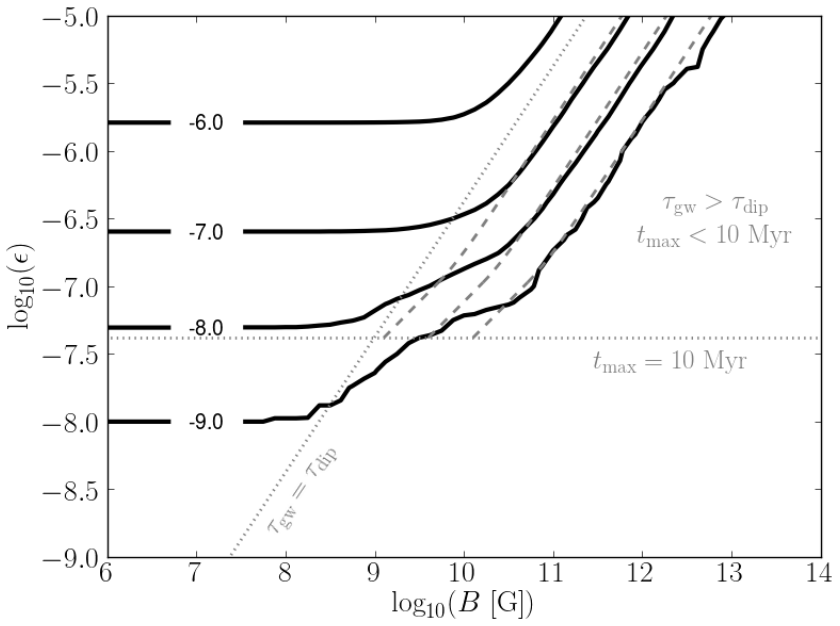

Figure 5 : Contours of $\log_{10} n$ (described in Section 2.3) with respect to $(\log_{10} B, \log_{10} \epsilon)$, which illustrate the expected detectability of the neutron star population with various ϵ and B combinations. Our analysis was performed on populations with logarithmic spacings of 1/8 dex in ϵ and B. The dashed lines are the analytic approximations for $\log_{10} n$ described in Section 2.4. We plot three results: $\log_{10} n = -7, -8, -9$, respectively from left to right. The dotted lines show the boundaries that separate where the analytic argument's assumptions are valid from where they are not (Section 2.4). They only hold for detectable neutron stars that are young ($t_{\rm max} \lesssim 10$ Myrs), found above the horizontal dotted line, and dominated by electromagnetic emission ($\tau_{\rm dip} \lesssim \tau_{\rm gw}$), found to the right of the positively sloped dotted line.

detectability of the neutron star population, we construct the fraction

$$n = \frac{N_{\rm det}}{N_{\rm sim}}, \tag{2.3.1}$$

where $N_{\rm sim}$ is the number of stars in the simulated population, and $N_{\rm det}$ is the number of stars aLIGO can detect from this population. To reduce statistical fluctuations, we simulate many more neutron stars than are actually expected to be in our Galaxy. Multiplying this fraction n by the number of neutron stars in our Galaxy $N_{\rm gal}$ gives the number of detectable neutron stars in our Galaxy. If $n \cdot N_{\rm gal}$ is greater than or equal to one, the population will likely be detectable; if it is less than one, the population will likely be undetectable. In Figure 5, we plot contours of $\log_{10} n$ with respect to $(\log_{10} B, \log_{10} \epsilon)$, illustrating the expected detectability of the neutron star population with various ϵ and B combinations.

We can further use our results (Figure 5) to place bounds on the ϵ–B parameter

space of the Galactic neutron star population. In Figure 5, the contour corresponding to $n \cdot N_{\rm gal} = 1$ is the boundary above which the ϵ–B parameter space is disallowed, assuming (pessimistically) no aLIGO detection of continuous gravitational waves associated with a Galactic neutron star. In this way, Figure 5 sets lower bounds on B for fixed ϵ values (or upper bounds on ϵ for fixed B values) if aLIGO does not make an isolated neutron star detection. For instance if $N_{\rm gal} \sim 10^9$ [19], and we assume neutron stars have a typical ellipticity of $\epsilon \sim 10^{-7}$ [19], Figure 5 shows that the minimum magnetic field strength of Galactic neutron stars is $B \gtrsim 10^{11}$ G in the absence of an aLIGO detection. Conversely if $N_{\rm gal} \sim 10^9$, and we assume neutron stars have a typical magnetic field strength of $B \sim 10^{11}$ G, Figure 5 shows that the population's maximum ellipticity is $\epsilon \lesssim 10^{-7}$ in the absence of an aLIGO detection. This argument also applies if aLIGO *does* make isolated neutron star detections. If $N_{\rm gal} \sim 10^9$, and we assume neutron stars have $\epsilon \sim 10^{-7}$, then the minimum magnetic field strength of Galactic neutron stars is $B \gtrsim 10^{10}$ G if aLIGO detects 10 neutron stars. Conversely if $N_{\rm gal} \sim 10^9$, and we assume neutron stars have $B \sim 10^{10}$ G, then the population's maximum ellipticity is $\epsilon \lesssim 10^{-7}$ if aLIGO detects 10 neutron stars.

2.4 Analytic results

In all previous sections, we used numerical methods to assess the detectability of Galactic neutron stars and place constraints on the properties of the Galactic neutron star population. In this section, we present an analytical approach to setting bounds on the ϵ–B parameter space of the Galactic neutron star population. Blandford's analytic argument considers neutron stars that emit only gravitationally. Our analytic argument, while still simplistic, applies to stars dominated by electromagnetic emission.

We first use the aLIGO sensitivity curve described in Section 2.3 to constrain the volume around Earth in which detectable neutron stars must be contained. If a neutron star is detected, it will tend to be at or near the detector's most sensitive frequency, which we call $\nu_{\rm det}$. For simplicity, we assume that a neutron star must have $\nu \approx \nu_{\rm det}$ to be detected. Therefore, a neutron star will be detected by a ground-based gravitational wave detector if $h(\nu_{\rm det}) > h_{\rm det}$, where $h_{\rm det}$ is the value of the strain amplitude for which

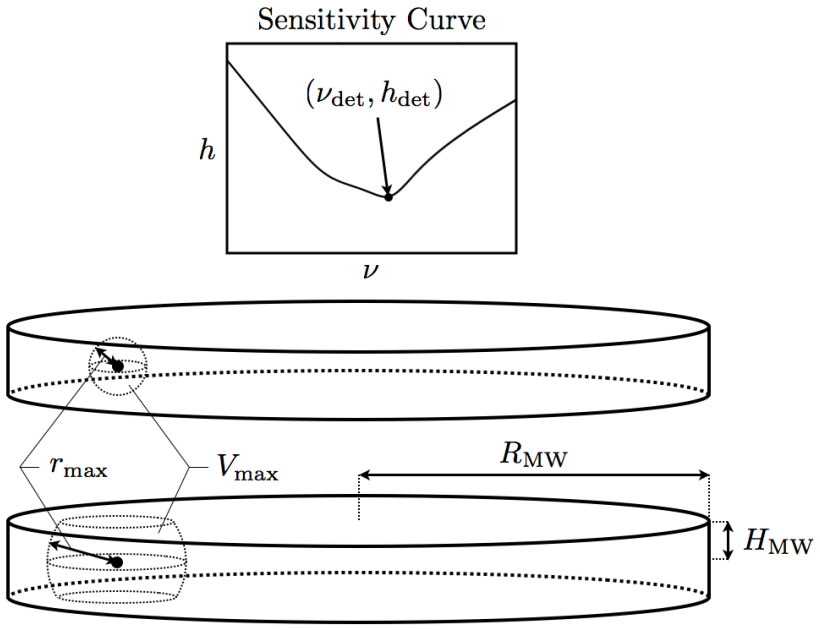

Figure 6 : The top plot is a typical sensitivity curve of a ground-based gravitational wave detector. We assume that isolated neutron stars with $h(\nu_{\rm det}) > h_{\rm det}$ will be detected. Below are diagrams of the Milky Way disk. The black dot is Earth's location within the Milky Way disk. The two volumes $V_{\rm max}$ outlined by dotted lines are the maximum volumes within which detectable neutron stars can be contained. $V_{\rm max}$ will be the volume of a sphere if $r_{\rm max} < H_{\rm MW}$ (top diagram), and $V_{\rm max}$ will be the volume of a spherical segment if $r_{\rm max} > H_{\rm MW}$ (bottom diagram). See Section 2.4.

the detector is most sensitive (see Figure 6). This detectability condition, along with Eq. (2.2.9), translates into a constraint on the distance from Earth of detectable neutron stars. The maximum distance $r_{\rm max}$ at which a neutron star with $\nu = \nu_{\rm det}$ could be detected is:

$$r_{\rm max} = 16\pi^2 \frac{GI}{c^4} \frac{\epsilon \nu_{\rm det}^2}{h_{\rm det}}. \tag{2.4.1}$$

The detectability condition also translates into a constraint on the volume that encloses detectable neutron stars. First, we assume that neutron stars are born uniformly throughout the Galactic stellar disk at a constant rate $\mathcal{N}$, which is the number of births per unit time. The volume of the Milky Way, which we approximate to be a disk, is roughly

$$V_{\rm MW} = \pi R_{\rm MW}^2 (2H_{\rm MW}), \tag{2.4.2}$$

where $R_{\rm MW}$ is the radius of the Galactic disk, and $H_{\rm MW}$ is half its height (Figure 6). The volume contained in $r_{\rm max}$ will be a sphere for $r_{\rm max} < H_{\rm MW}$. However, for $r_{\rm max} > H_{\rm MW}$, the

volume contained within $r_{\rm max}$ will be a sphere with its top and bottom caps truncated by the top and bottom surfaces of the Milky Way disk, as illustrated in Figure 6. This shape is called a spherical segment. Therefore, the maximum volume $V_{\rm max}$ in which neutron stars with $\nu = \nu_{\rm det}$ could be detected is:

$$V_{\rm max} = \begin{cases} \frac{4}{3}\pi r_{\rm max}^3 & r_{\rm max} < H_{\rm MW} \\ \frac{2}{3}\pi H_{\rm MW}\left(3r_{\rm max}^2 - H_{\rm MW}^2\right) & r_{\rm max} > H_{\rm MW} \end{cases} . \tag{2.4.3}$$

From the constraint on the volume that encloses detectable neutron stars of frequency $\nu = \nu_{\rm det}$, we can find the minimum allowed magnetic field strength in the absence of an isolated neutron star detection. Remembering our constant birth rate assumption, the average time $t_{\rm max}$ between neutron star births into the volume $V_{\rm max}$ is

$$t_{\rm max} = \mathcal{N}_{\rm max}^{-1} = \frac{V_{\rm MW}}{V_{\rm max}}\mathcal{N}^{-1}, \tag{2.4.4}$$

assuming a uniform spatial distribution. In order to ensure a neutron star detection, at least one star within the volume $V_{\rm max}$ must have $\nu > \nu_{\rm det}$ at all times. This will be the case if $\nu(t_{\rm max}) > \nu_{\rm det}$, because a neutron star spinning down below $\nu_{\rm det}$ will always be accompanied by a new star being born into the volume $V_{\rm max}$. Likewise, we also assume that, on average, when a detectable neutron star escapes $V_{\rm max}$ due to its motion in the Galaxy, another detectable neutron star will enter $V_{\rm max}$. Assuming that a neutron star's frequency evolution is dominated by dipolar emission, we solve for the minimum magnetic field strength $B_{\rm min}$ below which a neutron star detection is *not* guaranteed by substituting $t_{\rm max}$ into Eq. (2.2.4) and solving for B:

$$B_{\rm min}(\epsilon, h_{\rm det}, \nu_{\rm det}) = \begin{cases} B_{\rm min}^{\rm sphere} & r_{\rm max} < H_{\rm MW} \\ B_{\rm min}^{\rm sph.seg.} & r_{\rm max} > H_{\rm MW} \end{cases} , \tag{2.4.5}$$

where

$$\begin{aligned} B_{\rm min}^{\rm sphere} &= \frac{32\pi^2\nu_{\rm det}^2 I^2\epsilon^{3/2}}{\nu_0 R^3 h_{\rm det}^{3/2}}\sqrt{\frac{\pi G^3\mathcal{N}}{c^9 V_{\rm MW}}\left(\nu_0^2 - \nu_{\rm det}^2\right)} \\ B_{\rm min}^{\rm sph.seg.} &= \frac{cH_{\rm MW}}{2R^3\nu_0\nu_{\rm det}}\sqrt{\frac{cI\mathcal{N}H_{\rm MW}}{2\pi V_{\rm MW}}\left(\nu_0^2 - \nu_{\rm det}^2\right)}\left[\frac{768\pi^4 G^2 I^2\epsilon^2\nu_{\rm det}^4}{c^8 h_{\rm det}^2 H_{\rm MW}^2} - 1\right]^{1/2} . \end{aligned}$$

Neutron stars with $B > B_{\rm min}$ in $V_{\rm max}$ will spin down to $\nu < \nu_{\rm det}$ before another star is born into $V_{\rm max}$. Therefore, in the absence of an aLIGO detection, $B = B_{\rm min}$ is the

minimum possible magnetic field strength of Galactic neutron stars with fixed ellipticity values, since $B < B_{\rm min}$ ensures a detection.

Our argument is easily extended to the case of $N_{\rm s}$ neutron star detections. To do this, we solve for when $\nu(N_{\rm s} t_{\rm max}) > \nu_{\rm det}$. The result adds a factor of $N_{\rm s}^{-1/2}$ in front of Eq. (2.4.5).

We have made several assumptions in setting up our analytical argument. It is important to emphasize two of our argument's most crucial assumptions in order to clearly outline the physical systems for which our argument holds. The first crucial assumption is that the spatial distribution of neutron stars in the Milky Way is a uniform cylinder. Neutron stars will diffuse out of the Galactic disk due to Galactic acceleration and their kick velocities. The timescale for this process is found by dividing the average kick velocity in Ref. [18] by the gravitational acceleration (found by dividing the gravitational potential in Ref. [18] by the length scale). Therefore, our argument holds when $t_{\rm max} \lesssim 10$ Myrs. The second crucial assumption is that the frequency evolution of neutron stars is dominated by dipolar emission. Therefore, for $\nu_0 \gg \nu$, our argument holds when $\tau_{\rm dip} \lesssim \tau_{\rm gw}$.

In Figure 5, we have plotted the relationship in Eq. (2.4.5) (with the factor of $N_{\rm s}^{-1/2}$ in front) as dashed lines on top of our numerical results. We use $\nu_{\rm det} \approx 100$ Hz and $h_{\rm det} \approx 6.0 \times 10^{-26}$, which approximately corresponds to aLIGO's most sensitivity strain and associated frequency, and $R_{\rm MW} \approx 15$ kpc, $H_{\rm MW} \approx 75$ pc, and $\nu_0 \approx 850$ Hz, where $R_{\rm MW}$, $H_{\rm MW}$, and ν_0 are estimated averages of the spatial and period distributions in Ref. [18] found by reducing the maximum values by a factor of e^{-1}. We also use $\mathcal{N} \approx 0.02$ years^{-1} [27]. Our numerical results should roughly follow these dashed lines, which correspond to $n = 10^{-7}, 10^{-8}, 10^{-9}$, respectively from left to right. The analytic results only hold for detectable neutron stars that are young ($t_{\rm max} \lesssim 10$ Myrs), which corresponds to the region above the horizontal dotted line, and dominated by electromagnetic emission ($\tau_{\rm dip} \lesssim \tau_{\rm gw}$), which corresponds to the region to the right of the positively sloped dotted line. There is good agreement between our numerical and analytic results, except in the transition region near the dotted boundaries where the analytic assumptions start to lose their validity. While the rough numerical values chosen for the parameters in our analytic argument can change the overall normalization of the analytic curves, the shape of the

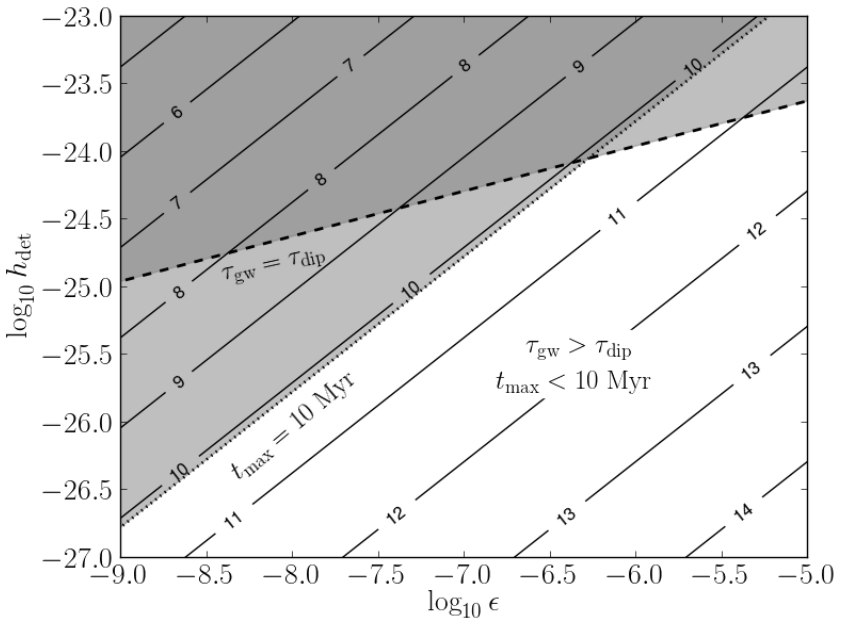

Figure 7 : Extends our analytic argument to any gravitational wave detector. Eq. (2.4.5) is plotted as solid contours of $\log_{10} B$ with respect to $(\log_{10} h_{\rm det}, \log_{10} \epsilon)$, where B is in units of Gauss. The dashed and dotted lines show the boundaries that separate where our analytic argument's assumptions are valid from where they are not. Our argument does not hold in the gray, shaded regions; our argument *does* hold for neutron stars that are young ($t_{\rm max} \lesssim 10$ Myrs), found below the dotted line ($t_{\rm max} = 10$ Myrs), and dominated by electromagnetic emission ($\tau_{\rm dip} \lesssim \tau_{\rm gw}$), found below the dashed line ($\tau_{\rm dip} = \tau_{\rm gw}$).

curves closely match the shape of the numerical contours.

While we only consider detection by aLIGO in our numerical analysis, our analytical approach easily extends to any gravitational wave detector. Notice that in Eq. (2.4.5) $B_{\rm min}$ is a function of ϵ, $h_{\rm det}$, and $\nu_{\rm det}$. Therefore, we fix $\nu_{\rm det}$ and plot contours of $\log_{10} B_{\rm min}$ with respect to $(\log_{10} \epsilon, \log_{10} h_{\rm det})$ in Figure 7 to illustrate how our argument extends to other detectors.

It also seems natural to extend our argument to the gravitar case, in which the frequency evolution of neutron stars is dominated by gravitational emission, by solving Eq. (2.2.2) for $B_{\rm min}$ under the assumption that $\tau_{\rm gw} \lesssim \tau_{\rm dip}$. However, detectable gravitars can be older than 10 Myrs, thus violating our assumption that $t_{\rm max} \lesssim 10$ Myrs. Therefore, these methods cannot be applied to the gravitar case.

2.5 Conclusion

We have used the methods described in Section 2.2 to find the gravitational wave amplitude and spin frequency of every neutron star in the simulated population described in Ref. [18]. This involved allowing for both electromagnetic and gravitational emission in a neutron star's frequency evolution (Eq. (2.2.1)). We then solved for each neutron star's frequency using either Eq. (2.2.2), (2.2.4), or (2.2.8) and each neutron star's gravitational wave strain amplitude using Eq. (2.2.9). We used the simulated population to assess the detectability of and set bounds on the ϵ–B parameter space of the Galactic neutron star population. Our results are summarized in Figure 5. Assuming that the Galactic neutron star population consists of $N_{\text{gal}} \sim 10^9$ stars, and assuming aLIGO does not make a neutron star detection, the contour $\log_{10} n = -9$ in Figure 5 separates the allowed ϵ–B parameter space (below the contour) from the disallowed ϵ–B parameter space (above the contour). In other words, assuming we know the magnetic field strength of the neutron star population, we can place upper bounds on the population's ellipticity; or, assuming we know the ellipticity of the neutron star population, we can place lower bounds on the population's magnetic field strength.

In this chapter, we have only considered the simple (and unrealistic) case in which all neutron stars have the same magnetic field strength and ellipticity. However, we have demonstrated that both a gravitational wave detection or the lack of a gravitational wave detection can be used to constrain some of the properties of the Galactic neutron star population. To make confident quantitative statements regarding the properties of the Galactic neutron star population, we must construct a more realistic population. Moving forward, we plan to incorporate magnetic field and ellipticity distributions and evolutions into our analysis to more closely mimic the Galactic neutron star population [19; 28; 29].

Chapter 3

Developing a compact binary coalescence search for intermediate-mass black-hole binaries

3.1 Motivating a CBC search for intermediate-mass black-hole binaries

In this section, we discuss (*i*) what an intermediate-mass black hole (IMBH) is, current observational evidence for their existence, and how one might form, (*ii*) how IMBHs might end up in a binary system that coalesces in less than a Hubble time and current rate estimates for their coalescence within aLIGO's reach, and (*iii*) why we are developing a CBC search for these systems when we have only used burst searches in the past.

3.1.1 Intermediate-mass black holes

Roughly speaking, we define an IMBH to be a BH with a mass above the upper edge of the stellar-mass BH mass range, which is a few tens of solar masses, and below the lower edge of the supermassive BH mass range, which is roughly a hundred thousand solar masses.

There is now strong evidence of supermassive BHs in the center of galaxies. Their existence can be inferred through observations of quasars, which are luminous active galactic nuclei whose electromagnetic emission is likely produced by accretion onto supermassive BHs. Additionally, the motion of stars around the center of our Galaxy is consistent with orbital motion about a supermassive BH with a mass of $\sim 10^6$ $M_\odot$ [30].

Stellar-mass BHs, which are thought to be the remnants of the gravitational collapse of massive stars, also have strong observational support. Bright X-ray sources in our Galaxy are thought to be the product of stellar-mass BHs accreting matter from a companion star. The mass of the X-ray-emitting compact objects can be estimated through radial velocity measurements of their companions. The compact objects can be conclusively determined to be BHs if their masses are > 3 $M_\odot$, which is too massive to be a NS, and many such sources have been observed [31].

While there is strong evidence for the existence of stellar-mass BHs and supermassive BHs, observational evidence for the existence of IMBHs is still inconclusive. Ultra-luminous X-ray sources such as discussed in Ref. [32] might be driven by accretion onto IMBHs. However, accretion onto stellar-mass BHs cannot be ruled out because beaming models powered by accretion onto a stellar-mass BH with a jet can also produce ultra-luminous X-rays [33; 34]. More recently there is increasing evidence that there exists an IMBH in the galaxy M82. By extrapolating the stellar-mass-BH scaling of quasi-periodic oscillations in the X-ray emission with BH mass to IMBHs, Ref. [35] finds the mass of the ultra-luminous X-ray source in M82 to be ~ 400 $M_\odot$. However, not enough is currently known about IMBHs to ensure that this extrapolation is valid. Perhaps the most compelling suggestion for IMBHs is the existence of stellar-mass BHs and supermassive BHs. It seems natural that merging stellar-mass BHs could result in an IMBH, and likewise merging IMBHs could result in supermassive BHs.

If IMBHs exist, they likely form in one or more of the following ways.

1. **Formation through stellar collapse:** Hypothetical Population III stars are early-universe stars with negligible metallicity. These stars could have been massive enough to leave behind IMBHs after their death. However, it has been suggested

that stars with masses roughly between 140 $M_\odot$ and 260 $M_\odot$ will violently explode in a pair-instability supernova. In this process, the star's core becomes hot enough to produce electron-positron pairs. This results in energy and pressure loss, which leads to a partial collapse followed by accelerated oxygen burning. The star then explodes leaving behind no remnant. However, for stars in excess of roughly 260 $M_\odot$, pair-instability will not occur, and the likely outcome of a core collapse is an IMBH. Population III stars are not the only candidates for stellar collapse into IMBHs. Recently, several stars with masses greater than 150 $M_\odot$ and initial masses as high as $\sim$300 $M_\odot$ have been observed in the R136 region of the Large Magellanic Cloud [36]. This discovery demonstrates that there are conditions in which very massive stars can be sustained. High-metallicity stars can have stellar winds capable of removing half or more of their mass. So, if some of these types of stars have low metallicity and mild stellar winds, they could collapse into IMBHs [37].

2. **Formation in globular clusters:** A globular cluster is a collection of tightly-bound stars orbiting a galactic core. Because globular clusters are old, the most massive stars will have had enough time to collapse leaving behind dense and massive stellar remnants, such as NSs and BHs. These objects will tend to sink to the center of the cluster and interact with one another. The close proximity of these massive objects in globular clusters could result in enough encounters to grow a BH through mergers with or accretion from stars or stellar remnants [2].

3. **Formation in young stellar clusters:** Young stellar clusters might also cultivate IMBHs. The most massive stars in a young cluster will still be on the main sequence and will also sink toward the center in a cluster core collapse. The close proximity of stars with such large cross sections (relative to stellar remnants) will lead to many collisions. The most massive stars will collide first, growing in size and becoming even more susceptible to future collisions. Enough collisions will result in a very massive star that can form an IMBH through gravitational collapse, as described in the first formation mechanism [2].

3.1.2 IMBH binaries[1]

Assuming the existence of IMBHs as described in Sec. 3.1.1, we will now discuss possible mechanism for their formation in binaries. Here, we consider mechanisms resulting in binary coalescence times less than a Hubble time, which allows them to be aLIGO sources.

1. **Common envelope phase:** Two orbiting IMBHs produced by very massive stars with separations greater than tens of solar radii will not merge in a Hubble time. Assuming no interactions with other stars, a common envelope phase is required to instigate mergers over a shorter timescale. When one of the stars leaves the main sequence, its envelope can expand and fully engulf the binary system. As the companion is dragged through the envelope, the binary will tighten and the envelope can become unbound. The result is a tightened binary including an IMBH. This process can even occur twice, which results in an even tighter binary with two IMBHs.

2. **Binary single interactions:** The coalescence of two orbiting IMBHs produced by very massive stars with separations greater than tens of solar radii in less than a Hubble time can also be accomplished dynamically. One such mechanism is through single interactions. Essentially, nearby passing stars or other compact objects can increase the binary's eccentricity causing the coalescence time to decrease. Through many single interactions, a wide binary can be brought to merge within a Hubble time.

3. **Triple systems:** Similarly, a triple system involving an IMBHB and a tertiary object can dynamically shrink the coalescence time of the binary. Through the Kozai mechanism, the tertiary's inclination will oscillate with the binary's eccentricity through many orbits. These Kozai cycles can cause a wide binary to merge on a much shorter timescale.

Ref. [37] estimated the IMBHB merger rate for aLIGO with these mechanisms in mind. Using population synthesis, it was shown that IMBHB mergers supported by a

[1]This subsection closely follows explanations in Ref. [37]

common envelope phase can have rates as few as zero per year and as many as 300–600 per year in aLIGO once design sensitivity is achieved. The optimistic rate of 300–600 events per year ignores the possibility of pair-instability supernovae for Population I stars, while the pessimistic rate of zero events per year assumes that stars do not survive the common envelope phase. It is considered most realistic to assume that stars can survive the common envelope phase but allow for pair-instability supernovae. This results in a rate of 3–6 events per year. It was also shown via order-of-magnitude estimates that non-expanding, wide binaries coalescing due to single interactions and/or the Kozai mechanism result in a rate of roughly 100 IMBHB mergers per year.

3.1.3 Why develop a CBC search for IMBHBs?

Little is known about IMBHs, and GW observations can provide the first definitive proof of their existence. IMBHB detections could support the current supermassive BH formation models which designate IMBHs as seeds for these giants, shed light on globular cluster dynamics, test GR in the strong-field regime, and constrain the pair-instability supernova mechanism. IMBHBs also enable aLIGO to probe cosmological redshifts up to $z \sim 2$.

Burst searches have been run on LIGO data in the past [38; 39]. A burst search is an un-modeled search for bursts of energy in the data that are not statistically consistent with noise. Since IMBHB signals merge near the low-frequency edge of the LIGO sensitive band, only the last few orbits of a massive IMBHB signal stands out above the noise and therefore closely resembles a short burst of gravitational energy. Fig. 8 shows the S6 ASD as well as the characteristic amplitude $h_c = \sqrt{f} \cdot |\tilde{h}(f)|$ of a $m_1 = m_2 = 150$ $M_\odot$ IMBHB at a distance $D \sim 800$ Mpc.

Advanced detectors will have vastly improved low-frequency sensitivity over their predecessors. Fig. 8 also shows a Recolored ASD, which represents aLIGO's anticipated ASD through the first few years of operation before reaching design sensitivity. Even still, the waveform spends much more of its evolution in aLIGO's sensitive band. Therefore, a matched filter search using CBC waveforms as filters can be effectively implemented to search for IMBHBs in aLIGO data.

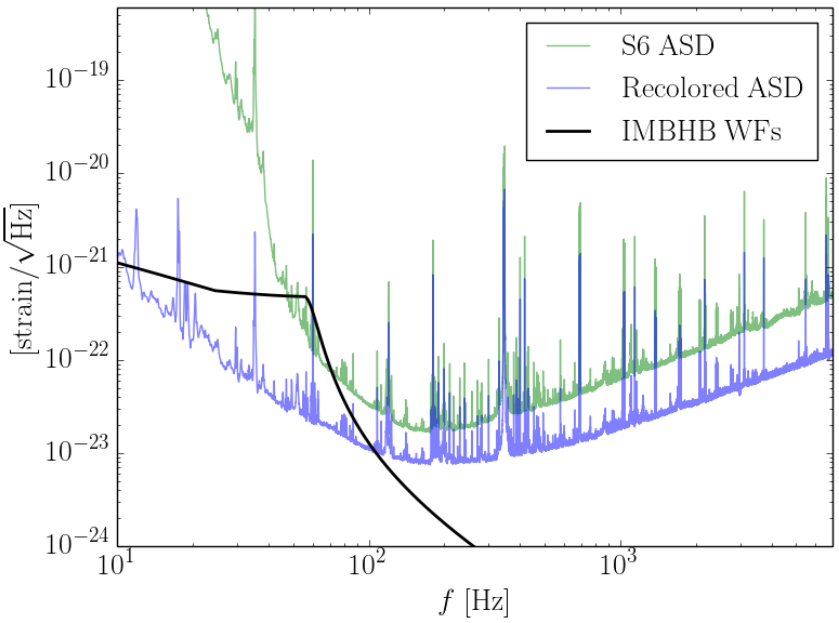

Figure 8 : ASDs for data from S6 and S6 data recolored to an anticipated early aLIGO ASD. Also plotted is the characteristic amplitude $h_c = \sqrt{f} \cdot |\tilde{h}(f)|$ for an IMBHB with 150 $M_\odot$ component masses at a distance of $D \sim 800$ Mpc.

3.2 CBC search strategy using gstlal

IMBHBs are CBC systems and can therefore be modeled by the waveforms described in Sec. 1.2.2. Since we have a model for these events, we can perform a matched filter search for IMBHB signals, and we use the offline `gstlal_inspiral` software to perform this search. We outline the search procedure in this section. We start with a general overview of the search, which describes how the search works in layman's terms, and subsequently explain each phase in more detail.

3.2.1 General overview

There are several techniques for searching for GW signals in noisy instrument data. Knowledge of what the signal looks like (i.e. knowing the shape of the signal) allows us to employ the optimal way to find hidden signals. We use theoretical CBC waveform models to find real GW signals from CBC events hidden in noisy instrument data by trying to match patterns in the data with the shape of the model, or template.

As outlined in Sec. 1.2.2, the CBC waveform is referred to as a chirp because

its frequency and amplitude increase together during its long inspiral phase before it merges and quickly rings down. Since all CBC chirp waveforms follow this same general time/frequency evolution, we have an idea of what GWs from CBC events will look like in our data. However, our model depends on many source parameters of the system, which include things like the binary's component masses and sky location. The values of the system's source parameters influence certain aspects of the waveform, such as its phase and/or amplitude evolution. For instance, keeping all other parameters the same, a CBC chirp waveform with component masses $m_1 = m_2 = 50\ \mathrm{M}_\odot$ is a much different looking signal than one with $m_1 = m_2 = 150\ \mathrm{M}_\odot$, as illustrated in Fig. 11. While they both have roughly the same properties in that they share common chirp waveform features, the lower mass binary evolves much slower and merges at a much higher frequency than the higher mass binary. In fact, these waveforms are the same under a rescaling of the time variable $t \to 3t$. So, although all chirp waveforms share some similarities, the shape of the signal depends significantly on source parameters that are *a priori* unknown. This means that we have many different signal shapes to search for in our data in order to cover our entire search parameter space.

The way in which we search for signals with varying source parameters is by constructing a bank of waveform templates that each have different source parameters, and thus each have a slightly different shape. The bank is a representation of the entire search parameter space sampled in such a way that a real GW will be close enough in shape to the nearest template that it will still be found by searching the data for each template in our bank.

The most basic CBC models, which assume that the components are non-spinning, have nine source parameters to search over. Of these nine source parameters, seven are extrinsic parameters, meaning that they are observer dependent, and only two are intrinsic, meaning that they are source dependent. All but two of the extrinsic parameters affect only the amplitude of the signal and do not have to be searched over at all (at least for the dominant component of the signal), and clever tricks can be used to maximize over the other two extrinsic parameters. A more detailed explanation of these points is discussed below. Therefore, the template bank need only be laid out over intrinsic

parameters. For the non-spinning case, the intrinsic parameters are m_1 and m_2.

The way one might imagine searching for signals with known shapes hidden in noisy data is to *filter* the data through each waveform template and compare the shape of your templates to the shape of the data. If the data only contains noise, there would be no overall pattern in the data that matches the shape of any of your templates. However, if a CBC signal is present in the data, the pattern it makes in the data will *match* at least one of your templates. Instead of doing this comparison by eye, which would only be successful for unrealistically large signals, we use a statistic called a *matched filter* to determine how closely the data matches our waveform templates. Roughly speaking, the matched filter is a measure of the correlation of the data with the signal model. It is typical to set a threshold on the matched filter or some matched-filter-like quantity. Anything above this threshold is called a "trigger" and might be a real GW signal. The matched filter is the optimal detection statistic if the statistical properties of the instrument's noise do not change over time (i.e. the instrument noise is stationary) and the noise is normally distributed (i.e. the instrument noise is Gaussian).

However, the noise in the LIGO and Virgo detectors is neither stationary nor Gaussian. It is not stationary because environmental factors, such as rush hour traffic, can cause the instrument's noise properties to change over time. The noise is roughly stationary, though, over time scales of a GW signal, and the statistical properties of the noise can be recomputed over time scales larger than that of a GW signal but smaller than that of the time-evolution of the noise. The noise is not entirely Gaussian either because it contains transient spikes, which we call "glitches". Because glitches can be large relative to signals (they are sometimes visible by eye, whereas a real signal most likely will not be), even though glitches do not match the shape of a template, they can still result in large values for the matched filter, since the statistic is derived assuming Gaussian noise. Therefore, the matched filter statistic alone is not enough to claim a GW detection.

Glitches are assumed to be uncorrelated across detectors, meaning that a glitch in H1 will be independent of what is happening in L1. However, if a GW hits H1, then L1 will also contain a GW signal at some nearby time. Therefore, a powerful veto for ruling out triggers produced by glitches is to check for triggers in at least one other detector

that occur at roughly the same time. If a trigger in a single detector does not have a counterpart at a nearby time in another detector, it is assumed to have been caused by a glitch and is not considered a GW candidate. Not only does a trigger in one detector have to have a counterpart in another detector that occurs at roughly the same time, it must also have been found with the same template. For instance, it might happen that a trigger-producing glitch occurs in H1 at the same time that a trigger-producing glitch occurs in L1. Since the glitches are uncorrelated, they may have very different shapes and result in large matched filter values for very different looking templates in each detector. These triggers are assumed to be caused by glitches since they were found with different templates. Therefore, triggers must be *coincident in time and template* in order to be considered a GW candidate.

Unfortunately, trigger-producing glitches happen often enough in our detectors that they even pass our coincidence vetoes, and we therefore need an additional detection statistic designed to suppress their significance. The detection statistic that is effective at down-weighting glitches is the χ^2 statistic. Just as the matched filter statistic can be roughly thought of as a correlation of the data with the signal model, the χ^2 statistic can be roughly thought of as a measure of how consistent the residual of the data and the signal model is with noise. Real signals will have small values for the χ^2 statistic while glitches result in much larger values for the χ^2 statistic.

Equipped with two detection statistics and two coincidence vetoes, triggers are ranked by the likelihood ratio, which is a function of our two detection statistics. The numerator of the likelihood ratio is the probability that a coincident trigger is a real GW signal and is a distribution that can be analytically derived; the denominator is the probability that the trigger was produced by noise and is constructed using the rejected noise triggers, i.e. those found in one instrument with no counterpart in the other. The likelihood ratio is used to rank all our GW candidates. It is also used to calculate a coincident trigger's false-alarm probability and false-alarm rate. The false-alarm rate is the typical quantity used to demonstrate our confidence that a given GW candidate is a detection.

This was a very general overview of our CBC search strategy. In the following subsections, we provide more detail into how each step is accomplished.

3.2.2 Traditional method to calculate signal-to-noise ratio[2]

If a GW from a CBC event, such as an IMBHB, hits a GW detector, such as LIGO or Virgo, then the data $d(t)$ will consist of both a true GW signal $h_{\rm GW}(t;\vec{\theta}_{\rm GW})$ with source parameters $\vec{\theta}_{\rm GW}$ and instrument noise $n(t)$:

$$d(t) = h_{\rm GW}(t;\vec{\theta}_{\rm GW}) + n(t). \tag{3.2.1}$$

However, if no GWs hit the detector, then the data will consist only of noise: $d(t) = n(t)$. Assuming that the noise $n(t)$ is stationary and Gaussian, then the optimal detection statistic is called the matched filter and is defined as

$$x(\vec{\theta}) = (d(t), h_{\rm GW}(t;\vec{\theta}_{\rm GW})), \tag{3.2.2}$$

where we have also defined a noise-weighted inner product of two time series $a(t)$ and $b(t)$ as follows:

$$(a(t), b(t)) = 4{\rm Re}\int_0^\infty \frac{\tilde{a}(f)\tilde{b}^*(f)}{S_n(f)}df. \tag{3.2.3}$$

Here, tildes represent Fourier transforms, and S_n is the one-sided PSD of detector n. Notice that the matched filter assumes that we know the exact gravitational waveform with its exact source parameters. If only nature were so kind... Instead, we have theoretical models for the CBC waveform, which we call templates, and these models depend on many intrinsic and extrinsic parameters. In order to perform a matched filter search for GWs hidden in our data, we must find a way to search over each of these parameters.

Searching over extrinsic parameters: Be clever

Eq. (1.2.21) in Sec. 1.2.2 for the CBC waveform in the time domain can be written very generally as:

$$h_{\rm T}(t;\vec{\theta}) = \left(\frac{\mathcal{A}(t-t_0;\vec{\theta}_{\rm in})}{D_{\rm eff}(\vec{\theta}_{\rm ex},t)}\right)\cos\left[2\phi_0 + 2\phi(t-t_0;\vec{\theta}_{\rm in})\right], \tag{3.2.4}$$

where the T subscript labels h as a waveform template. Here, we have separated the waveform parameters $\vec{\theta}$ into intrinsic parameters $\vec{\theta}_{\rm in}$ and extrinsic parameters $\vec{\theta}_{\rm ex}$. Additionally, we have separated the arrival time t_0 and phase ϕ_0, which are arbitrary constants

[2]The entirety of this subsection closely follows Refs. [40] and [9].

in the CBC waveform, from the rest of the extrinsic parameters. We have also grouped the arrival time t_0 with the dependent time parameter t, since they always appear in combination. Therefore, the waveform parameters are $\vec{\theta} = \{\vec{\theta}_{\rm in}, \vec{\theta}_{\rm ex}, \phi_0\}$.

Since the extrinsic parameters $\vec{\theta}_{\rm ex}$ only enter into the amplitude of the waveform, they merely set a scale factor for the matched filter search. This assumes that the extrinsic parameters do not change over the signal duration, which is true for short-duration non-spinning and aligned-spin systems. We can therefore just normalize the matched filter, which makes it unnecessary to search over the extrinsic parameters $\vec{\theta}_{\rm ex}$. By convention, we also choose to set $D_{\rm eff} = 1$ Mpc.

The arrival time, however, is an important parameter to search over since it determines where in the data the signal is located. One could imagine sliding a waveform template along the data and calculating the matched filter at every point in time. This is equivalent to doing the following:

$$x(t_0; \vec{\theta}_{\rm in}) = (d(t), h_{\rm T}(t - t_0; \vec{\theta}_{\rm in})) \tag{3.2.5}$$

$$= 4{\rm Re} \int_0^\infty \frac{\tilde{d}(f)\tilde{h}^*_{\rm T}(f; \vec{\theta}_{\rm in})}{S_n(f)} \exp(2\pi i f t_0) df, \tag{3.2.6}$$

where $x(t_0; \vec{\theta}_{\rm in})$ is the matched filter time series for the waveform template $h_{\rm T}$ with intrinsic parameters $\vec{\theta}_{\rm in}$, since we do not need to search over the extrinsic parameters $\vec{\theta}_{\rm ex}$. The second line follows from the first because the Fourier transform of $h_{\rm T}(t - t_0; \vec{\theta}_{\rm in})$ is $\tilde{h}_{\rm T}(f; \vec{\theta}_{\rm in}) \exp(-2\pi i f t_0)$. Ignoring the unknown phase ϕ_0 which will be addressed shortly, if the waveform template is close in form to the true GW signal, then the largest matched filter value will correspond to the matched filter maximized over arrival time.

The phase ϕ_0 is also an unknown parameter that must be searched over. This is done by constructing a linear combination of matched filter outputs where each corresponds to the waveform evaluated at orthogonal phases. Then, the matched filter maximized over phase is just the quadrature sum of the two matched filter outputs. An efficient way of constructing these orthogonal-in-phase matched filter outputs is by computing the complex matched filter time series

$$z(t_0; \vec{\theta}_{\rm in}) = x(t_0; \vec{\theta}_{\rm in}) + iy(t_0; \vec{\theta}_{\rm in}) = 4 \int_0^\infty \frac{\tilde{d}(f)\tilde{h}^*_{\rm T}(f; \vec{\theta}_{\rm in})}{S_n(f)} \exp(2\pi i f t_0) df. \tag{3.2.7}$$

The function $x(t_0;\vec{\theta}_{\rm in})$ is the matched filter time series of the template in Eq. (3.2.4) evaluated at $2\phi_0$, and $y(t_0;\vec{\theta}_{\rm in})$ is the matched filter time series for the template evaluated at $2\phi_0 \to 2\phi_0 - \pi/2$, since for $f > 0$: $\tilde{h}_{\rm T}(f;\vec{\theta}_{\rm in})|_{2\phi_0-\pi/2} = \tilde{h}_{\rm T}(f;\vec{\theta}_{\rm in})|_{2\phi_0} e^{i\pi/2} = i\tilde{h}_{\rm T}(f;\vec{\theta}_{\rm in})|_{2\phi_0}$. The matched filter maximized over phase is just

$$|z(t_0;\vec{\theta}_{\rm in})| = \sqrt{x^2(t_0;\vec{\theta}_{\rm in}) + y^2(t_0;\vec{\theta}_{\rm in})}. \tag{3.2.8}$$

Finally, as mentioned above, we choose to normalize the matched filter output to eliminate any amplitude dependence in the template waveforms. We call the normalized amplitude of the complex matched filter time series the *signal-to-noise ratio* (SNR) time series:

$$\mathrm{SNR}(t_0;\vec{\theta}_{\rm in}) = \frac{|z(t_0;\vec{\theta}_{\rm in})|}{\sigma(\vec{\theta}_{\rm in})}, \tag{3.2.9}$$

where the normalization constant is

$$\sigma(\vec{\theta}_{\rm in}) = \sqrt{(h_{\rm T}(t-t_0;\vec{\theta}_{\rm in}), h_{\rm T}(t-t_0;\vec{\theta}_{\rm in}))}. \tag{3.2.10}$$

The value of $\sigma(\vec{\theta}_{\rm in})$ is a measure of a detector's sensitivity and does not depend on t_0 since the two time series are the same and thus share the same arrival time. The SNR maximized over time and phase for a given template, which we call the SNR for simplicity, is the largest value of the SNR time series.

This is how we search over extrinsic parameters. Next, we address searching over intrinsic parameters.

Searching over intrinsic parameters: Construct a template bank

The final parameters to search over are the intrinsic parameters $\vec{\theta}_{\rm in}$. To do so, we generate a bank of waveform templates with specific intrinsic parameters discretely sampled over the entire parameter space of a given search. The intrinsic parameter space must be sampled finely enough that the true waveform is close enough to the nearest template to produce a large enough SNR for detection. This is done by choosing a minimal match (MM) and placing templates in such a way that any possible GW signal is guaranteed to have a mismatch less than $100(1-\mathrm{MM})\%$ with at least one template in the bank [41]. If a template bank does not meet this minimal match criterion for all possible waveforms

within the desired intrinsic parameter space of a given search, the template bank is said to have "holes".

To search over the intrinsic waveform parameters, an SNR time series is calculated for each template in the bank. It is convenient to absorb the constant $\sigma(\vec{\theta}_{\rm in})$ into the template bank by normalizing the templates as follows: $h_{\rm T,n} = h_{\rm T}/\sigma = h_{\rm T}/\sqrt{(h_{\rm T}, h_{\rm T})}$. The SNR time series is then

$$\mathrm{SNR}(t_0; \vec{\theta}_{\rm in}) = |z(t_0; \vec{\theta}_{\rm in})|, \tag{3.2.11}$$

where the complex matched filter time series is written in terms of normalized templates:

$$z(t_0; \vec{\theta}_{\rm in}) = 4 \int_0^\infty \frac{\tilde{d}(f)\tilde{h}^*_{\rm T,n}(f; \vec{\theta}_{\rm in})}{S_n(f)} \exp(2\pi i f t_0) df. \tag{3.2.12}$$

Any time the SNR time series of Eq. (3.2.11) surpasses a pre-determined SNR threshold for a given template, local peak-finding is applied over time to find the largest value of the SNR time series, and the corresponding SNR, arrival time, and template parameters are stored as a single-detector trigger (augmented with $\chi^2_{\rm auto}$ as described in Sec. 3.2.4).

3.2.3 SNR calculation in gstlal

The previous subsection described the traditional method for calculating SNR, which involves Fourier transforms to maximize over time. Since `gstlal_inspiral` was developed as a low-latency trigger generator, it calculates the SNR time series in the TD to avoid the unavoidable latency accumulated by performing this operation in the FD. The normalized matched filter time series is computed in the time-domain as follows:

$$\mathrm{x}(t_0; \vec{\theta}_{\rm in}) = 4 \int_{-t_{\rm dur}}^0 d_{\rm w}(t + t_0) h_{\rm T,w,n}(t; \vec{\theta}_{\rm in}) dt, \tag{3.2.13}$$

where $d_{\rm w}(t)$ is the *whitened* data stream, which is the inverse Fourier transform of $\tilde{d}(f)/\sqrt{S_n(f)}$, and $h_{\rm T,w,n}(t; \vec{\theta}_{\rm in}) = h_{\rm T,w}(t; \vec{\theta}_{\rm in})/\sqrt{(h_{\rm T,w}, h_{\rm T,w})}$ is the normalized whitened waveform template, where $h_{\rm T,w}(t; \vec{\theta}_{\rm in})$ is the inverse Fourier transform of $\tilde{h}_{\rm T}(f; \vec{\theta}_{\rm in})/\sqrt{S_n(f)}$ [42]. Since the template has some finite duration $t_{\rm dur}$, the integral is just performed over the duration of the template. To maximize over phase, the matched filter time series $\mathrm{y}(t_0; \vec{\theta}_{\rm in})$ for the orthogonal-in-phase template evaluated at

$2\phi_0 \to 2\phi_0 - \pi/2$ must also be calculated. Then the quadrature sum of the two matched filter outputs is the SNR time series maximized over phase. Local peak finding is then used to maximize over time.

Despite the slightly different strategy, calculating the SNR (maximized over time and phase) in the TD is equivalent to calculating this quantity in the FD. However, TD filtering is less computationally efficient than using a fast Fourier transform for FD filtering. To make TD filtering more computationally competitive, `gstlal_inspiral` time-slices and down-samples its templates and then performs a singular-value decomposition (SVD) on the template bank to drastically reduce the number of templates required for filtering. Since these operations are not essential to understanding the development of the CBC search for IMBHBs, we will not delve into more detail. Instead, we refer the interested reader to Ref. [42].

3.2.4 Autocorrelation χ^2

Sec. 3.2.2 introduced the SNR as the optimal detection statistic for stationary, Gaussian noise. However, the noise in the LIGO and Virgo instruments is neither stationary nor Gaussian. Environmental factors, such as rush hour traffic, cause the instrument's noise properties to change over time. The noise *is* roughly stationary, though, over typical time scales of a GW signal. The noise PSD can therefore be frequently recomputed over time scales larger than that of a GW signal but smaller than that of the time-evolution of the noise. However, transient noise excitations called "glitches" are non-Gaussian noise features that can cause the SNR detection statistic to fail. For this reason, the χ^2 statistic, which is effective at assigning glitches low significance, is a detection statistic calculated in addition to the SNR. There are many different types of χ^2 statistics, and `gstlal_inspiral` typically uses the autocorrelation χ^2 statistic, or *autochisq* for short.

The autochisq statistic is found by integrating the square of the difference between the SNR time series centered around a GW trigger and the scaled autocorrelation function (ACF) of the associated template. A template's ACF is essentially calculated by finding the SNR time series of the template filtered over itself:

$$\mathrm{ACF}(t_0;\vec{\theta}_{\mathrm{in}}) = \left| 4\int_0^\infty \tilde{h}_{\mathrm{T,w,n}}(f;\vec{\theta}_{\mathrm{in}})\tilde{h}^*_{\mathrm{T,w,n}}(f;\vec{\theta}_{\mathrm{in}})\exp(2\pi i f t_0)df \right| . \tag{3.2.14}$$

Since the templates are normalized, the maximum value of the ACF, which happens at $t_0 = 0$, is 1. In order to compare the ACF to the SNR time series, it must be scaled to the same amplitude, and the maximum value of the SNR time series must be shifted to $t_0 = 0$. The autochisq statistic can then be written in the following way:

$$\chi^2_{\text{auto}} = \int_{-T/2}^{T/2} \left| \text{SNR}(t_0; \vec{\theta}_{\text{in}}) - \text{SNR}_0 \cdot \text{ACF}(t_0; \vec{\theta}_{\text{in}}) \right|^2 dt_0, \tag{3.2.15}$$

where $\text{SNR}_0 = \text{SNR}(0; \vec{\theta}_{\text{in}})$ is the maximum value of the SNR time series and T is a tunable amount of time over which to calculate χ^2_{auto}. In practice, it is the autocorrelation length (ACL) that is the tunable parameter which specifies the number of samples to include in the integral, and $T = \text{ACL} \cdot \Delta t$ where $\Delta t = 1/(\text{sample rate})$. The value of χ^2_{auto} will be small for signals that are triggered by closely-matching templates, which should happen for real GW signals, and large for signals triggered by templates with dissimilar properties, which should happen for glitches [43].

Fig. 9 demonstrates how the SNR maximized over phase and time and the autochisq statistics can be used to distinguish noise events from real signals. Plotted by red and black crosses are all the coincident triggers recorded in a `gstlal_inspiral` search run over two months of simulated data. The red crosses labeled "Injections" are candidates that are associated with simulated GW signals manually injected into the data. The black crosses labeled "background" are candidates that are not associated with injected signals and are surely noise events since the search used simulated data. If the χ^2_{auto} axis were projected onto the SNR axis, which would be the case if SNR were the only detection statistic used, then the injections would not be distinguishable from the background events. The inclusion of the autochisq statistic, however, results in a clear separation between injection and background events. Another thing to notice is that the value of χ^2_{auto} increases with SNR. This is apparent in Eq. (3.2.15) since the difference between each point in the SNR and ACF time series will increase with the maximum SNR.

3.2.5 Ranking GW candidates[3]

The ultimate goal of a GW search is to find GW candidate signals and make statistically significant claims regarding how likely they are to be real GW detections. The statistic

[3]The entirety of this subsection closely follows Ref. [44].

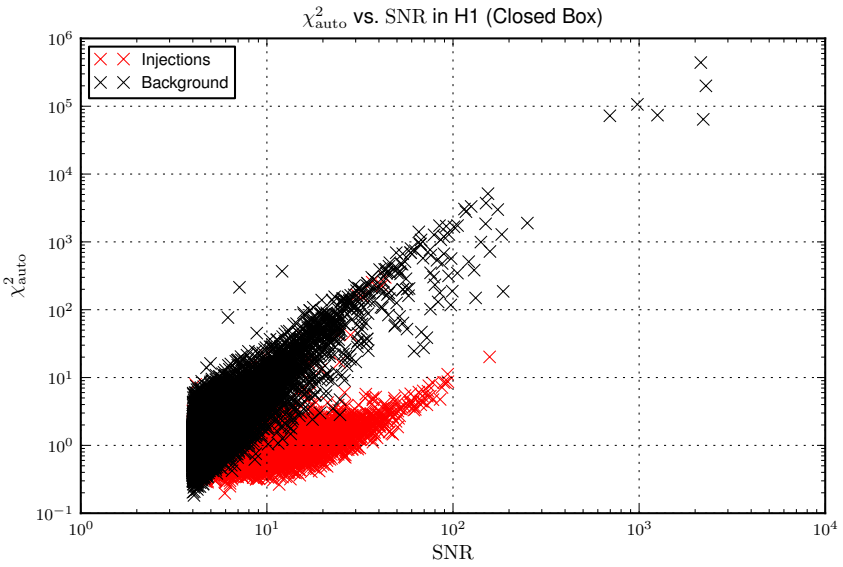

Figure 9 : $\chi^2_{\rm auto}$ vs. SNR in H1. Values associated with injections are marked in red and values associated with noise events, which are often referred to as "background" events, are marked in black.

that is often associated with the significance of a GW signal from a CBC search is the false-alarm rate (FAR), which is a measure of how often noise will result in a signal with identical properties. In this section we outline how to go from trigger generation all the way through FAR calculations.

Coincidence

In Sec. 3.2.2, we present SNR as the optimal detection statistic in stationary Gaussian noise. While the LIGO–Virgo detector noise is neither stationary nor Gaussian, the SNR statistic is still useful for finding and ranking GW candidates. In a `gstlal_inspiral` search, as the data is filtered through each template in the bank, whenever the SNR time series exceeds a pre-determined SNR threshold, which we choose to be $\mathrm{SNR}_\tau = 4$, local peak-finding is applied over time to find the largest value of the SNR time series. The corresponding SNR, arrival time, and template parameters are grouped together as a single-detector trigger. As each trigger gets generated, the autochisq statistic also gets calculated and grouped with the rest of the trigger information.

When single-detector triggers are coincidence in time and template across at least two detectors, they are stored as GW detection candidates. Coincident in time means that

triggers are found in different detectors within some time window of each other. This time window accounts for the small but finite amount of time it takes for a GW traveling at the speed of light to hit one instrument and then another. Coincident in template means that the single-detector triggers are also found with the same template across detectors. When single-detector triggers are not coincidence in time and template across at least two detectors, they are assumed to be noise events.

From here on out, when we use the word "coincidence" in reference to triggers, it is implied that we mean "coincident in time and template", unless otherwise stated.

Likelihood ratio

The SNR and autochisq statistics are used to rank GW candidates through the likelihood ratio

$$\Lambda = \frac{P(\mathrm{SNR}_1, \chi^2_{\mathrm{auto},1}, \ldots, \mathrm{SNR}_n, \chi^2_{\mathrm{auto},n}, \vec{\theta}_{\mathrm{in}}|\mathrm{s})}{P(\mathrm{SNR}_1, \chi^2_{\mathrm{auto},1}, \ldots, \mathrm{SNR}_n, \chi^2_{\mathrm{auto},n}, \vec{\theta}_{\mathrm{in}}|\mathrm{n})}, \tag{3.2.16}$$

which is the probability of observing a certain combination of detections statistics given that the candidate is a true signal "s" over the same probability give that the candidate is the result of noise "n". It is assumed that the likelihood ratio can be separated into the product of likelihood ratios from individual detectors:

$$\Lambda = \prod_n^{\mathrm{det}} \Lambda_n = \prod_n^{\mathrm{det}} \frac{P(\mathrm{SNR}_n, \chi^2_{\mathrm{auto},n}, \vec{\theta}_{\mathrm{in}}|\mathrm{s})}{P(\mathrm{SNR}_n, \chi^2_{\mathrm{auto},n}, \vec{\theta}_{\mathrm{in}}|\mathrm{n})}. \tag{3.2.17}$$

The numerator of Λ_n is evaluated assuming that signals are found during periods of time where the data is relatively stationary and Gaussian. Therefore, the probability of observing certain SNR values can be determined by assuming signal sources are uniformly distributed in space and the probability of observing certain χ^2_{auto} is demonstrated in Ref. [45]. This numerator therefore is neither detector dependent nor template dependent. The denominator of Λ_n is constructed by filling a histogram with the SNR and autochisq values from the non-coincident single-detector triggers. Fig. 10 plots examples of the raw histograms for the numerator and denominator of the likelihood ratio in Gaussian noise and recolored enhanced LIGO data for a 1-day analysis.

Once constructed, the likelihood ratio Λ is used to rank all candidate signals against each other. The higher the likelihood ratio, the more likely a candidate signal is a real

GW and not just a noise product. In order to assign a meaningful significance to a GW candidate, we calculate its false-alarm probability and false-alarm rate from its likelihood ratio.

False-alarm probability and false-alarm rate

The false alarm probability (FAP) for a candidate with likelihood ratio Λ_0 is the probability the a noise event has a likelihood ratio greater than or equal to Λ_0. Basically, the FAP is the probability that a noise event is at least as likely as the candidate. The FAP is found from the probability of observing a certain likelihood ratio Λ' given that the candidate is a noise event, or $P(\Lambda'|\mathrm{n})$. This can be found by first integrating the denominator of the likelihood ratio over surfaces of constant likelihood ratio

$$P(\Lambda', \vec{\theta}_{\mathrm{in}}|\mathrm{n}) = \int_{\Sigma(\Lambda')} P(\mathrm{SNR}_1, \chi^2_{\mathrm{auto},1}, \ldots, \mathrm{SNR}_n, \chi^2_{\mathrm{auto},n}, \vec{\theta}_{\mathrm{in}}|\mathrm{n}) d^{n-1}\Sigma \tag{3.2.18}$$

to find the probability of observing a certain likelihood ratio Λ' with a template defined by the intrinsic parameters $\vec{\theta}_{\mathrm{in}}$ (see Ref. [44] for details on how this is done), and then marginalizing over the template bank:

$$P(\Lambda'|\mathrm{n}) = \int P(\Lambda', \vec{\theta}_{\mathrm{in}}|\mathrm{n}) d\vec{\theta}_{\mathrm{in}}. \tag{3.2.19}$$

Integrating from Λ to infinity

$$P(\Lambda' \geq \Lambda|\mathrm{n}) = \int_{\Lambda}^{\infty} P(\Lambda'|\mathrm{n}) d\Lambda' \tag{3.2.20}$$

gives the probability that a noise event would be assigned a likelihood ratio at least as large as Λ. This is the FAP if a GW search produced just a single coincident trigger. However a GW search will produce many GW candidates. The probability of observing one or more events with a likelihood ratio at least as large as Λ when the search produced m candidates is

$$\mathrm{FAP}(\Lambda) = P(\Lambda' \geq \Lambda|\mathrm{n}_1, \ldots, \mathrm{n}_m) = 1 - (1 - P(\Lambda' \geq \Lambda|\mathrm{n}))^m. \tag{3.2.21}$$

Notice that the FAP never used any signal information. The FAP is thus independent of whether or not the search detects any real signals.

The FAP can be used to calculate the FAR of a candidate signal. It is assumed that the probability of observing one or more noise events with a likelihood of at least Λ is a Poisson distribution, which takes the form

$$\mathrm{FAP}(\Lambda) = 1 - e^{-\lambda}, \tag{3.2.22}$$

where λ is the mean number of events. Therefore, if the T is the observational time, the FAR is

$$\mathrm{FAR}(\Lambda) = \frac{\lambda(\Lambda)}{T} = -\frac{\ln[1 - \mathrm{FAP}(\Lambda)]}{T}. \tag{3.2.23}$$

By combining Eqs. (3.2.23), (3.2.21), and (3.2.20), the FAR can be equivalently expressed as

$$\mathrm{FAR}(\Lambda) = -\frac{m \ln[\int_0^{\Lambda} P(\Lambda'|\mathrm{n}) d\Lambda]}{T}. \tag{3.2.24}$$

In this way, every GW candidate produced during the filtering process gets ranked by the likelihood ratio of Eq. (3.2.17), and assigned a FAP from Eq. (3.2.21) and a FAR from Eq. (3.2.24).

3.3 Developing a CBC search for IMBHBs

The `gstlal_inspiral` software was originally developed to search for BNSs in low-latency. It has since been expanded to a broader parameter space that includes NSBHs and stellar-mass BBHs [46]. My collaborators and I are working to extend the search parameter space even more to include massive binaries involving IMBHs. This section outlines what has been learned in extending `gstlal_inspiral` to search over the IMBHB parameter space and presents results from a recent mock data challenge (MDC).

3.3.1 MDC1

MDCs are a primary tool in the LSC for testing the sensitivity of a GW search. It is typically the first testing ground for tuning and optimizing a GW search in preparation for searching for real signals in real GW data. In an MDC, synthetically produced data (or sometimes archival data) is injected with simulated GW signals (called "injections") to test a given search's sensitivity for finding these injections and ranking them as real

signals. The data is typically constructed to mimic real GW data, and the injection set is designed to mimic the types of astrophysical signals being searched for, though they are usually injected at a much higher rate than anticipated. For a CBC search, the MDC tests how well a template bank recovers the injection set and is a testing ground for adjusting any tunable parameters to improve the search sensitivity.

We have finished the first IMBHB MDC and are working through a second. Each MDC is designed to test different aspects of the IMBHB search. Since this is the first CBC search for sources up to a total mass of ~ 300 $M_\odot$, MDC1 was designed to merely be an end-to-end test of how effective a CBC search could be at detecting such high mass signals. We therefore kept the MDC1 configuration to be as simple and idealized as possible.

MDC1 configuration

In Fig. 13, we show the amplitude spectral density (ASD), which is just the square root of the PSD, of the MDC1 data set. It was generated by whitening enhanced LIGO data from the sixth science run and recoloring it to the anticipated ASD for the early years of Advanced LIGO. Whitening is the process of removing the overall frequency dependence of a data set by dividing by its ASD. Recoloring is the process of adding an overall frequency dependence to the data. The result is glitchy data, much like we expect Advanced LIGO-data to be, that has the same noise floor as is expected in early Advanced LIGO. We used roughly two months of recolored data from the three detectors H1, L1, and V1.

For simplicity, we focussed our MDC1 efforts on three distinct source classes: asymmetric mass ratio binaries uniformly and narrowly distributed about $m_1 = 50$ $M_\odot$ and $m_2 = 5$ $M_\odot$, equal mass binaries with moderate component masses uniformly and narrowly distributed about $m_1 = m_2 = 50$ $M_\odot$, and equal mass binaries with large component masses uniformly and narrowly distributed about $m_1 = m_2 = 150$ $M_\odot$ (see Fig. 12). For simplicity, we refer to each class of signals as the "5:50" , "50:50", "150:150" injection set and have plotted one of each in Fig. 11 for reference. The injections were distributed uniformly in a sphere whose radius corresponds to the distance to an optimally-oriented

signal with single-detector characteristic SNR = 14 (defined in Sec. 4.3.3). For reference, this distance is 240 Mpc for 5:50 injections, 1,140 Mpc for 50:50 injections, and 1,160 Mpc for 150:150 injections. The simulated signals were injected every 100 seconds to densely populate the data with non-overlapping signals. Signal orientations were also drawn from uniform distributions. The waveform approximant used to simulate these sources is EOBNRv2, which is like a pN inspiral waveform with a merger and ringdown calibrated to NR simulations and is part of the LIGO Algorithm Library [47]. This waveform family does not allow for spinning components. Injections were either generated starting at a lower frequency $f_{\rm low}$ of 25 Hz or 10 Hz, which is explained more in the next section.

We searched for these injection sets using an EOBNRv2 template bank. The templates were placed over the intrinsic parameters m_1 and m_2 to cover the overlapping surface of $3\ {\rm M}_\odot \leq m_2 \leq m_1 \leq 200\ {\rm M}_\odot$, $50\ {\rm M}_\odot \leq m_1 + m_2 \leq 350\ {\rm M}_\odot$, and $1/14 \leq m_2/m_1 \leq 1$ with a minimal match of roughly 0.985. Templates were either generated starting at a lower frequency $f_{\rm low}$ of 25 Hz, resulting in 645 templates, or 20 Hz, resulting in 779 templates, and the reasoning for this is explained more in the next section. Fig. 12 shows the template bank placement in mass space for templates generated at $f_{\rm low} = 20$ Hz.

Search sensitivity

To determine how sensitive a search is to an injection population, we treat the injections as we would any real signal in our data. We filter the data (with injections) through our template bank and collect a list of GW candidates. Each is ranked with a likelihood, which eventually gets translated into a FAR. To analyze how sensitive the search is to our injection sets, we use a threshold in FAR to separate all of our candidates associated with injections into "missed" or "found" categories. Fig. 15 shows missed/found plots in decisive $D_{\rm eff}$ versus $M_{\rm total}$ for each injection set. For injections marked as "found", the decisive $D_{\rm eff}$ is the second largest effective distance calculated for the coincident detectors; for injections marked as "found", the decisive $D_{\rm eff}$ is the second largest effective distance calculated for the participating detectors. The FAR threshold used to separate "missed" from "found" in these plots is ${\rm FAR}_\tau = 1/(30\ {\rm days})$, where τ indicates a threshold.

The number of "found" injections and their associated distances compared to the

total number of injections is used to calculate the *sensitive distance* of a search, which is roughly how far away the injection set signals can be detected in a real search. To do this, we first calculate the sensitive volume by performing an efficiency-weighted integration over b spherical shells of thickness Δd_i at a distance of d_i:

$$V_{\rm s}(\tau) = \sum_{i}^{b} 4\pi\epsilon_i(\tau) d_i^2 \Delta d_i, \tag{3.3.1}$$

where the efficiency in the $i^{\rm th}$ shell is defined to be

$$\epsilon_i(\tau) = \frac{\text{number of ``found'' injections in } i^{\rm th} \text{ bin}}{\text{total number of injections in } i^{\rm th} \text{ bin}} = \frac{N_{{\rm found},i}}{N_{{\rm tot},i}}, \tag{3.3.2}$$

which is a function of the threshold. Then, the sensitive distance is just

$$D_{\rm s}(\tau) = \left[\frac{3V(\tau)}{4\pi}\right]^{1/3}. \tag{3.3.3}$$

The uncertainty in the efficiency due to the finite number of injections in each distance bin, which is estimated by modeling the efficiency with a binomial distribution, is propagated through the sensitive volume and into the sensitive distance like so:

$$\sigma_{D_{\rm s}} = \frac{1}{3} D_{\rm s} \frac{\sigma_{V_{\rm s}}}{V_{\rm s}}, \tag{3.3.4}$$

where

$$\sigma_{V_{\rm s}} = \sqrt{\sum_{i}^{b} (4\pi\sigma_{\epsilon_i} d_i^2 \Delta d_i)^2} \tag{3.3.5}$$

and

$$\sigma_{\epsilon_i} = \sqrt{\frac{\epsilon_i(1-\epsilon_i)}{N_{{\rm tot},i}}}. \tag{3.3.6}$$

So, the sensitive distances in Fig. 16 are computed through Eq. (3.3.3) with an uncertainty estimated by Eq. (3.3.4) and are a function of whatever threshold is used to separate "missed" and "found" triggers associated with the injection sets.

Waveform handling

For the most part, we found that `gstlal_inspiral` was effective at searching for IMBHB signals (to skip straight to these results, see Figs. 15 and 16). However, since `gstlal_inspiral` was originally developed to search for long BNS signals, it was not too

surprising that we did run into problems with the way the high-mass 150:150 waveforms were being handled. In particular, methods for conditioning the beginning of the waveforms and choices regarding what f_{low} should be used for waveform generation had to be adjusted for searching over the IMBHB parameter space.

We initially decided that generating waveforms at a lower frequency of $f_{\text{low}} = 25$ Hz would be low enough that, after whitening the data and the templates as described in Sec. 3.2.3, the beginning of the waveform would be overtaken by the noise at lower frequencies. This seemed reasonable considering the ASD at 25 Hz is roughly one order in magnitude above the noise floor (see Fig. 13). For this reason, we did not even bother to taper the beginning of our waveforms before injecting them into the data. However, as shown in Fig. 13, a 150:150 IMBHB injection starting at 25 Hz located ∼800 Mpc away abruptly starts above the noise amplitude. Therefore, an unnatural feature was introduced at the beginning of each high-mass injection after Fourier transforming the data to whiten it and inverse Fourier transforming the data back into the TD to perform the SNR calculation. This is a manifestation of the Gibbs phenomenon that is typically avoided by either tapering the start of injections or injecting at a low enough frequency that the large noise amplitude makes the discontinuity is insignificant. However, the templates used in our search were tapered and therefore did not experience this effect. As a result, the autochisq statistic was negatively affected by the unnatural mismatch between our templates and injections, and the search sensitivity for high-mass signals was poor.

Even though the templates we used were tapered, the search sensitivity still suffered from them being generated starting at $f_{\text{low}} = 25$ Hz. Tapering is typically applied over the first few waveform peaks. However, as shown in Fig. 11, a 150:150 signal starting at $f_{\text{low}} = 25$ Hz only has a couple large amplitude cycles. Therefore, tapering over the first few peaks noticeably reduces the SNR recovery of high-mass templates. We demonstrate this effect in Fig. 14. Notice that templates starting at 25 Hz that get tapered and subsequently whitened have noticeably less amplitude in their first few peaks than if they were not tapered.

To account for our original oversights in the waveform handling, we reran the search

with tapered injections that start at 10 Hz and tapered templates that start at 20 Hz. We started our injections at the very low starting frequency of 10 Hz to be sure that the waveforms started out-of-band. However, there frequency at which we start our templates affects the number of templates in our template bank. We found that the search sensitivity was insignificantly affected by pushing the starting frequency of our templates below 20 Hz. This is because tapering has a minimal effect on the amplitude of our waveform if we start them at 20 Hz, as shown in the middle plot of Fig. 14.

MDC1 results

In Figs. 15 and 16 we show the results of our search before and after accounting for waveform handling issues. It is clear that the sensitivity to the 150:150 injections was hurt the most by the waveform handling issues, the sensitivity to the 50:50 injections was slightly affected, and the sensitivity to the 5:50 injections felt mostly insignificant effects. This makes sense in two ways. Firstly, the lower mass signals have lower amplitudes at near-detection threshold SNRs, and therefore when they are injected to abruptly start in-band, the resulting Gibbs phenomenon feature will be less noticeable. Secondly, the lower mass signals are much longer, and therefore tapering out some amplitude in the first few peaks of the waveform does not have as dramatic of an effect on these signals.

More recently, we have incorporated a function into our waveform generation routines that, given an $f_{\rm low}$, generates a waveform starting at a lower frequency and tapers up to $f_{\rm low}$. This ensures that our injection and template waveforms will be free of any Gibbs effects and will not lose any signal power due to tapering.

3.3.2 MDC2

We are currently working through a second MDC. The purpose of MDC2 is to test the effects of spin and precession in IMBHB sources. Since little is known about IMBHBs and their formation mechanisms, while we expect these systems to be spinning, it is unclear whether to expect their component spins to be aligned/anti-aligned or to expect the systems to be precessing [37]. Additionally, we will be testing the effects of waveform uncertainty by using different waveform families for injections and templates.

Preliminary results suggest that the sensitive distance to the 150:150 and the 50:50 injections with aligned spin are roughly comparable to our MDC1 results. A few factors are at play here. Firstly, all else being equal, the aligned-spin (anti-aligned spin) systems of MDC2 can be seen to slightly larger (smaller) distances compared to the non-spinning injections of MDC1 [37; 48; 49]. Secondly, our non-spinning template bank is not expected to be completely effectual to spinning systems. Therefore our MM condition might not be conserved, resulting in less sensitivity to these sources. Thirdly, for MDC2, we are using a more sophisticated likelihood ratio than the one described in Sec. 3.2.5, which results in increased sensitivity [50].

Preliminary results however show a sharp drop in sensitive distance for the 5:50 injections for large aligned-spin values. While this feature is still being investigated, sensitive distance can be restored by using an aligned-spin template bank. Indeed, preliminary results show that an aligned-spin bank has roughly the same or better sensitivity across each injection set. However, extending to an aligned-spin bank adds an order of magnitude more templates to the bank (from ∼1,000 to ∼10,000 templates), resulting in a more computationally expensive search. The question then becomes "Does the benefit of an aligned-spin bank outweigh the cost?" Further investigations are underway in an effort to decide whether or not to perform the IMBHB search with an aligned-spin template bank.

3.4 Conclusion and discussion

A CBC search for IMBHBs may result in the first conclusive proof of the existence of IMBHs. This would be an extraordinary discovery that would shed light on supermassive BH formation, globular cluster dynamics, strong-field GR, and much more. A `gstlal_inspiral` search for IMBHBs is a relatively inexpensive search, since a non-spinning bank will only consist of ∼1,000 templates. In MDC1, we showed that advanced detectors in early configurations can see IMBHBs out to sensitive distances ranging from ∼100 Mpc for light binaries to ∼1,000 Mpc for heavy binaries. However, we have only demonstrated the search sensitivity to non-spinning systems. We are currently working through a second MDC that will test the search sensitivity for highly spinning and/or

precessing systems.

We have learned the importance of proper waveform handling for analysis involving high-mass signals, such as IMBHBs. In particular, we saw that tapering the first few cycles of a short, high-mass waveform can noticeably decrease its power. Instead, templates and injections should be generated at lower frequencies than requested and tapered up to such frequencies to ensure that the signals maintain full power at the intended lower frequency band. Otherwise an IMBHB search is less sensitive to high-mass signals.

Preliminary results in MDC2 also suggest a transition to an aligned-spin bank. Since such a transition results in an order of magnitude more templates, more investigations are being performed to weigh our options going forward.

Eventually, we will have to explore the entire search mass parameter space in a subsequent MDC or as part of an engineering run (ER). An ER is an end-to-end test of data collection at the instruments through the announcement of GW event candidates. In the upcoming ER, we could run the IMBHB search on real detector data. Not only is this the first time we will be able to test our search on aLIGO data, which might have different and unexpected characteristics compared to the recolored S6 data that we have used so far, but this data is also forecasted to have the best sensitivity to date, even eclipsing the mark set by S6.

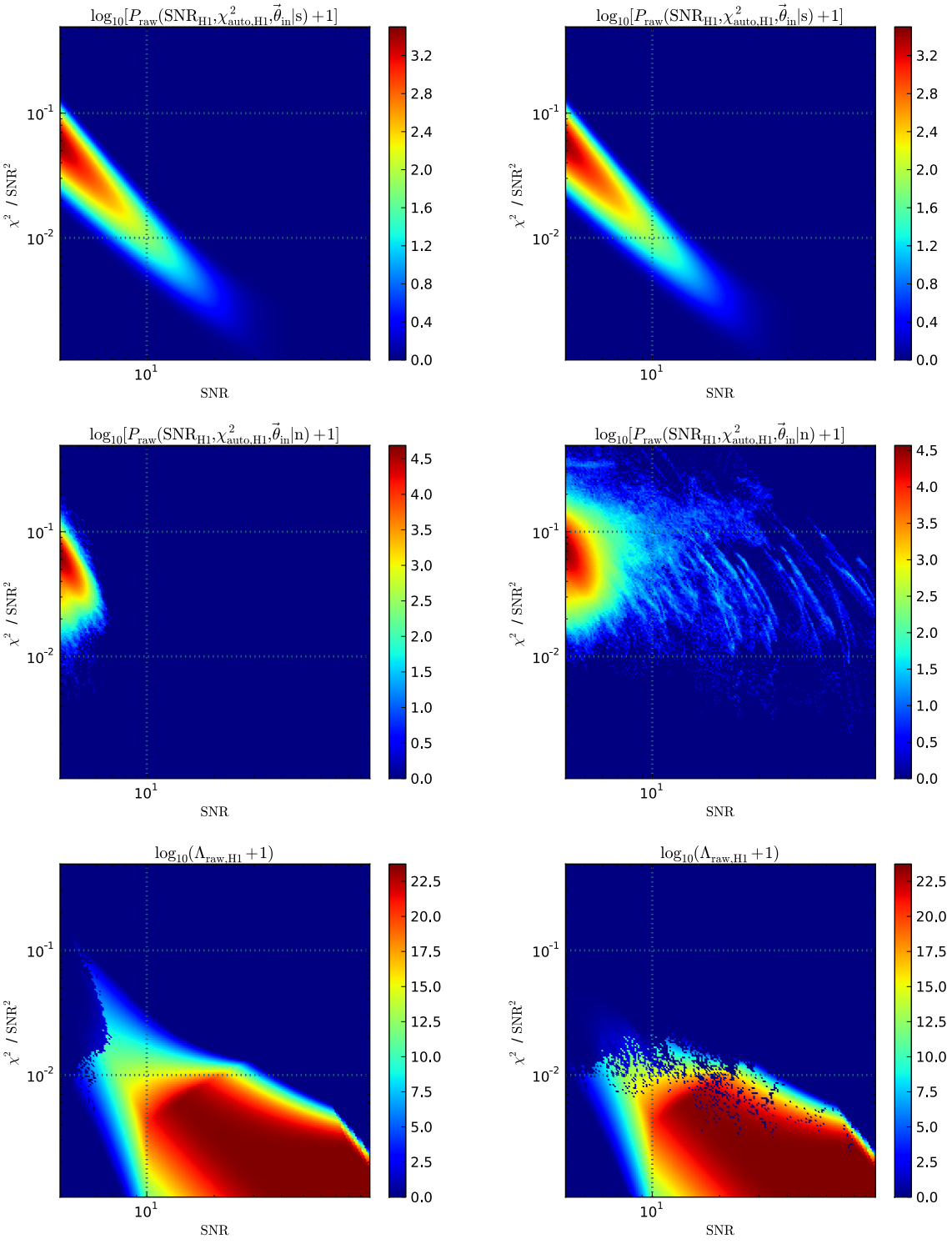

Figure 10 : The likelihood ratio $\Lambda_{\rm H1}$, its numerator $P(\mathrm{SNR}_{\rm H1},\chi^2_{\rm auto,H1},\vec{\theta}_{\rm in}|\mathrm{s})$, and its denominator $P(\mathrm{SNR}_{\rm H1},\chi^2_{\rm auto,H1},\vec{\theta}_{\rm in}|\mathrm{n})$ are plotted as 2D histograms in raw counts on $\chi^2_{\rm auto}/\mathrm{SNR}^2$ versus SNR axes. The left plots were generated with Gaussian data, and the right plots were generated with recolored S6 data. The top plots are the numerators of the likelihood ratios, the middle plots are the denominators of the likelihood ratios, and the bottom plots are the likelihood ratios.

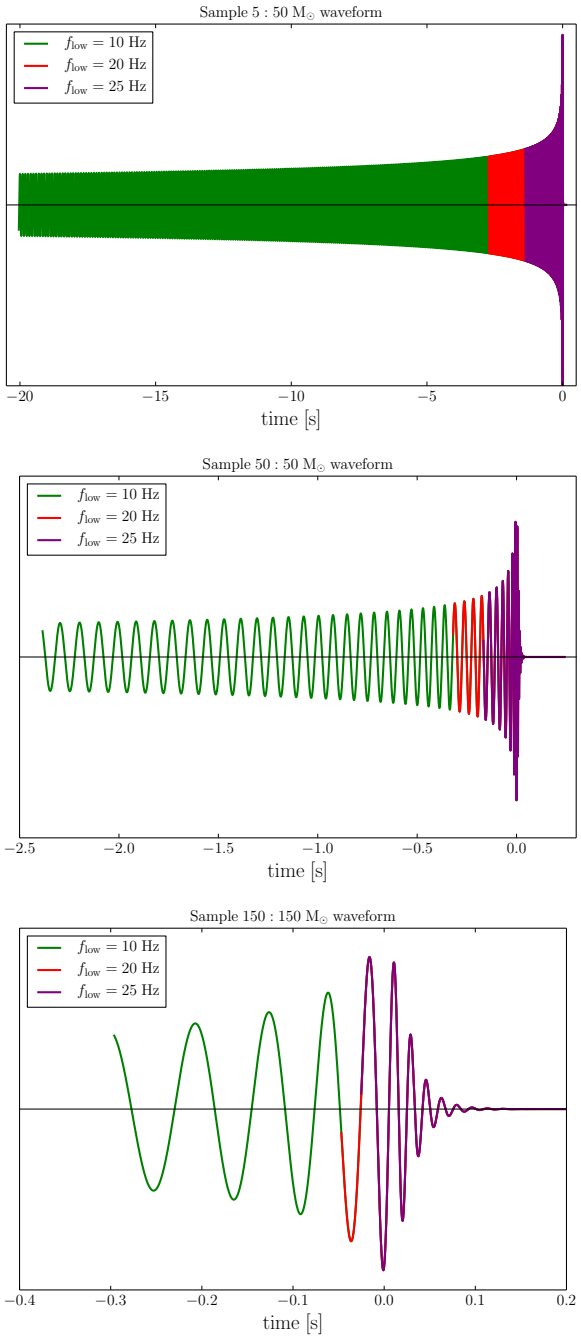

Figure 11 : Plots of h_+ for 5:50 (top), 50:50 (middle), and 150:150 (bottom) systems with EOBNRv2 generation at $f_{\rm low} = 25$ (purple), 20 (red), and 10 (green).

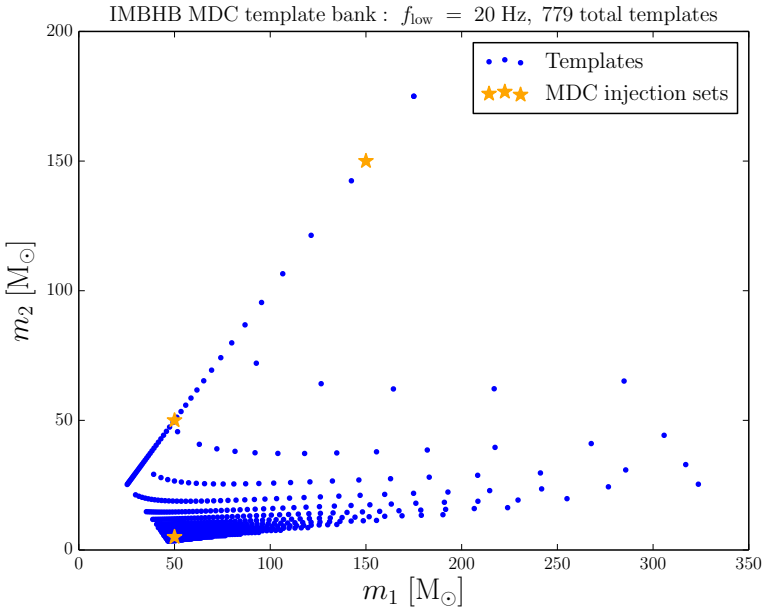

Figure 12 : Non-spinning MDC1 template bank. The blue dots mark the template placement in mass space, and the orange stars mark the narrow mass distributions of the injections used in MDC1.

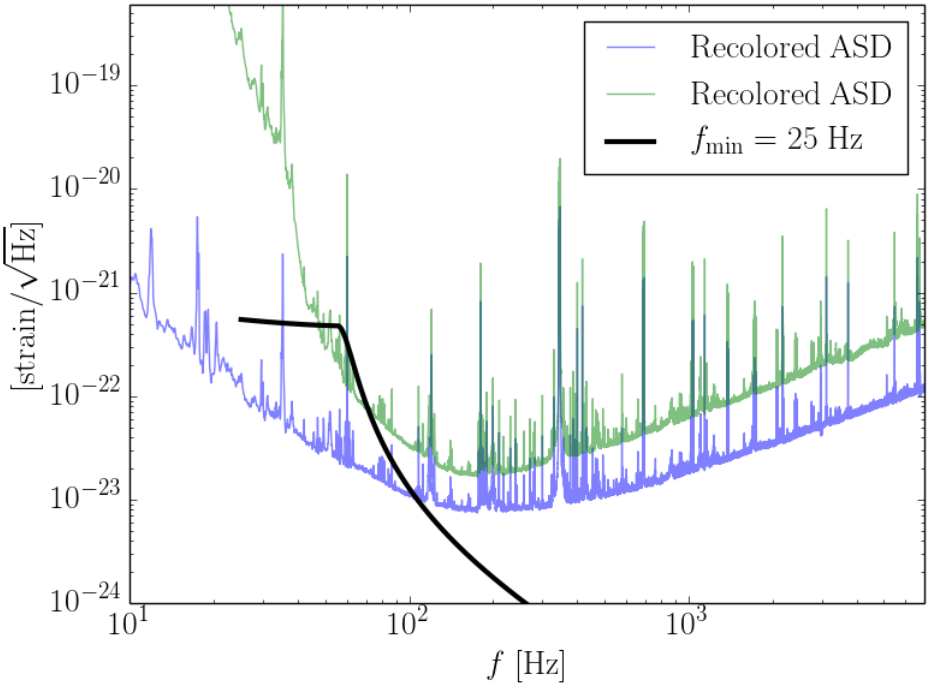

Figure 13 : ASDs for data from S6 and S6 data recolored to an anticipated early aLIGO ASD. Plotted is the characteristic amplitude $h_c = \sqrt{f} \cdot |\tilde{h}(f)|$ for an IMBHB with 150 M$_\odot$ component masses at a distance of $D \sim 800$ Mpc generated starting at 25 Hz.

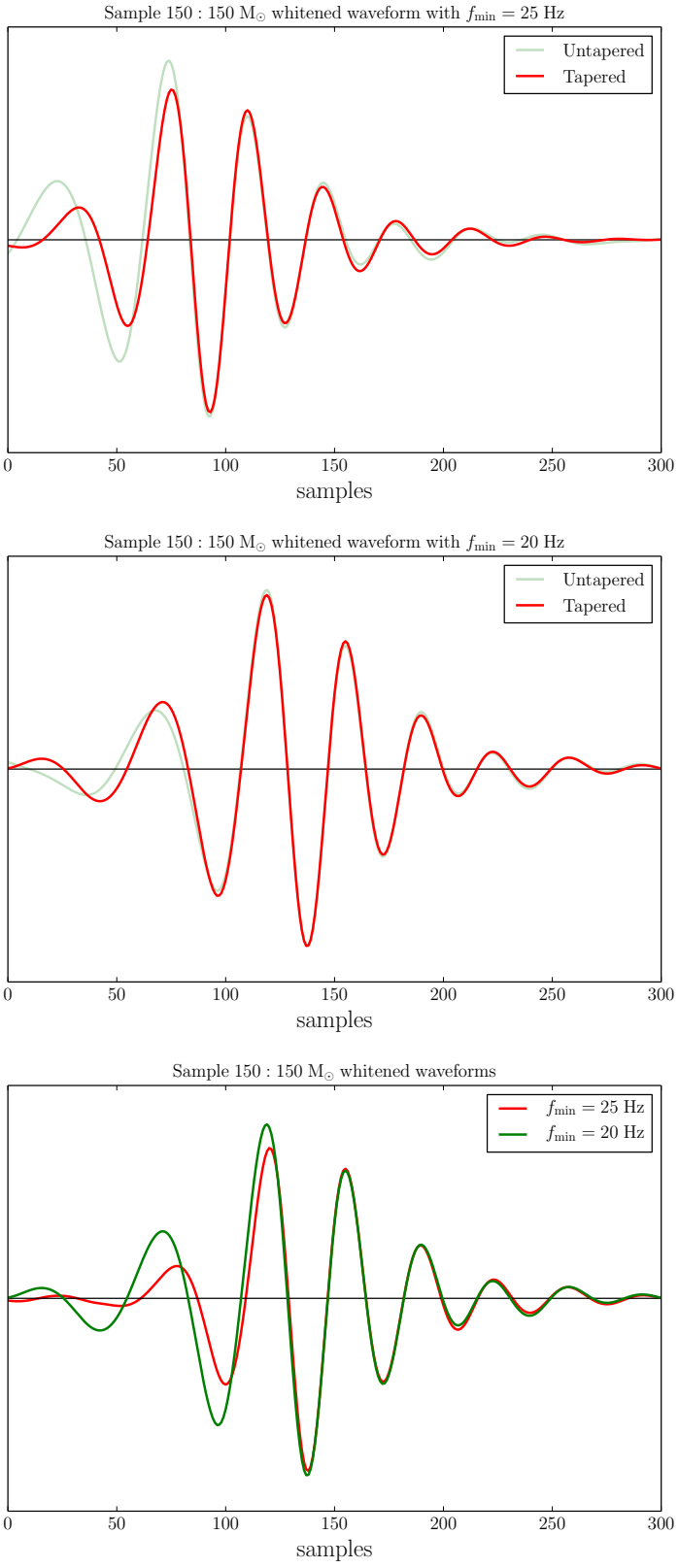

Figure 14 : Plotted are whitened 150:150 waveforms generated starting at either 20 or 25 Hz. The top two plots compare tapered with untapped waveforms, and the bottom plot compares tapered waveforms with different minimum frequencies.

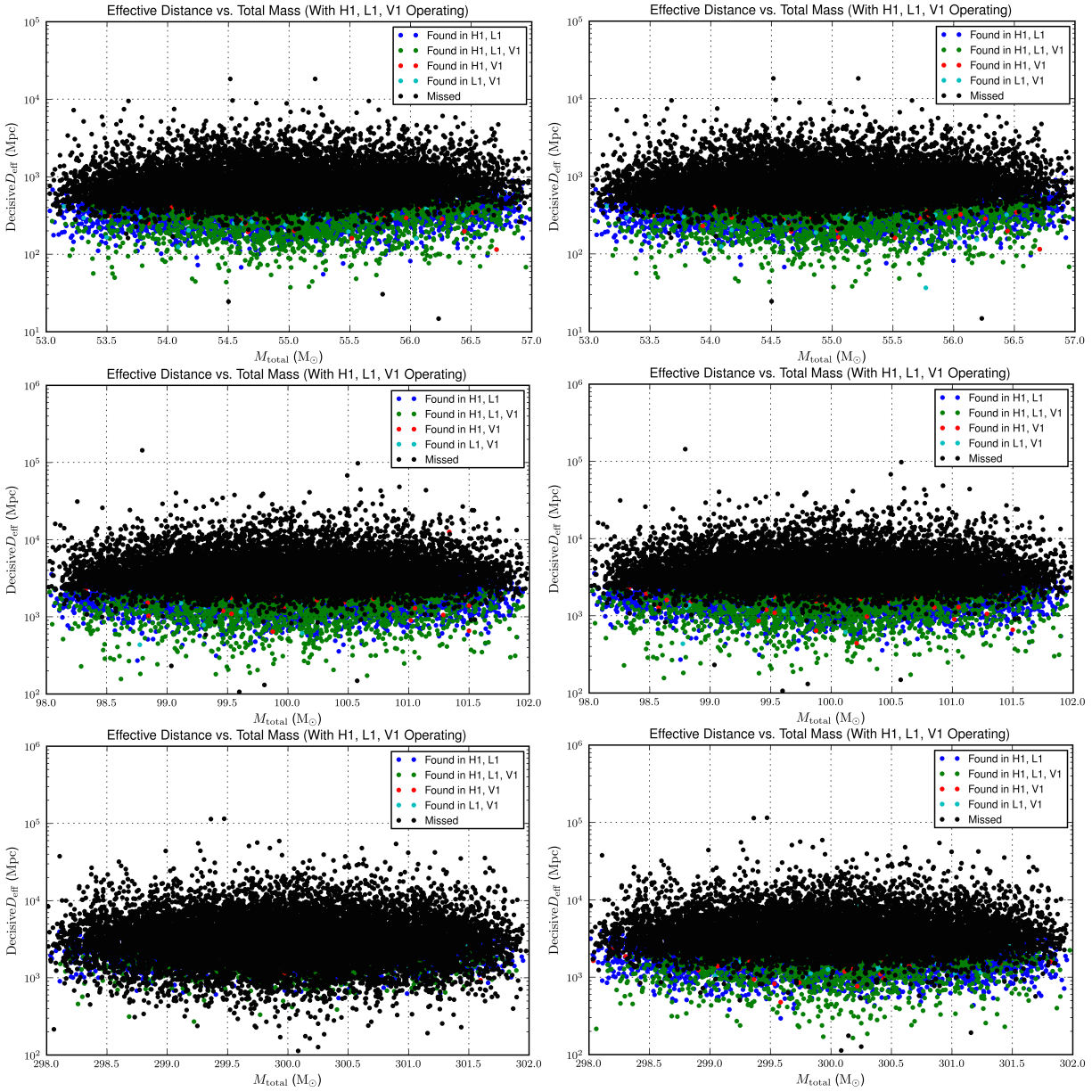

Figure 15 : Missed/Found plots comparing the effects of waveform handling. The dots represent injected signals. Black dots are missed signals, and colored dots are signals found coincident in a certain combination of instruments as labeled in the legend. Decisive $D_{\rm eff}$ refers to the second smallest single-detector $D_{\rm eff}$. The distinction between Missed and Found is made through a FAR threshold of 1/(30 days). (Left) Results from a search in which we used templates generated starting from 25 Hz and injected untapped signals generated starting from 25 Hz. (Right) Results from the same search except that we generated templates starting from 20 Hz and injected tapered signals generated starting from 10 Hz.

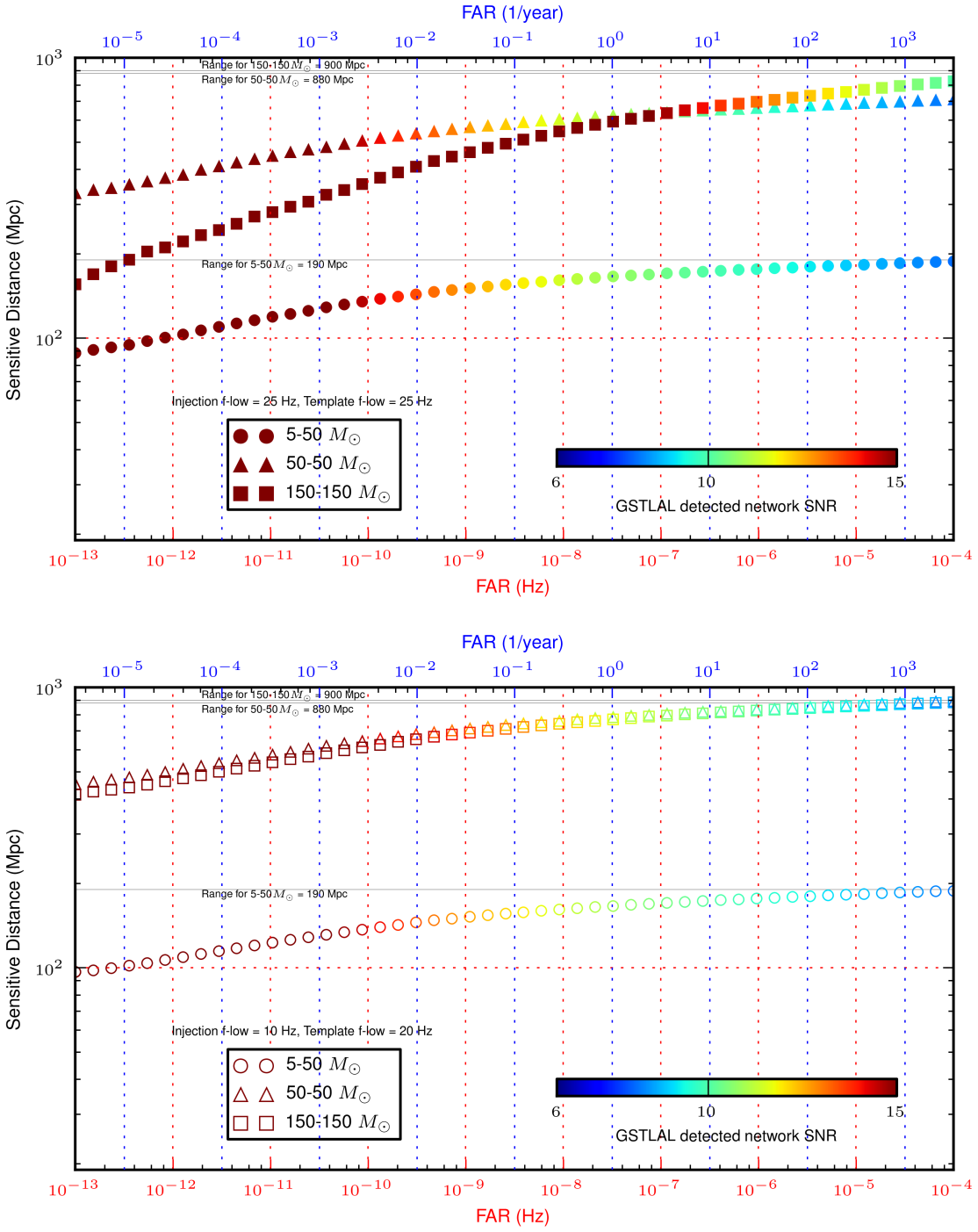

Figure 16 : Sensitive distance plots for MDC1. (Top) Results from a search in which we used templates generated starting from 25 Hz and injected untapped signals generated starting from 25 Hz. (Bottom) Results from the same search except that we generated templates starting from 20 Hz and injected tapered signals generated starting from 10 Hz.

Chapter 4

Systematic and statistical errors in a bayesian approach to the estimation of the neutron-star equation of state using advanced gravitational-wave detectors[1]

4.1 Background and Motivation

Advanced interferometric gravitational-wave (GW) detectors currently under construction are expected to begin operating in the next few years. Advanced LIGO [52] is expected to achieve its design sensitivity c. 2019 [8], at which time the detection rate of binary neutron-star (BNS) events in a single detector is expected to be $\sim$40 yr^{-1}, though this value is quite uncertain and ranges from 0.4–400 yr^{-1} [53].

When a compact binary coalescence (CBC) signal is detected [54; 55], the corresponding interferometer data stream segment is sent through a parameter estimation pipeline to determine the source parameters of the system. Some of these source parameters include the binary component masses and spins, the sky location, distance, and orientation of the

[1]This chapter was published in Ref. [51]

system. Bayesian inference is used to explore the probability distribution of the CBC's source parameters by comparing model waveform templates, whose form depends on these source parameters, to the data stream segment containing the GW. For this work, we use `lalinference_mcmc`, which is included in the `LALInference` LSC Algorithm Library [47], as our parameter estimation pipeline. It is a Markov Chain Monte Carlo (MCMC) sampler designed to efficiently explore the full waveform parameter space in order to make reliable and meaningful statements about CBC source parameters [56–58].

This chapter's focus is on measuring the effect of tidal influence on BNS GW signals with advanced detectors. Neutron stars (NSs) in merging CBC systems will be tidally deformed by the gravitational gradient of their companion across their finite diameter. This effect is insignificant at large separations but becomes increasingly significant as the NSs near each other [59]. The internal structure of a NS, which is characterized by its equation of state (EOS), determines how much each star will deform. The amount that a NS deforms will affect the orbital decay rate, which is encoded in the observed gravitational waveform. Therefore, if a gravitational signal from a BNS system is detected, then such a detection could provide insight into the NS EOS [59–62].

In order to make meaningful statements regarding the recoverability of tidal parameters from BNS signals, it is important to understand the effects of error on parameter estimation. One such obstacle to measuring tidal influence is accurate waveform modeling. The error resulting from inaccurate waveform models is a kind of systematic error. Some of the most commonly used CBC waveforms rely on a post-Newtonian (PN) expansion in orbital speed. As the CBC inspirals, the orbital speed of the binary components increases leading to a higher frequency signal. These waveform families are thus unreliable at high frequencies where orbital speeds become large [10] and tidal effects emerge. Another difficulty in measuring tidal influence results from fluctuations in detector noise. This type of error is called statistical error. Tidal influences only noticeably affect the final high frequency orbits of the binary where the detector noise (in strain units) is comparatively large. Extracting such a small influence occurring in the high frequency band is an investigation at the very brink of our detectors' sensitivity. Even small fluctuations in detector noise might be able to dramatically affect the recovery of tidal deformability.

Understanding the magnitude of these two sources of error is the core motivator of this work.

Several studies have used the Fisher Information Matrix (FM), which is only valid in the large signal-to-noise ratio (SNR) limit, to estimate the measurability of tidal effects on the CBC gravitational waveform [59–61; 63–66]. Flanagan and Hinderer [59] were among the first to show that advanced detectors can constrain the tidal influence of NSs on the early inspiral portion of the CBC waveform. They notably use PN waveforms truncated at 400 Hz to remove the unreliable high-frequency portion of the PN model. Hinderer *et al.* [60] later investigated how well constraints on the tidal deformability from the early inspiral can discriminate between several theoretical NS EOSs. Also using PN waveforms, they find that advanced detectors will likely only be able to probe stiff EOSs.

Further FM studies moved away from the use of PN waveforms in favor of waveforms that are more reliable at high frequencies. Read *et al.* [61; 63] probed the late inspiral portion of the BNS waveform with numerical relativity (NR) simulations, which are accurate during the late inspiral and merger epochs. They find that the additional high frequency information results in greater measurement accuracy of the tidal deformability. Damour, Nagar, and Villain [65] also probed beyond the early inspiral with tidally corrected effective-one-body (EOB) waveforms, which they claim to be accurate up to merger. They show that advanced detectors should in fact be able to constrain the NS EOS for reasonably loud signals.

While the above mentioned studies are informative, the FM is not always trustworthy in estimating the measurability of source parameters [67–70]. Though it is known that FM estimates are only accurate for loud signals, recent investigations have highlighted additional shortcomings of FM estimates when compared to real GW parameter estimation pipelines [68]. It is now clear that there is no substitute for full Bayesian results when making definitive statements regarding parameter estimation.

Del Pozzo *et al.* [71] recently performed Bayesian simulations of BNS systems with a tidally corrected PN waveform. They find that advanced detectors will be able to measure tidal effects on GW signals and constrain the NS EOS by combining information from many BNS sources. While this result is very important, their analysis assumes that true

BNS signals have the exact same form as their model. Although the authors acknowledge this limitation, it is necessary to study how much their result depends on this assumption.

Recently, there have been several FM investigations that have studied the effects of systematic error on the measurability of tidal parameters [63; 64; 72; 73]. In particular, Yagi and Yunes in [72] and Favata in [73] both find that current PN waveforms, which are known only up to 3.5PN order [10], cannot be used to make accurate measurements of tidal effects. This is an extremely important result that motivates a full Bayesian investigation into the effect of systematic error from tidally corrected PN waveforms on parameter estimation.

In this work, we use a full Bayesian framework to demonstrate the ability of advanced detectors to constrain the NS EOS by measuring the effects of tidal influence on BNS signals. We estimate the anticipated measurement uncertainty associated with using the advanced LIGO/Virgo network [52; 74] to recover tidal influence in BNS systems. We find that systematic error inherent in the current PN inspiral waveform families significantly biases the recovery of tidal parameters. Additionally, we find that individual instances of detector noise can on occasion considerably reduce the measurability of tidal parameters. We consider only BNS systems.

This work is organized as follows. In Sec. 4.2 we review how tidal influences affect the CBC waveform. In Sec. 4.3 we briefly outline the parameter estimation pipeline used in this analysis and present measurement uncertainty estimates for the recovery of tidal influences in BNS systems. In Sec. 4.4 we explain how simultaneous mass-like and radius-like measurements, specifically the measurement of chirp mass and tidal deformability, can help constrain the NS EOS. In Sec. 4.5 we describe the two main sources of error in parameter estimation and how much each source of error affects the recovery of tidal parameters. We finish with a summary of our main results in Sec. 4.6. We also refer the interested reader to Appendix 4.A where we derive how the tidal corrections appear in several PN waveform families.

4.2 Tidal Corrections to CBC PN Waveform Families

In this section, we review the effects of tidal influences on the CBC waveform. For a more complete discussion, refer to Appendix 4.A, which outlines how tidal effects appear in the following PN waveform families: TaylorT1, TaylorT2, TaylorT3, TaylorT4, and TaylorF2. For more details regarding each of these waveform families, see [10] and references therein.

4.2.1 Constructing tidally corrected PN waveforms

To model the CBC waveform, it is customary to approximate each massive body as having infinitesimal size. As the two bodies orbit, GWs carry energy away from the system causing their separation to decrease and their orbital frequency to increase. The energy and luminosity of this point-particle system ($E_{\rm pp}$ and $L_{\rm pp}$ respectively) are currently known to 3.5 post-Newtonian (PN) order[2] [10].

If the two compact objects are NSs, each will start to deform under the tidal field of the other as their separation decreases. The deformation of each body will have an effect on the rate at which the bodies coalesce. BNS systems therefore depart from the point-particle approximation at high frequencies and require an additional correction to the energy and luminosity of the system relative to the point-particle terms.

Since a NS in a binary system will deform under the tidal influence of its companion, its quadrupole moment $\mathcal{Q}_{ij}$ must be related to the tidal field $\mathcal{E}_{ij}$ caused by its companion. For a single NS, to leading order in the quasi-stationary approximation and ignoring resonance,

$$\mathcal{Q}_{ij} = -\lambda \mathcal{E}_{ij}, \tag{4.2.1}$$

where $\lambda = (2/3)k_2 R^5/G$ parameterizes the amount that a NS deforms [59]. The i and j are spatial tensor indices, k_2 is the second Love number, and R is the NS's radius. Since λ parameterizes the severity of a NS's deformation under a given tidal field, it must depend on the NS EOS. NSs with large radii will more easily be deformed by the external tidal field, because there will be a more extreme gravitational gradient over their radius. For a fixed mass, NSs with large radii are also referred to as having a stiff EOS, and, for the

[2]The energy has recently been calculated to 4PN order [75].

same mass, NSs with small radii have a soft EOS. Therefore, NSs that have large values of λ will have large radii, a stiff EOS, and become severely deformed in BNS systems; on the other hand, NSs that have small values of λ will have small radii, a soft EOS, and will be less severely deformed in these systems.

Tidal effects are most important at small separations and therefore at high frequencies in BNS systems. Tidal corrections to the energy $\delta E_{\rm tidal}$ and tidal corrections to the luminosity $\delta L_{\rm tidal}$ add linearly to the point-particle energy $E_{\rm pp}$ and luminosity $L_{\rm pp}$. Though the leading order tidal correction is a Newtonian effect, it is often referred to as a 5PN correction, because it appears at 5PN order relative to the leading order point-particle term. In this work, we keep the leading order (5PN) and next-to-leading order (6PN) corrections to the energy and luminosity [76]:

$$\begin{aligned}
\delta E_{\rm tidal} &= -\frac{1}{2}c^2 M\eta x\left[-\left(\frac{9}{\chi_1}-9\right)\frac{c^{10}}{G^4}\frac{\lambda_1}{M^5}x^5\right. \\
&\left.-\left(\frac{33}{2\chi_1}-\frac{11}{2}+\frac{11}{2}\chi_1-\frac{33}{2}\chi_1^2\right)\frac{c^{10}}{G^4}\frac{\lambda_1}{M^5}x^6+(1\longleftrightarrow 2)\right] \qquad (4.2.2)\\
\delta L_{\rm tidal} &= \frac{32}{5}\frac{c^5}{G}\eta^2 x^5\left[\left(\frac{18}{\chi_1}-12\right)\frac{c^{10}}{G^4}\frac{\lambda_1}{M^5}x^5\right. \\
&\left.-\left(\frac{176}{7\chi_1}+\frac{1803}{28}-\frac{643}{4}\chi_1+\frac{155}{2}\chi_1^2\right)\frac{c^{10}}{G^4}\frac{\lambda_1}{M^5}x^6+(1\longleftrightarrow 2)\right]. \qquad (4.2.3)
\end{aligned}$$

The total mass is $M = m_1 + m_2$, where m_1 and m_2 are the component masses, $\eta = m_1 m_2/M^2$ is the symmetric mass ratio, $x = (\pi G M f_{\rm gw}/c^3)^{2/3}$ is the PN expansion parameter, $f_{\rm gw} = 2f_{\rm orb}$ is the GW frequency, $f_{\rm orb}$ is the binary's orbital frequency, and $\chi_1 = m_1/M$ and $\chi_2 = m_2/M$ are the two mass fractions. Note that the PN order is labelled by the exponent on x inside the square brackets, which is why these terms are referred to as 5PN and 6PN corrections. Since the 5PN and 6PN tidal correction coefficients multiply x^5 and x^6 respectively, these effects will be insignificant at low frequencies and increasingly more significant at higher frequencies ($x \sim f_{\rm orb}^{2/3}$), as anticipated. Appendix 4.A derives each tidally corrected PN waveform family from Eqs. (4.2.2) and (4.2.3).

The point-particle energy and luminosity are only known to 3.5PN order [10]. However, we add tidal corrections to the energy and luminosity that appear at 5PN and 6PN orders without knowing the higher order point-particle terms. The justification for including the tidal corrections has typically been that they are always associated with the

large coefficient $G\lambda_A[c^2/(Gm_A)]^5 \sim [c^2 R_A/(Gm_A)]^5 \sim 10^5$ [59]. Therefore, although they appear at high PN orders, the effect of the tidal terms on the binary's orbit are comparable to the effects of the 3PN and 3.5PN point-particle terms. However, this claim was contradicted in [72] because the tidal corrections are actually associated with the coefficient $[c^2 R/(GM)]^5 \sim 10^3 \ll [c^2 R_A/(Gm_A)]^5$, which is apparent from the form of Eqs. (4.2.2) and (4.2.3). We show in Sec. 4.5.1 that not knowing the higher order PN point-particle terms leads to significant systematic error when recovering tidal parameters. Yagi and Yunes in [72] and Favata in [73] also discuss the importance of these unknown point-particle terms.

4.2.2 Reparameterization of tidal parameters

It becomes convenient to reparameterize the tidal parameters (λ_1, λ_2) in terms of purely dimensionless parameters, which we call $(\tilde{\Lambda}, \delta\tilde{\Lambda})$ [73]. Inspired by the $\tilde{\lambda}$ from [59], $\tilde{\Lambda} = 32 G\tilde{\lambda}[c^2/(GM)]^5$ is essentially the entire 5PN tidal correction in all of the PN waveform families, while the 6PN tidal correction is a linear combination of $\tilde{\Lambda}$ and $\delta\tilde{\Lambda}$. For example, the tidal corrections to the TaylorF2 phase later derived in Eq. (4.A.6) of Appendix 4.A can equivalently be expressed as follows:

$$\delta\psi_{\rm tidal} = \frac{3}{128\eta x^{5/2}}\left[\left(-\frac{39}{2}\tilde{\Lambda}\right)x^5 + \left(-\frac{3115}{64}\tilde{\Lambda} + \frac{6595}{364}\sqrt{1-4\eta}\,\delta\tilde{\Lambda}\right)x^6\right], \tag{4.2.4}$$

where

$$\begin{aligned}\tilde{\Lambda} &= \frac{8}{13}\left[\left(1+7\eta-31\eta^2\right)(\Lambda_1+\Lambda_2)\right. \\ &\quad \left.+\sqrt{1-4\eta}\left(1+9\eta-11\eta^2\right)(\Lambda_1-\Lambda_2)\right] \qquad (4.2.5)\\ \delta\tilde{\Lambda} &= \frac{1}{2}\left[\sqrt{1-4\eta}\left(1-\frac{13272}{1319}\eta+\frac{8944}{1319}\eta^2\right)(\Lambda_1+\Lambda_2)\right. \\ &\quad \left.+\left(1-\frac{15910}{1319}\eta+\frac{32850}{1319}\eta^2+\frac{3380}{1319}\eta^3\right)(\Lambda_1-\Lambda_2)\right]. \qquad (4.2.6)\end{aligned}$$

The dimensionless parameters $\Lambda_1 = G\lambda_1[c^2/(Gm_1)]^5$ and $\Lambda_2 = G\lambda_2[c^2/(Gm_2)]^5$, and we have assumed that $m_1 > m_2$. Though we choose to express $\tilde{\Lambda}$ and $\delta\tilde{\Lambda}$ in terms of dimensionless parameters as in Eqs. (4.2.5) and (4.2.6), they can be equivalently expressed more compactly in terms of dimensionful parameters, as can be inferred from Eq. (4.A.6). The

parameters $(\tilde{\Lambda}, \delta\tilde{\Lambda})$ were chosen such that they have the following convenient properties:

$$\tilde{\Lambda}(\eta = 1/4, \Lambda_1 = \Lambda_2 = \Lambda) = \Lambda \tag{4.2.7}$$

$$\delta\tilde{\Lambda}(\eta = 1/4, \Lambda_1 = \Lambda_2 = \Lambda) = 0. \tag{4.2.8}$$

Setting $\eta = 1/4$ implies that $m_1 = m_2$. Since all cold NSs have the same EOS [77], spherical NSs with the same mass will also have the same value for Λ. We have over-specified Eqs. (4.2.7) and (4.2.8) for clarity. We refer to $\tilde{\Lambda}$ as the *tidal deformability* of a BNS system throughout this work. For more details regarding this reparameterization, see [73].[3]

4.3 Measurability of Tidal Influence

In this work, we use `lalinference_mcmc` to run full Bayesian simulations for our parameter estimation investigation into the measurability of tidal deformability. `lalinference_mcmc` uses an MCMC sampling algorithm to calculate the posterior probability density function (PDF) of a detected CBC signal. The algorithm is designed to efficiently explore a multi-dimensional parameter space in such a way that the density of parameter samples is a good approximation to the underlying posterior distribution. In this section, we briefly outline the algorithm used by `lalinference_mcmc`. For a more comprehensive overview, we refer the reader to Refs. [56–58].

4.3.1 MCMC overview

A true GW signal will be buried in detector noise. Given a GW detection, the data stream segment $d(t)$ will have the following form in the time-domain:

$$d(t) = h_{\rm GW}(t) + n(t). \tag{4.3.1}$$

The detector noise is denoted $n(t)$ while the pure GW signal is denoted $h_{\rm GW}(t)$. Since no GWs have yet been detected by ground-based interferometers, our studies require simulated signals. It is therefore customary to inject a modeled signal with chosen parameters

[3]Note that, relative to [73], we have pulled out a factor of $\sqrt{1-4\eta}$ from our definition of $\delta\tilde{\Lambda}$ to allow for nonzero values of $\delta\tilde{\Lambda}$ when $\eta = 1/4$. This distinction enables the MCMC algorithm to fully explore the $\delta\tilde{\Lambda}$ parameter space even for equal mass systems.

into synthetic noise.

To determine the physical properties of a CBC system, we seek to map out the functional form of the posterior probability distribution (*posterior* for short) of its parameters. Bayes' theorem relates the posterior $p(\vec{\theta}|d,\mathcal{H},\mathcal{I})$ for a set of waveform parameters $\vec{\theta}$ given a hypothesis $\mathcal{H}$, any background information $\mathcal{I}$, and a data stream segment $d(t)$ to the prior probability distribution (*prior* for short) and the likelihood $p(d|\vec{\theta},\mathcal{H},\mathcal{I})$:

$$p(\vec{\theta}|d,\mathcal{H},\mathcal{I}) = \frac{p(\vec{\theta}|\mathcal{H},\mathcal{I})p(d|\vec{\theta},\mathcal{H},\mathcal{I})}{p(d|\mathcal{H},\mathcal{I})} \tag{4.3.2}$$

$$\propto p(\vec{\theta}|\mathcal{H},\mathcal{I})\mathcal{L}(d|\vec{\theta},\mathcal{H},\mathcal{I}). \tag{4.3.3}$$

The notation $p(a|b)$ means the probability density of a given b. To be more specific, the hypothesis here represents the waveform model $h_{\mathcal{H}}$. The posterior is then the probability that the GW source modeled by the waveform $h_{\mathcal{H}}$ that produced the data stream segment $d(t)$ has the physical properties $\vec{\theta}$. The prior $p(\vec{\theta}|\mathcal{H},\mathcal{I})$ is the *a priori* probability that the system modeled by $h_{\mathcal{H}}$ has the physical properties $\vec{\theta}$. The prior reflects everything that we know about the physical properties of any CBC system before attempting to determine the parameters of a specific source. The evidence $p(d|\mathcal{H},\mathcal{I})$ is the probability of observing the data stream segment $d(t)$ with the model $h_{\mathcal{H}}$. The evidence is a normalization factor that can be used to compare how well different models would produce the data. The likelihood $\mathcal{L}(d|\vec{\theta},\mathcal{H},\mathcal{I}) = p(d|\vec{\theta},\mathcal{H},\mathcal{I})$ is the probability of observing the data stream segment $d(t)$ assuming the system that produced it is modeled by $h_{\mathcal{H}}$ and has the physical properties $\vec{\theta}$. The likelihood is a measure of how well the model $h_{\mathcal{H}}$ with parameters $\vec{\theta}$ matches the data stream segment $d(t)$. Assuming the noise is stationary and Gaussian, the functional form of the likelihood when using a single detector n is [16; 78]

$$\mathcal{L}_n(d|\vec{\theta},\mathcal{H},\mathcal{I}) \propto \exp\left[-2\int_0^\infty \frac{\left|\tilde{d}_n(f)-\tilde{h}_{\mathcal{H}}(f,\vec{\theta})\right|^2}{S_n(f)}df\right]. \tag{4.3.4}$$

$S_n(f)$ is the one-sided noise power spectral density (PSD), $\tilde{d}_n(f)$ is the Fourier transform of the detector data stream segment, and $\tilde{h}_{\mathcal{H}}(f,\vec{\theta})$ is a frequency-domain model for the waveform. When using a network of GW detectors, the posterior probability becomes

$$p(\vec{\theta}|d,\mathcal{H},\mathcal{I}) \propto p(\vec{\theta}|\mathcal{H},\mathcal{I})\prod_n \mathcal{L}_n(d|\vec{\theta},\mathcal{H},\mathcal{I}). \tag{4.3.5}$$

The MCMC algorithm used draws samples from the underlying posterior distribution $p(\vec{\theta}|d,\mathcal{H},\mathcal{I})$. The samples can be binned to produce a histogram of the full multi-dimensional posterior distribution. Posterior PDFs of fewer dimensions can be produced by marginalizing the full posterior over parameters that are not of interest. For example, a 1D PDF for the tidal deformability $\tilde{\Lambda}$ can be found by integrating the posterior over all the other parameters:

$$p(\tilde{\Lambda}|d,\mathcal{H},\mathcal{I}) = \int_{\vec{\theta}_{\rm other}} p(\vec{\theta}|d,\mathcal{H},\mathcal{I}) d\vec{\theta}_{\rm other}, \tag{4.3.6}$$

where $\vec{\theta}_{\rm other}$ are all the parameters in the set $\vec{\theta}$ except $\tilde{\Lambda}$. However, since the MCMC samples follow the posterior distribution, this integral is easily solved by simply binning only the parameters of interest (in this case $\tilde{\Lambda}$).

Various aspects of this algorithm have been fine-tuned to optimize speed and robustness and are outlined in Ref. [79]. This section is meant to merely provide an adequate overview of the parameter estimation pipeline used in this work. We refer the interested reader to the following sources for more details [56–58].

4.3.2 Models, Parameters, and Priors

Eq. (4.3.3) is used to calculate the posterior $p(\vec{\theta}|d,\mathcal{H},\mathcal{I})$, which is the quantity of interest, from the prior $p(\vec{\theta}|\mathcal{H},\mathcal{I})$ and likelihood $\mathcal{L}(d|\vec{\theta},\mathcal{H},\mathcal{I})$. It depends on a model $h_{\mathcal{H}}$, the model source parameters $\vec{\theta}$, and the prior distribution of each parameter. The waveform models used in this work are the following tidally corrected PN waveform families, which we outline in Appendix 4.A: TaylorT1, TaylorT2, TaylorT3, TaylorT4, and TaylorF2. To focus on purely EOS effects, we consider non-spinning BNS systems with no amplitude corrections. (Parameter estimation can be just as easily performed with spinning waveforms, though slightly larger uncertainties in $\tilde{\Lambda}$ may arise for NSs with significant spins.) These assumptions lead to the following 11-dimensional parameter space:

$$\vec{\theta} = \{\mathcal{M}_{\rm c}, q, \tilde{\Lambda}, \delta\tilde{\Lambda}, D, \iota, \alpha, \delta, \phi_{\rm ref}, t_{\rm ref}, \psi\}. \tag{4.3.7}$$

These parameters are: the chirp mass $\mathcal{M}_{\rm c} = \eta^{3/5}M$, the mass ratio $q = m_2/m_1$ where $m_1 > m_2$, the distance to the binary D, the angle between the line of sight and the orbital

axis ι, the right ascension and declination of the binary α and δ, the GW's polarization angle ψ, and the arbitrary reference phase and time $\phi_{\rm ref}$ and $t_{\rm ref}$. Since Λ_1 and Λ_2 are highly correlated, we choose to parameterize in terms of $\tilde{\Lambda}$ and $\delta\tilde{\Lambda}$. It is known that $\tilde{\Lambda}$ is comparatively more measurable than Λ_1 and Λ_2 individually [59; 60]. We use a uniform prior distribution in component masses between $1\ {\rm M}_\odot \leq m_2 \leq m_1 \leq 30\ {\rm M}_\odot$, a uniform prior distribution in volume to $D \leq 200$ Mpc[4], an isotropic prior distribution in sky location (α, δ) and emission direction $(\phi_{\rm ref}, \iota)$, a uniform prior distribution in polarization angle ψ, and a uniform prior distribution in $t_{\rm ref}$ over the data stream segment. We use a uniform prior distribution in $\tilde{\Lambda}$ between $0 \leq \tilde{\Lambda} \leq 3000$ and a uniform prior distribution in $\delta\tilde{\Lambda}$ between $-500 \leq \delta\tilde{\Lambda} \leq 500$. These ranges were chosen to include effects from the majority of possible NS EOSs.[5]

Since we are concerned only with measuring EOS effects on BNS signals, we fixed all the injected signals to have the exact same sky position ($\alpha = 0.648522$ and $\delta = 0.5747465$), orientation ($\iota = 0.7240786$), and polarization ($\psi = 2.228162$) for comparison purposes. We vary the strength of injected signals by adjusting D. We also use a 3-detector advanced LIGO/Virgo network. We use the PSD of the two advanced LIGO detectors under the zero-detuned high power configuration [81] and the parameterized advanced Virgo PSD based on Eq. 6 of [82]. Injection and template waveforms all have a low frequency cutoff at $f_{\rm low} = 30$ Hz and end when the system reaches $f_{\rm high} = f_{\rm ISCO} = c^3/(6^{3/2}\pi GM)$, where $f_{\rm ISCO}$ is the GW frequency of the innermost stable circular orbit (ISCO) of a test particle about a Schwarzschild BH of mass M.

The abrupt termination of waveforms at $f_{\rm ISCO}$ is not ideal for parameter estimation. True gravitational waveforms do not abruptly end at $f_{\rm ISCO}$ or any such artificial frequency cutoff. Recent work [83] has shown that the abrupt termination of frequency-domain

[4]Out to this distance, cosmological redshift is negligible, so we assume the intrinsic frequency of the signal is the same as the observed frequency at the detector. If we were to consider sources out to a greater distance, cosmological redshift would be an additional parameter that is necessary to deduce the true values of the component masses and the equation of state parameters [80].

[5]Note that $\tilde{\Lambda}$ may exceed 3000 for low mass NSs with a stiff EOS. However, this upper bound does not affect the results in this chapter, because the posterior is found to be fully contained within the region of prior support for all cases considered.

waveforms contains additional information that can artificially improve parameter estimation. For instance, since $f_{\rm ISCO}$ depends on the total mass of the system, abruptly ending waveforms at this frequency can reveal more information about a system's mass than is available in practice. We ran tests with template waveforms that were all terminated at an identical fixed frequency cutoff, which had no dependence on the model parameters, to eliminate any information in our waveforms' abrupt frequency cutoff. We found that our results did not change in any noticeable way, which is expected since $f_{\rm ISCO}$ for BNS systems is effectively above our detectors' sensitive frequency band [83]. In addition to the effects of abrupt waveform termination, a given BNS system may have an $f_{\rm ISCO}$ that is greater than the frequency at which the two stars come into contact, which suggests using a lower frequency cutoff for such systems. However, only a few of the systems considered in this work have $f_{\rm contact} < f_{\rm ISCO}$, and we found that this effect only reduces the measurability of tidal parameters for these systems by roughly 5% or less.

4.3.3 Measurability of Tidal Deformability

In order to simulate the parameter estimation of a GW signal, one typically injects a model waveform into a data stream segment consisting of simulated detector noise. The strength of the injected signal relative to the detector noise is characterized by the SNR. The SNR ρ_n of an injection into a single GW detector n is

$$\rho_n = \sqrt{4 \int_0^\infty \frac{|\tilde{h}(f, \vec{\theta})|^2}{S_n(f)} df}, \tag{4.3.8}$$

where $\tilde{h}(f, \vec{\theta})$ is the injected waveform model in the frequency domain. For a collection of detectors, the network SNR $\rho_{\rm net}$ is defined to be

$$\rho_{\rm net} = \sqrt{\sum_n \rho_n^2}. \tag{4.3.9}$$

We report on the optimal measurability of tidal influences in BNS systems assuming a 3-detector LIGO/Virgo network. We follow a similar procedure to the one used in [84], which details the statistical uncertainties in the mass parameters and sky location parameters of BNS systems that are expected to be achieved with advanced detectors.

While one typically injects a signal into synthetic noise, we sometimes choose not to add synthetic noise to our injected signal, which essentially means that we set $n(t) = 0$ in Eq. (4.3.1). However, we still calculate the likelihood and the network SNR by dividing by the detector PSD, which is the variance of the noise. In this way, we incorporate the overall effect of noise without dealing with the statistical fluctuations of individual noise realizations. We refer to this procedure as "injecting into zero-noise" [84].

We inject into zero-noise for two reasons. The first reason is to report measurement uncertainties for typical systems. However, individual results depend on individual realizations of the noise at the time of detection. It is shown in [85] that their "averaged" posterior PDF, or more precisely the prior distribution multiplied by a likelihood that is geometrically averaged over a large number of noise realizations, is recovered by setting the noise to zero. We can therefore estimate the most probable measurement uncertainty of tidal parameters by simply injecting that signal into zero-noise [68; 84–86]. This saves us from having to perform many MCMC simulations with different noise realizations. While this approach only considers the overall effect of noise, we discuss the effect of individual noise realizations in Sec. 4.5.2. The second reason for injecting into zero-noise, which we use in Sec. 4.5.1, is to isolate the effects of systematic error in our analysis. By injecting into zero-noise, we are able to disentangle modeling bias from noise realization effects without having to perform many MCMC simulations, which are computationally expensive [87].

In Fig. 17, we present the 1D and 2D posterior PDFs for $\tilde{\Lambda}$ and $\delta\tilde{\Lambda}$ of a typical BNS system. The true signal was injected with $\rho_{\rm net} = 32.4$, which is considered very large (perhaps a one-per-year event by 2019 [8]). We use tidally corrected TaylorF2 waveforms for the injected waveform as well as for the recovery template waveforms. The injection has the following properties: $m_1 = m_2 = 1.35\ \mathrm{M}_\odot$, $\tilde{\Lambda} = 590.944$, and $\delta\tilde{\Lambda} = 0$, which is consistent with the MPA1 EOS model[6] [1]. We find that the injected value of $\tilde{\Lambda}$ is well

[6]We actually use the parameterized EOS presented in [1] that matches the theoretical MPA1 EOS, as well as many other theoretical EOSs, to a few percent. This approximation is used throughout this work for our convenience. Since the EOS is only used to estimate injected $\tilde{\Lambda}$ values, our results will not be affected by this approximation.

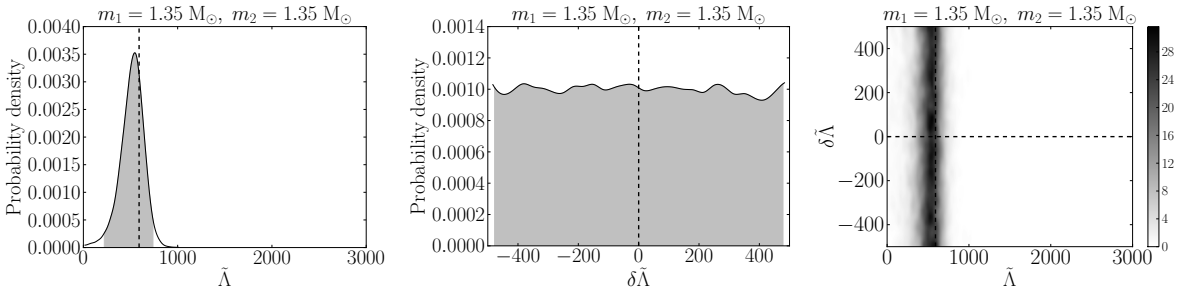

Figure 17 : Marginalized 1D (left and middle) and 2D (right) posterior probability density functions for $\tilde{\Lambda}$ and $\delta\tilde{\Lambda}$ of a 1.35 $\mathrm{M}_\odot$:1.35 $\mathrm{M}_\odot$ BNS system with $\rho_{\mathrm{net}} = 32.4$. The shaded regions in the 1D PDFs enclose 2σ (95%) confidence regions. The color bar in the 2D PDF labels the (unnormalized) probability density. The injected values for $\tilde{\Lambda}$ and $\delta\tilde{\Lambda}$ are consistent with the MPA1 EOS model [1] and are marked with straight dashed lines. These plots are PDFs smoothed with a Gaussian kernel density estimator. For these results, we injected into zero-noise (see Sec. 4.3.3).

recovered.[7] However, advanced detectors are not able to discern $\delta\tilde{\Lambda}$ contributions to the waveform even at a network SNR of 32.4. This is expected because $\delta\tilde{\Lambda}$ only shows up in the 6PN tidal correction, which is $\mathcal{O}(10\%)$ as big as the 5PN term, and additionally contributes little to the 6PN correction since $\delta\tilde{\Lambda}/\tilde{\Lambda} \sim 0$–$0.01$ [73].

In Table 1 we outline the measurement uncertainties for the tidal deformability parameter $\tilde{\Lambda}$ for several equal mass and unequal mass BNS systems. We compute the 1σ and 2σ measurement uncertainty interval by determining the smallest interval in $\tilde{\Lambda}$ that contains 68% and 95% of the total marginalized posterior probability. We then report the lower and upper bound on this confidence interval. The 1σ confidence interval for a 1.35 $\mathrm{M}_\odot$:1.35 $\mathrm{M}_\odot$ BNS system consistent with the MPA1 EOS model is (382.0,636.7) for $\rho_{\mathrm{net}} = 30$. We find that the measurability of the other parameters are not noticeably affected by including tidal parameters in our analysis.

We can also compare our MCMC results to a few FM results. The FM study by Favata [73] uses tidally corrected PN waveforms with a high frequency cutoff of 1000 Hz. Favata finds the 1σ measurement uncertainty of the tidal deformability parameter to be roughly 27% for a 1.40 $\mathrm{M}_\odot$:1.40 $\mathrm{M}_\odot$ BNS system with $\tilde{\Lambda} \approx 600$ at an SNR of 30. Damour, Nagar, and Villain [65] use tidally corrected EOB waveforms that end at contact. In their

[7]The peak of the 1D PDF for $\tilde{\Lambda}$ is consistently found to be displaced from the injected value for equal mass and near equal mass systems. This is a result of marginalizing over the other ten parameters [84], in particular the mass ratio q, whose prior distribution caps off at $q = m_2/m_1 = 1$.

Table 1 : The 1σ (68%) and 2σ (95%) confidence intervals (min,max) for $\tilde{\Lambda}$. The BNS systems considered are labeled by their injected masses (in units of solar mass) and tidal deformability $\tilde{\Lambda}$. Both equal mass and unequal mass systems ranging from $m_{\rm min} = 1.20$ $M_\odot$ to $m_{\rm max} = 2.10$ $M_\odot$ are considered. The injected values for $\tilde{\Lambda}$ are consistent with the MPA1 EOS model [1]. We report confidence intervals for systems with a $\rho_{\rm net}$ of both 20 and 30. For these results, we injected into zero-noise (see Section 4.3.3).

			$\rho_{\rm net} = 20$		$\rho_{\rm net} = 30$	
m_1	m_2	$\tilde{\Lambda}$	1σ	2σ	1σ	2σ
1.20	1.20	1135.630	(553.8 , 1258.1)	(134.6 , 1700.1)	(838.7 , 1193.8)	(516.6 , 1359.4)
1.35	1.35	590.944	(251.3 , 690.2)	(60.7 , 963.0)	(382.0 , 636.7)	(182.3 , 750.8)
1.50	1.50	318.786	(113.2 , 398.9)	(22.9 , 576.8)	(162.1 , 357.4)	(63.9 , 447.7)
1.65	1.65	175.963	(54.5 , 250.2)	(9.6 , 377.2)	(63.5 , 213.9)	(14.0 , 290.8)
1.80	1.80	98.191	(29.2 , 176.8)	(4.9 , 274.9)	(28.9 , 136.1)	(5.0 , 196.8)
1.95	1.95	54.670	(20.1 , 132.5)	(3.5 , 214.4)	(16.6 , 96.1)	(2.6 , 148.2)
2.10	2.10	29.844	(14.8 , 104.8)	(2.1 , 174.4)	(11.7 , 74.0)	(1.9 , 118.6)
1.35	1.20	820.610	(433.7 , 1017.6)	(102.7 , 1381.7)	(612.9 , 941.3)	(340.7 , 1094.6)
1.35	1.50	435.585	(200.0 , 574.9)	(44.4 , 814.5)	(282.5 , 518.0)	(125.5 , 626.1)
1.35	1.65	328.177	(196.1 , 570.5)	(45.5 , 834.6)	(221.3 , 495.9)	(85.5 , 619.1)
1.35	1.80	252.398	(155.1 , 593.1)	(33.0 , 907.0)	(155.9 , 433.5)	(45.5 , 598.6)
1.35	1.95	197.899	(119.0 , 546.9)	(21.5 , 922.6)	(107.3 , 348.2)	(24.7 , 489.1)
1.35	2.10	157.974	(90.7 , 445.4)	(15.8 , 819.9)	(79.3 , 296.8)	(16.2 , 424.9)

FM study, they find a slightly better measurement uncertainty of roughly 21% for a 1.40 $M_\odot$:1.40 $M_\odot$ BNS system with $\tilde{\Lambda} \approx 600$ at an SNR of 30.[8] This improvement is likely due to the extra high frequency information included in the EOB waveforms. Read *et al.* [63] use NR waveforms in their FM study, though they rely on a somewhat crude finite difference approximation. For a 1.35 $M_\odot$:1.35 $M_\odot$ BNS system with $\tilde{\Lambda} \approx 600$ at an SNR of 30, they find a measurement uncertainty of roughly 16% with full hybrid waveforms, though they do not consider correlations with other parameters.[9] Again, the

[8]Since [65] does not include the measurement uncertainty of a BNS system with $\tilde{\Lambda} \approx 600$, this measurement uncertainty was estimated via interpolation.

[9]The finite difference approximation is between the EOS H and HB: $\sigma_{\tilde{\Lambda}} = (\tilde{\Lambda}_{\rm H} - \tilde{\Lambda}_{\rm HB})/||h_{\rm H} - h_{\rm HB}|| = 85$, which results in a measurement uncertainty of $\sigma_{\tilde{\Lambda}}/\tilde{\Lambda}_{\rm H} = 0.16$ when scaled to an SNR of 30.

slight increase in measurability is likely due to the additional high frequency information included in their waveforms. In our MCMC study, we find the measurement uncertainty of the tidal deformability parameter to be roughly 21% for a 1.35 $M_\odot$:1.35 $M_\odot$ BNS system with $\tilde{\Lambda} \approx 600$ at an SNR of 30 in a single advanced LIGO detector. This is in general agreement with existing FM calculations.

4.4 Constraining NS EOS

The NS EOS describes the structure of all cold NSs in equilibrium by relating NS state variables, such as pressure and density. Simultaneous NS mass-radius measurements, or equivalently mass-λ measurements, can highly constrain the NS EOS [88–90]. While many accurate NS mass measurements have been made, corresponding radius measurements are still needed [91].

While $\Lambda_1 \sim (R_1/m_1)^5$ and $\Lambda_2 \sim (R_2/m_2)^5$ are poorly measured by advanced GW detectors due to their strong correlation, the tidal deformability parameter $\tilde{\Lambda}$, which is a linear combination of (Λ_1, Λ_2), is better measured. Ground-based interferometers are most adept at measuring a system's chirp mass $\mathcal{M}_\mathrm{c}$. In the same way that a binary's chirp mass is a mass-like parameter that contains information about the mass of both components, the fifth root of the tidal deformability parameter $\tilde{\Lambda}^{1/5}$ can be thought of as a dimensionless radius-like parameter that contains information about the radius of both components. While GW detectors may not be able to simultaneously constrain the mass and radius of individual NS's, we show that they can simultaneously constrain the mass-like and radius-like parameters describing the binary system as a whole. To further this analogy, we choose to define a conveniently scaled dimensionful radius-like parameter $\mathcal{R}_\mathrm{c} = 2G\mathcal{M}_\mathrm{c}\tilde{\Lambda}^{1/5}/c^2$, which we call the binary's *chirp radius*. Therefore, making a $\mathcal{M}_\mathrm{c}$–$\mathcal{R}_\mathrm{c}$ measurement of a CBC system is analogous to making a mass–radius measurement of a single NS star. Note that the component masses and radii are entangled in the former case and are only determined in combination. The question then becomes: "Does measuring the chirp mass and the chirp radius as opposed to the individual mass and individual radius contain enough information to constrain the NS EOS?"

In Fig. 18, we take a mass-radius plot with multiple theoretical EOS curves [1] (upper

left) and transform it into a $\mathcal{M}_c$–$\mathcal{R}_c$ plot with the same EOS curves, now smeared out due to the extra degrees of freedom from not specifying individual masses and radii (upper right). The three horizontal, black lines are the 1σ confidence regions of three recovered injections. Because chirp mass is so well measured, these confidence regions appear to be lines due to the aspect ratio of this plot. The three bottom plots in Fig. 18 are zoomed-in plots of each recovered injection. From left to right, the important parameters for each injection are: $m_1 = m_2 = 1.50$ $M_\odot$ and $\tilde{\Lambda} = \Lambda_1 = \Lambda_2 = 318.786$, $m_1 = m_2 = 1.35$ $M_\odot$ and $\tilde{\Lambda} = \Lambda_1 = \Lambda_2 = 590.944$, and $m_1 = m_2 = 1.20$ $M_\odot$ and $\tilde{\Lambda} = \Lambda_1 = \Lambda_2 = 1135.63$. The injections all correspond to the EOS MPA1 [1] and have $\rho_{\rm net} = 30$. Fig. 18 demonstrates that simultaneous $\mathcal{M}_c$–$\mathcal{R}_c$ measurements can indeed constrain the NS EOS. However, because certain regions of parameter space can be described by overlapping EOS curves, BNS observations with varying values for chirp mass will likely need to be observed before tight constraints on the NS EOS can be made with this approach.

This inversion of $\mathcal{M}_c$–$\mathcal{R}_c$ measurements to EOS constraints is similar to the inverse stellar structure problem described in [88–90]. Other methods for constraining the NS EOS with GW detectors are discussed in Sec. 4.6.

4.5 Sources of Error

Sources of error in estimating the parameters of a CBC system given its gravitational signal can be categorized as statistical and/or systematic. Statistical error is due to the presence of random detector noise. In Sec. 4.3.3, we focused on the overall effect of detector noise. In this section, our focus is on the effect of individual noise realizations. The kind of systematic error that we are studying arises because our template waveforms only approximate true signals. Statistical error is SNR-dependent, since it depends on the relative strength of the signal to the detector noise, while systematic error is SNR-independent. In this section, we present the effects of both systematic error and individual noise realizations on the ability of advanced ground-based interferometers to measure tidal deformability.

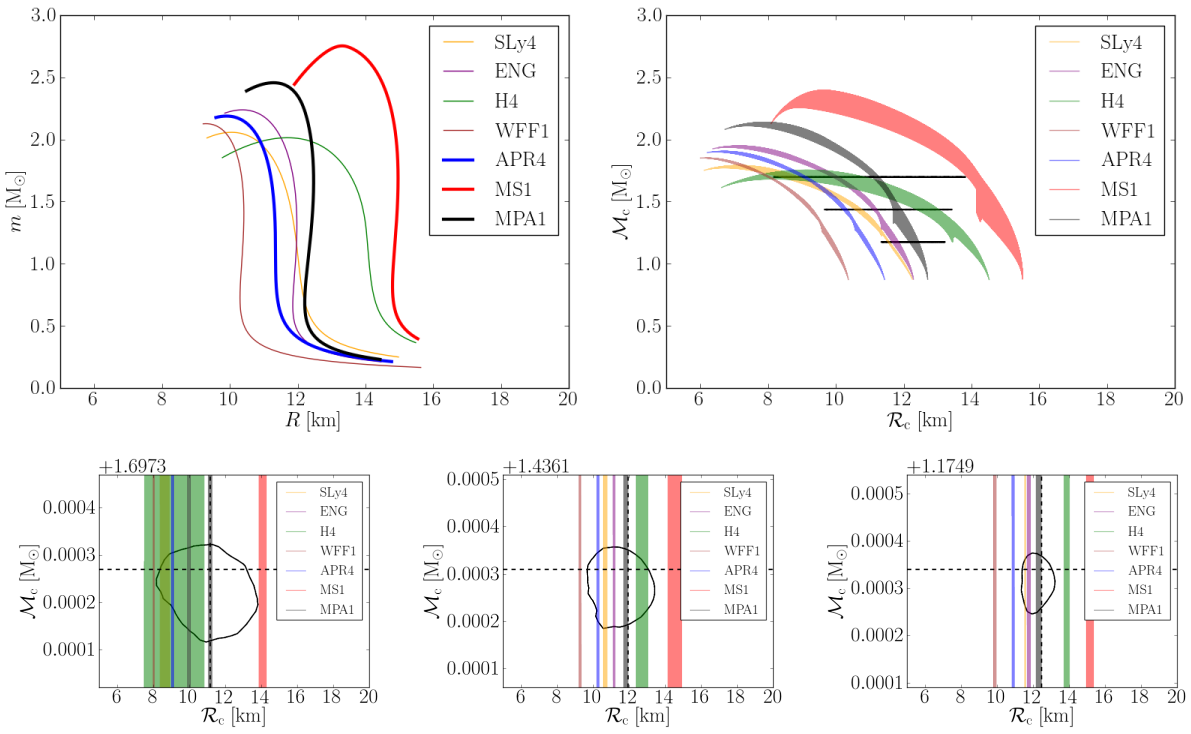

Figure 18 : NS mass-radius plot for a sample of NS EOS models found in the literature [1] (top left). The $\mathcal{M}_c$–$\mathcal{R}_c$ plot (top right), where $\mathcal{R}_c$ is defined in Sec. 4.4, depicts the same EOSs as the mass-radius plot now smeared out due to the extra degrees of freedom from not specifying individual masses and radii. We consider NSs with masses that range from 1 M$_\odot$ to the maximum allowed mass for each EOS. The three horizontal, black lines are the 1σ (68%) confidence regions of three recovered injections. The three bottom plots are zoomed-in to show these recovered injections more clearly. The injected values for $\mathcal{M}_c$ and $\mathcal{R}_c$ are consistent with the MPA1 EOS model and are marked with straight, dashed lines. For these results, we injected into zero-noise (see Sec. 4.3.3).

4.5.1 Systematic Error

The PN approximation to the energy and luminosity of a CBC system is an expansion of the equations of motion about small characteristic velocities, or small frequencies ($v \sim f_{\rm gw}^{1/3}$). Currently, the point-particle corrections to the CBC energy and luminosity are known to 3.5PN order [10]. While PN waveforms match a true GW signal at small frequencies, they are unreliable at high frequencies. Since tidal influences become significant at high frequencies, it is expected that the systematic error from having unreliable waveforms at high frequencies will bias the recovery of tidal parameters. The question is: "By how much?"

We expect that the deviation of PN waveform families away from the true CBC waveform will be comparable to the amount that they deviate away from each other.

All of the PN waveform families are accurate to the same PN order but differ from one another at higher orders. We use the fact that we cannot say which PN family is more accurate as a simple way to parameterize our ignorance of unknown higher order PN terms. We test systematic bias by injecting one PN waveform family and recovering with another. Because all PN waveform families are considered viable, this gives at least a lower bound on the systematic error due to modeling bias. In this way, we can get an order of magnitude estimate of the systematic bias that results from using waveforms that are unreliable at high frequencies to estimate tidal parameters whose effects arise at high frequencies.

In Fig. 19, we present example 1D posterior PDFs for $\tilde{\Lambda}$. We inject signals from each of the five PN waveform families derived in Appendix 4.A but only recover with TaylorF2 templates. Since injected waveforms are only generated once while template waveforms are generated millions of times during an MCMC run, we only use TaylorF2 templates, because they are generated much faster than the other PN waveform families. The injected component masses are labeled in each figure's title, while the injected value of $\tilde{\Lambda}$, which is consistent with the EOS labeled in the legend, is marked by a dashed, vertical line. Each injection has a network SNR of 32.4 and was injected into zero-noise in order to isolate systematic error from statistical error. (Remember that the effects of noise are not completely ignored by injecting into zero-noise. The PSD is still used to calculate likelihood and network SNR.) While we only present three mass combinations and one EOS model in Fig. 19, we also find similar results when considering several other equal and unequal mass combinations and EOS models.

We find that systematic error can be significant in each of the mass combinations and EOSs considered. In particular, the TaylorT4 waveform family has been found to be remarkably similar to equal mass numerical relativity (NR) waveforms [92]. Therefore, for a typical $m_1 = m_2 = 1.35$ $M_\odot$ BNS system with a moderate EOS, say MPA1, systematic error will likely bias the maximum likelihood recovery of $\tilde{\Lambda}$ by $(\tilde{\Lambda}_{\rm inj} - \tilde{\Lambda}_{\rm rec})/\tilde{\Lambda}_{\rm inj}$ ~50%.

It is also interesting to note that the TaylorT3 injected waveforms are all recovered with little to no tidal contribution with TaylorF2 templates. Additionally, the TaylorT3 injected waveforms were recovered with a chirp mass bias of roughly twice its standard

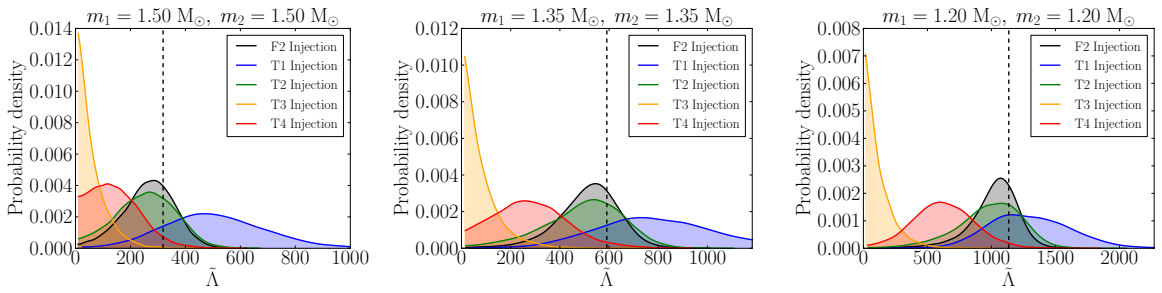

Figure 19 : Marginalized 1D posterior probability density functions for $\tilde{\Lambda}$ of three BNS systems (labelled by the masses in the title) each with $\rho_{\rm net} = 32.4$. The injected $\tilde{\Lambda}$ values are consistent with the MPA1 EOS model [1] and are marked with straight, dashed lines. These plots are PDFs smoothed with a Gaussian kernel density estimator. To generate a single plot, we inject BNS signals modeled by each of the five PN waveform families derived in Appendix 4.A. Though the waveform family for each signal is different, the injected waveform parameters are identical. The five PDFs, which are labelled by the injected waveform family, are all recovered using TaylorF2 waveform templates. The deviation of each peak away from the injected value is due to the systematic error in the PN waveform approximants. For these results, we injected into zero-noise (see Sec. 4.3.3).

deviation, whereas none of the other injected waveforms were recovered with noticeable bias in chirp mass. It was previously seen in [10] that the TaylorT3 approximant agrees poorly with other PN approximants due to its peculiar termination conditions, and we suspect this also explains the biases seen here.

4.5.2 Noise Realizations

Statistical error is due to random fluctuations in detector noise. In Sec. 4.3.3, all signals were injected into zero-noise, which gives the posterior averaged over noise realizations [85]. However, to get an understanding of how much a particular instance of noise can affect parameter recovery, we inject the same signal into ten different synthetic noise realizations (Fig. 20). Here, both the injected waveform model and the recovery waveform model is TaylorF2, and each injection has $\rho_{\rm net} = 32.4$.

We find that the measurability of $\tilde{\Lambda}$ can vary dramatically from one instance of noise to the next. A few out of the ten PDFs plotted in Fig. 20 have significantly broadened peaks, and some even inherit strange multimodal behavior. Therefore, even though the true parameter value still lies within the 90% confidence interval 90% of the time (as expected [67]), statistical error occasionally acts to significantly reduce the measurability of $\tilde{\Lambda}$. Unfortunately some BNS detections may provide uninformative tidal deformability

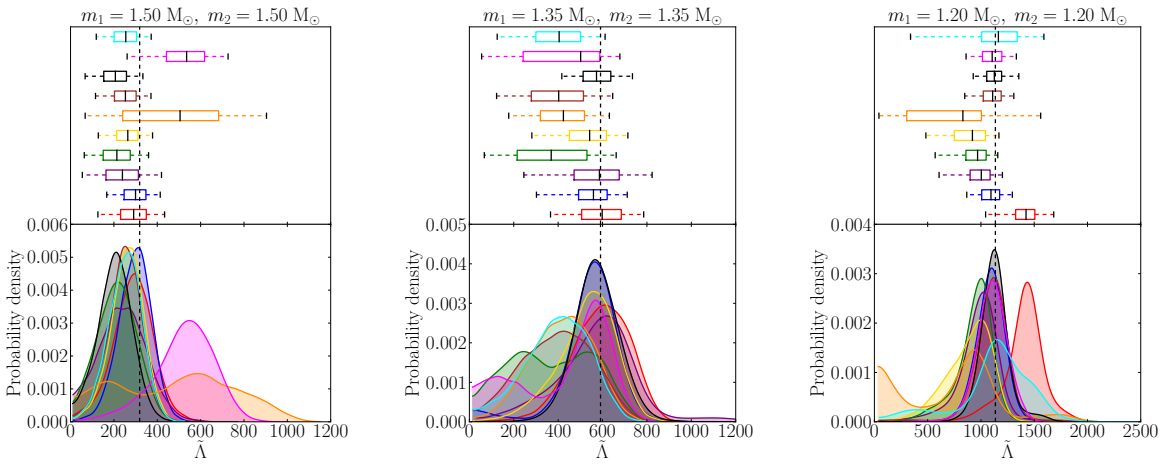

Figure 20 : Marginalized 1D posterior probability density functions for $\tilde{\Lambda}$ of three BNS systems (labelled by the masses in the title) each with $\rho_{\rm net} = 32.4$ (bottom). The injected $\tilde{\Lambda}$ values are consistent with the MPA1 EOS model [1] and are marked with straight, dashed lines. These plots are PDFs smoothed with a Gaussian kernel density estimator. To generate a single plot, we inject the same BNS signal into ten different noise realizations. The deviation of each peak away from the injected value is due to the statistical error from the presence of random detector noise. Each PDF has an associated box-and-whisker representation (top), where the edges of each box mark the first and third quartile, the band inside each box is the median, and the end of the whiskers span the 90% confidence interval.

estimates due to random detector noise. Multiple detections might need to be combined to overcome the effects of noise, which was successfully shown in [71].

4.6 Conclusion/Discussion

In Sec. 4.3.3, we have shown with full Bayesian simulations that tidal deformability in BNS systems is measurable with the advanced LIGO/Virgo network (see Table 1). This is in general agreement with FM studies [63; 65; 73] and compliments the Bayesian results shown in [71]. For a canonical 1.35 $\mathrm{M}_\odot$:1.35 $\mathrm{M}_\odot$ BNS system with the moderate EOS MPA1 recovered using the advanced LIGO/Virgo network, we find that the 1σ measurement uncertainty of $\tilde{\Lambda}$ (or the radius-like $\tilde{\Lambda}^{1/5}$) will likely be $\sim$40% ($\sim$8%) for a source with $\rho_{\rm net} = 20$ and $\sim$20% ($\sim$4%) for a source with $\rho_{\rm net} = 30$.

We showed in Sec. 4.4 how simultaneous measurements of $\tilde{\Lambda}$ and chirp mass can be used to constrain the NS EOS. Other studies in constraining the NS EOS with future GW observations include work by Del Pozzo *et al.* [71], in which Bayesian simulations are used to incorporate information from tens of detections to discriminate between stiff, moderate, and soft EOSs. While Del Pozzo *et al.* showed that tens of BNS sources can

constrain λ for a 1.4 $M_\odot$ NS, which can then be used to constrain the NS EOS, it might even be possible to constrain the full form of the NS EOS over all masses.

In the work presented here, we have examined the ability of GW detectors to measure the tidal parameters $\tilde{\Lambda}$ and $\delta\tilde{\Lambda}$. The main quantity of interest, however, is the universal EOS that is common to all NSs. One method to measure the EOS is to construct a parameterized EOS (e.g. [1; 93; 94]), then replace the tidal parameters in the waveform with EOS parameters. This method allows one to use physical and astrophysical information to place tighter constraints on the priors for the EOS parameters in contrast to the less physically motivated priors on $\tilde{\Lambda}$ and $\delta\tilde{\Lambda}$. Additionally, this allows for combining information from several BNS sources to more tightly constrain EOS parameters. This approach can be found in Ref. [95] and is the topic of Ch. 5.

Both systematic error and individual noise realizations have been shown to significantly affect the measurement of tidal deformability. Individual instances of detector noise can severely broaden the peaks of the marginalized $\tilde{\Lambda}$ posteriors, but can be overcome by combining information from multiple sources, which averages out the effects of noise. This would require many ($\sim$20) BNS detections [71], instead of just a few loud signals. Both optimistic and realistic estimates for the BNS detection rate predict that it will take less than a year after reaching design sensitivity ($\sim$2019) to constrain the NS EOS with GW signals. However, according to pessimistic estimates, this may take considerably longer [53]. Systematic error, which can significantly bias the recovered parameters, is overcome by improving current waveforms. Higher order point-particle terms would be required in order to trust PN waveform families at frequencies sufficiently high to recover tidal deformability. However hybrid waveforms, which are PN waveforms at low frequencies stitched to NR waveforms at high frequency, or phenomenological waveforms, which are waveforms fitted to NR, will likely be required to reliably capture high frequency effects, such as tidal deformability [61; 63; 64; 96]. We hope that these results motivate the importance of prioritizing waveform development that incorporates NS matter effects.

Appendix 4.A Tidally corrected PN waveform derivations

We now adopt units where $G = c = 1$. The equations that describe the CBC orbital phase evolution are the following:

$$\frac{d\phi}{dt} = \frac{v^3}{M} \tag{4.A.1}$$

$$\frac{dv}{dt} = \frac{dv}{dE}\frac{dE}{dt} = \frac{-L}{E'}, \tag{4.A.2}$$

where ϕ is the binary's orbital phase, t is time, the prime represents a derivative with respect to v, and the requirement for energy balance is $dE/dt = -L$. Integrating Eqs. (4.A.1) and (4.A.2) give the alternate form:

$$t(v) = t_{\rm ref} + \int_v^{v_{\rm ref}} \frac{E'(u)}{L(u)} du \tag{4.A.3}$$

$$\phi(v) = \phi_{\rm ref} + \int_v^{v_{\rm ref}} \frac{u^3}{M}\frac{E'(u)}{L(u)} du, \tag{4.A.4}$$

where $t_{\rm ref} = t(v_{\rm ref})$, $\phi_{\rm ref} = \phi(v_{\rm ref})$, and $v_{\rm ref}$ is an arbitrary reference velocity, following [10]. Solutions for $\phi(t)$ and $v(t)$ fully determine a non-spinning CBC waveform with polarizations that go like

$$h_+(t) \propto v^2 \cos 2\phi$$

$$h_\times(t) \propto v^2 \sin 2\phi.$$

Because there are several ways to solve for the orbital phase starting with the same energy and luminosity inputs, there are several different PN waveform families. These PN families are equivalent up to unknown truncation terms at the next PN order. We briefly outline each waveform family below and point out how tidal corrections are incorporated in their derivation. See [10] for the point-particle terms for each waveform family and details regarding initial conditions.

4.A.1 TaylorT1

The TaylorT1 approximant is achieved by numerically solving Eqs. (4.A.1) and (4.A.2) for $\phi(t)$ and $v(t)$. Tidal corrections enter through the energy derivative E' and the luminosity

L:

$$\begin{aligned} E(v) &= E_{\rm pp} + \delta E_{\rm tidal} \\ E'(v) &= E'_{\rm pp} + \delta E'_{\rm tidal} \\ L(v) &= L_{\rm pp} + \delta L_{\rm tidal}, \end{aligned}$$

where $\delta E_{\rm tidal}$ and $\delta L_{\rm tidal}$ come from Eqs. (4.2.2) and (4.2.3) respectively.

4.A.2 TaylorT2

The TaylorT2 approximant is achieved by solving Eqs. (4.A.3) and (4.A.4). First, the ratio E'/L is expanded about $v = 0$ to consistent PN order, then the result is analytically integrated to find $t(v)$ and $\phi(v)$. Tidal corrections enter through the energy derivative E' and the luminosity L and appear at 5PN and 6PN order in $t(v)$ and $\phi(v)$:

$$\begin{aligned} \delta\phi_{\rm tidal}(v) &= -\frac{1}{32\eta x^{5/2}}\left[\left(\frac{72}{\chi_1} - 66\right)\frac{\lambda_1}{M^5}x^5 \right. \\ &\quad \left. + \left(\frac{15895}{56\chi_1} - \frac{4595}{56} - \frac{5715}{28}\chi_1 + \frac{325}{14}\chi_1^2\right)\frac{\lambda_1}{M^5}x^6 + \ (1 \longleftrightarrow 2)\right] \\ \delta t_{\rm tidal}(v) &= -\frac{5M}{256\eta x^4}\left[\left(\frac{288}{\chi_1} - 264\right)\frac{\lambda_1}{M^5}x^5 \right. \\ &\quad \left. + \left(\frac{3179}{4\chi_1} - \frac{919}{4} - \frac{1143}{2}\chi_1 + 65\chi_1^2\right)\frac{\lambda_1}{M^5}x^6 + (1 \longleftrightarrow 2)\right]. \end{aligned}$$

Here, $x = v^2 = (\pi M f_{\rm gw})^{2/3}$ is the PN expansion parameter. The tidal corrections add linearly to the point-particle terms:

$$\begin{aligned} \phi(v) &= \phi_{\rm pp}(v) + \delta\phi_{\rm tidal}(v) \\ t(v) &= t_{\rm pp}(v) + \delta t_{\rm tidal}(v). \end{aligned}$$

These parametric equations are then solved numerically to obtain $\phi(t)$ and $v(t)$.

4.A.3 TaylorT3

The TaylorT3 approximant starts by following the TaylorT2 approach. After $t(v)$ and $\phi(v)$ are found, the following reparameterization is used:

$$\theta(t) = \left[\frac{t_{\rm ref} - t(v)}{5M}\eta\right]^{-1/8}.$$

Next, $v(\theta)$ is found to consistent PN order via reversion of the power series. The characteristic velocity $v(\theta)$ can then be used to find the 5PN and 6PN tidal corrections to the phase $\phi(\theta) = \phi(v(\theta))$ as well as the 5PN and 6PN tidal corrections to the GW frequency $f_{\rm gw} = v^3/(\pi M)$:

$$\begin{aligned}
\delta\phi_{\rm tidal}(\theta) &= -\frac{1}{\eta\theta^5}\left[\left(\frac{9}{128\chi_1}-\frac{33}{512}\right)\frac{\lambda_1}{M^5}\theta^{10}+\right.\\
&\left.\left(\frac{23325}{229376\chi_1}-\frac{12995}{1376256}-\frac{7285}{57344}\chi_1+\frac{4885}{114688}\chi_1^2\right)\frac{\lambda_1}{M^5}\theta^{12}+(1\longleftrightarrow 2)\right]\\
\delta f_{\rm gw,tidal}(\theta) &= \frac{\theta^3}{8\pi M}\left[\left(\frac{27}{256\chi_1}-\frac{99}{1024}\right)\frac{\lambda_1}{M^5}\theta^{10}+\right.\\
&\left.\left(\frac{18453}{131072\chi_1}+\frac{79}{65536}-\frac{14055}{65536}\chi_1+\frac{171}{2048}\chi_1^2\right)\frac{\lambda_1}{M^5}\theta^{12}+(1\longleftrightarrow 2)\right].
\end{aligned}$$

The tidal corrections add linearly to the point-particle terms:

$$\begin{aligned}
\phi(\theta) &= \phi_{\rm pp}(\theta)+\delta\phi_{\rm tidal}(\theta)\\
f_{\rm gw}(\theta) &= f_{\rm gw,pp}(\theta)+\delta f_{\rm gw,tidal}(\theta).
\end{aligned}$$

These equations are essentially the equations for $\phi(t) = \phi(\theta(t))$ and $v(t) = [\pi M f_{\rm gw}(\theta(t))]^{1/3}$.

4.A.4 TaylorT4

The TaylorT4 approximant is achieved by numerically solving Eqs. (4.A.1) and (4.A.2) for $\phi(t)$ and $v(t)$ after first expanding the ratio E'/L about $v = 0$ to consistent PN order. The 5PN and 6PN tidal corrections are:

$$\begin{aligned}
\delta\dot{v}_{\rm tidal} &= \frac{32}{5}\frac{\eta}{M}x^{9/2}\left[\left(\frac{72}{\chi_1}-66\right)\frac{\lambda_1}{M^5}x^5\right.\\
&\left.+\left(\frac{4421}{56\chi_1}-\frac{12263}{56}+\frac{1893}{4}\chi_1-\frac{661}{2}\chi_1^2\right)\frac{\lambda_1}{M^5}x^6+(1\longleftrightarrow 2)\right],
\end{aligned}$$

where the dot represents a derivative with respect to t. The tidal corrections add linearly to the point-particle terms:

$$\dot{v}(v) = \dot{v}_{\rm pp}(v)+\delta\dot{v}_{\rm tidal}(v).$$

4.A.5 TaylorF2

The CBC gravitational waveform can also be derived in the frequency domain using the stationary phase approximation. The waveform takes the form

$$\tilde{h}(f_{\rm gw}) = A(f_{\rm gw}) \exp\left[i\psi(f_{\rm gw})\right],$$

where $\psi(f_{\rm gw}) = 2\pi f_{\rm gw} t(v) - 2\phi(v) - \pi/4$. Substituting Eqs. (4.A.3) and (4.A.4) for t and ϕ into ψ yields:

$$\psi(f_{\rm gw}) = 2\pi f_{\rm gw} t_{\rm ref} - 2\phi_{\rm ref} - \frac{\pi}{4} + 2\int_{v}^{v_{\rm ref}} \frac{v^3 - u^3}{M} \frac{E'(u)}{L(u)} du. \tag{4.A.5}$$

The tidal corrections are found by expanding the ratio E'/L about $v = 0$ to consistent PN order and integrating the expression in Eq. (4.A.5). By choosing to neglect amplitude corrections, the waveform becomes:

$$\tilde{h}(f) = \mathcal{A} f_{\rm gw}^{-7/6} \exp\left[i\psi(f_{\rm gw})\right],$$

where $\mathcal{A} \propto \mathcal{M}_{\rm c}^{5/6}/D$. The chirp mass $\mathcal{M}_{\rm c} = \eta^{3/5} M$, and D is the distance between the GW detector and the binary. The 5PN and 6PN tidal corrections are:

$$\begin{aligned} \delta\psi_{\rm tidal} \;=\; & \frac{3}{128\eta x^{5/2}} \left[-\left(\frac{288}{\chi_1} - 264\right) \frac{\lambda_1}{M^5} x^5 \right. \\ & \left. -\left(\frac{15895}{28\chi_1} - \frac{4595}{28} - \frac{5715}{14}\chi_1 + \frac{325}{7}\chi_1^2\right) \frac{\lambda_1}{M^5} x^6 + (1 \longleftrightarrow 2) \right]. \end{aligned} \tag{4.A.6}$$

The tidal corrections add linearly to the point-particle terms:

$$\psi(v) = \psi_{\rm pp}(v) + \delta\psi_{\rm tidal}(v).$$

The TaylorF2 waveform is one of the most utilized CBC waveforms because its fully analytic frequency-domain form makes it the fastest PN waveform to generate.

Chapter 5

Reconstructing the neutron-star equation of state with gravitational-wave detectors from a realistic population of inspiralling binary neutron stars[1]

5.1 Introduction

In Sec. 4.4, we presented a method for constraining the NS EOS by measuring allowed areas in chirp mass – chirp radius space and excluding candidate EOSs that do not pass inside that area. In this chapter, we introduce an alternate approach that seeks to directly measure the NS EOS. We do this by parameterizing the NS EOS and measuring the parameters of this model. This novel approach allows for straightforward inclusion of physical and observationally motivated priors on the NS EOS, including causality and measurements of massive NSs, and any *a priori* information about the functional form of the EOS in general. Additionally, since all NSs share the same EOS, we can combine information from multiple observations into a single constraint of the NS EOS.

[1]This chapter is based entirely off of the work published in Ref. [95].

We organize this chapter as follows. In Sec. 5.2, we describe the known properties of the NS EOS and outline the parameterization that we use for EOS measurements. Then we discuss our 2-stage Bayesian parameter estimation approach in Sec. 5.3. In Sec. 5.4, we present results from a comprehensive study over a range of observation scenarios using a simulated BNS population and review the effect of error on our analysis. We finish with a discussion on our findings in Sec. 5.5.

5.2 The EOS

As with any equation of state, the NS EOS is a relationship that describes the properties of NS matter under certain physical conditions. More specifically, it is an equation that relates state variables, typically pressure p and energy density ϵ, to one another. Finding this relationship $\mathrm{EOS}(p, \epsilon) = 0$ for NS matter has proven difficult because replicating such densities while remaining in equilibrium ground state has so far been unachievable in laboratories on Earth. Therefore the NS EOS is still highly unconstrained today.

In a standard analysis, an EOS would be used to predict the observable parameters of NSs, which include mass, radius, tidal deformability, etc. Much literature has been devoted to developing candidate theoretical EOS models that describe NS matter. The predictions of observable parameters based on candidate EOSs can then be compared to observations and tested for consistency. For instance, it has been shown that the NS EOS, which is often expressed as $p(\epsilon)$, can be directly calculated from the relationship between NS masses and radii $r(m)$ (as well as mass and tidal deformability $\lambda(m)$) [97]. However, since simultaneous measurements of mass and radius for a given NS have historically been difficult to obtain [98], the most successful attempts at constraining the NS EOS come from precise mass measurements of the heaviest NSs observed. With such measurements, any theoretical candidate EOS model whose $r(m)$ form does not support NSs at such high masses can be eliminated from contention.

However, there is an alternative approach to finding the EOS. Instead of relying on a wide variety of candidate EOSs to contain the true NS EOS and ruling out candidates until only the true EOS is left, one could instead model the NS EOS incorporating what little is actually known about the EOS while also leaving free parameters that represent

our lack of knowledge of the EOS. The parameters of this model can then be constrained observationally to directly measure the NS EOS. The advantage of such an approach is that it does not rely on the production of candidate EOSs; the disadvantage is that any EOS measurement is inherently model-dependent. Therefore, your model should be able to span all possible unconstrained EOS candidates without incorporating too many free parameters.

While the NS EOS is highly unconstrained, there are still a few things that are known about its form:

1. The EOS is known below a certain density ρ_0.
2. The EOS $p(\epsilon)$ must be a monotonically increasing function.
3. The speed of light must be greater than the speed of sound at all densities.
4. The EOS must support all observed NS masses.

We consider these to be *a priori* constraints on the EOS and use this information in our model and our analysis. Therefore, we seek a parameterized model that not only follows these rules but also has enough flexibility to match the true NS EOS, whatever it might be. While the literature provides several adequate EOS representations, for this first analysis, we choose to employ the 4-piece polytropic parameterization of [99] due to its frequent use in gravitational-wave literature.

The 4-piece polytropic parameterization is constructed as follows. Four polytropic segments

$$p(\rho) = K_i \rho^{\Gamma_i}, \tag{5.2.1}$$

are continuously stitched together to form our model. Here p is the pressure, K is a polytropic constant, ρ is the rest-mass density, and Γ is an adiabatic index. Note that since the energy density is a function of the rest-mass density $\epsilon = \epsilon(\rho)$, the EOS $p(\epsilon)$ is equivalently represented as a function of the rest-mass density $p(\rho) = p(\epsilon(\rho))$. The NS core is represented by three polytropes joined together at the two fixed dividing densities $\rho_1 = 10^{14.7}$ g/cm^3 and $\rho_2 = 10^{15}$ g/cm^3. The lower density crust is modeled by a fourth fixed polytrope that is fitted to the Sly EOS [99]. The point at which the lowest

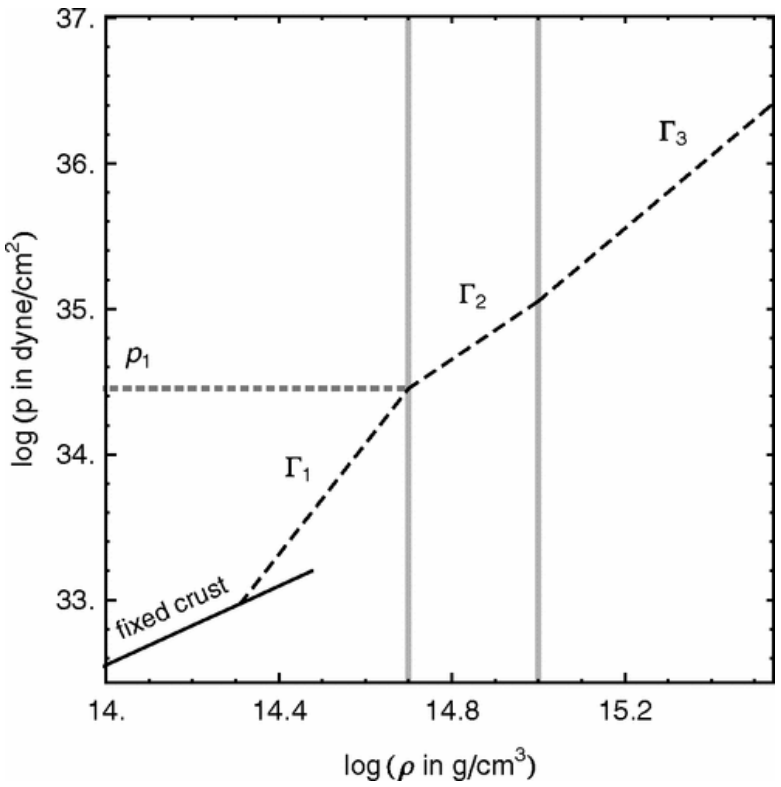

Figure 21 : Depiction of 4-piece polytropic EOS model from Ref. [1] used as our NS EOS model. The leftmost polytrope is fitted to the SLy candidate EOS and represents the fixed crust. The next three polytropes have adiabatic indexes Γ_1, Γ_2, Γ_3, and are stitched together at the densities ρ_1 and ρ_2 represented by vertical gray lines. The pressure p_1 at which the middle two polytropes are joined sets the pressure scaling.

density polytrope describing the core is joined to this fixed crust polytrope is determined by the overall pressure scaling, which is controlled by the pressure at the first joining density $p_1 = p(\rho_1)$. This results in a 4-piece polytropic EOS model with four independent parameters $\vec{\theta}_{\rm EOS} = \{\log(p_1), \Gamma_1, \Gamma_2, \Gamma_3\}$ (Fig. 21). This model has been shown to match a wide range of candidate EOSs to a few percent making it a useful model for EOS measurements. For more details, see [99].

This 4-piece polytropic model is a monotonically increasing function ($dp/d\epsilon \geq 0$) that converges to the same known form below $\rho = \rho_0$. Therefore conditions 1 and 2 are built directly into our EOS model. However, conditions 3 and 4 are not always satisfied with this model. In section 5.3, we outline how these conditions are built into our analysis by including them as *a priori* information used for updating our measured EOS posteriors.

We incorporate EOS effects into the gravitational waveform using this EOS fit.

Since the NS EOS $p(\rho)$ defines the relationship between its mass and its tidal deformability $\lambda(m|\text{EOS})$, by specifying the four parameters of our model, we can determine the tidal deformability parameters λ for a NS given its mass. In this way, EOS effects enter the gravitational waveform through the calculating of the tidal deformability $\lambda = \lambda(m|\log(p_1), \Gamma_1, \Gamma_2, \Gamma_3)$ as described in Sec. 4.2.

5.3 Two-stage MCMC approach

In Ch. 4, we used MCMC simulations to estimate the posterior distribution $p(\vec{\theta}|d, \mathcal{H}, \mathcal{I})$ for several simulated BNS inspiral events whose waveforms were modeled by the parameters $\vec{\theta} = \{\mathcal{M}_\text{c}, q, \tilde{\Lambda}, \delta\tilde{\Lambda}, D, \iota, \alpha, \delta, \psi, \phi_\text{ref}, t_\text{ref}\}$. In doing so, we first had to develop the `LALInferenceMCMC` sampler to take steps in the tidal deformability parameters $\vec{\theta}_\text{tidal} = \{\tilde{\Lambda}, \delta\tilde{\Lambda}\}$. We then marginalized over all extrinsic parameters to find the marginalized posterior distribution $p(\mathcal{M}_\text{c}, q, \tilde{\Lambda}, \delta\tilde{\Lambda}|d, \mathcal{H}, \mathcal{I})$ of the intrinsic parameters.

We now seek to estimate the marginalized posterior distribution $p(\vec{\theta}_\text{EOS}|d_1, \ldots, d_n, \mathcal{H}, \mathcal{I})$ for n BNS events whose waveforms are modeled by the EOS parameters $\vec{\theta}_\text{EOS} = \{\log(p_1), \Gamma_1, \Gamma_2, \Gamma_3\}$ instead of the tidal deformability parameters $\vec{\theta}_\text{tidal} = \{\tilde{\Lambda}, \delta\tilde{\Lambda}\}$. The full set of parameters in this case, including external parameters, is $\vec{\theta}' = \{\mathcal{M}_\text{c}, q, \log(p_1), \Gamma_1, \Gamma_2, \Gamma_3, D, \iota, \alpha, \delta, \psi, \phi_\text{ref}, t_\text{ref}\}$. Developing the `LALInferenceMCMC` sampler to take steps in the EOS parameters $\vec{\theta}_\text{EOS}$ also involves calculating $\lambda = \lambda(m|\vec{\theta}_\text{EOS})$ for each proposed step, which is not a trivial transformation. With the utilities available to my collaborators and I at the time, it was more convenient to use a two-stage MCMC approach to estimate the marginalized posterior distribution when including EOS parameters. Additionally, since all NS matter is governed by the same EOS, the second step of this approach allows us to combine information from multiple inspiral events to put tighter constraints on the EOS parameters, as was demonstrated in [100]. We have since developed the `LALInferenceMCMC` sampler to take steps in the EOS parameters, and the results match those from our two-stage approach.

5.3.1 Derivation

We first derive the two-stage approach, which follows Sec. IV.A in Ref. [95]. Since we seek to measure the NS EOS, our primary goal is to find the marginalized posterior PDF for just the EOS parameters. When considering a single inspiral event, this would normally be calculated by finding the full posterior PDF and integrating out all non-EOS parameters:

$$p(\vec{\theta}_{\rm EOS}|d,\mathcal{H},\mathcal{I}) = \int p(\vec{\theta}'|d,\mathcal{H},\mathcal{I})d\vec{\theta}_{\rm other}, \tag{5.3.1}$$

where $\vec{\theta}' = \{\vec{\theta}_{\rm EOS}, \vec{\theta}_{\rm other}\}$. However, as mentioned above, the calculation of $p(\vec{\theta}'|d,\mathcal{H},\mathcal{I})$ requires us to develop the `LALInferenceMCMC` sampler to take steps in EOS parameters. We wondered if we could somehow use the MCMC from the original parameterization ($\vec{\theta} = \{\mathcal{M}_{\rm c}, q, \tilde{\Lambda}, \delta\tilde{\Lambda}, D, \iota, \alpha, \delta, \psi, \phi_{\rm ref}, t_{\rm ref}\} = \{\vec{\theta}_{\rm tidal}, \vec{\theta}_{\rm other}\}$) to estimate $p(\vec{\theta}_{\rm EOS}|d,\mathcal{H},\mathcal{I})$.

We start by treating the EOS parameters as extra parameters independent of the existing tidal parameters, and we will later use the fact that the EOS parameters and the mass parameters together determine the tidal parameters. The marginalized posterior of this system is

$$p(\vec{\theta}_{\rm EOS}|d,\mathcal{H},\mathcal{I}) = \int p(\vec{\theta}_{\rm EOS},\vec{\theta}|d,\mathcal{H},\mathcal{I})d\vec{\theta}, \tag{5.3.2}$$

When considering n events that are known to have the same EOS parameters, this becomes:

$$\begin{aligned} p(\vec{\theta}_{\rm EOS}|d_1,\ldots,d_n,\mathcal{H},\mathcal{I}) &= \int p(\vec{\theta}_{\rm EOS},\vec{\theta}_1,\ldots,\vec{\theta}_n|d_1,\ldots,d_n,\mathcal{H},\mathcal{I})d\vec{\theta}_1\ldots d\vec{\theta}_n \\ &= \frac{1}{p(d_1,\ldots,d_n,|\mathcal{H},\mathcal{I})}\int p(\vec{\theta}_{\rm EOS},\vec{\theta}_1,\ldots,\vec{\theta}_n|\mathcal{I}) \\ &\times\ p(d_1,\ldots,d_n,|\vec{\theta}_{\rm EOS},\vec{\theta}_1,\ldots,\vec{\theta}_n,\mathcal{H},\mathcal{I})\ d\vec{\theta}_1\ldots d\vec{\theta}_n \end{aligned}$$

where Bayes' theorem was used to get to the second line from the first. The prior $p(\vec{\theta}_{\rm EOS},\vec{\theta}_1,\ldots,\vec{\theta}_n|\mathcal{I})$ can be broken up as follows:

$$\begin{aligned} p(\vec{\theta}_{\rm EOS},\vec{\theta}_1,\ldots,\vec{\theta}_n|\mathcal{I}) &= p(\vec{\theta}_{\rm EOS}|\mathcal{I})\prod_{i=1}^{n} p(\vec{\theta}_i|\vec{\theta}_{\rm EOS},d_i,\mathcal{I}) \\ &= p(\vec{\theta}_{\rm EOS}|\mathcal{I})\prod_{i=1}^{n}\Big[p(m_{1,i},m_{2,i}|\vec{\theta}_{\rm EOS},\mathcal{I}) \\ &\times\ p(\tilde{\Lambda}_i|m_{1,i},m_{2,i},\vec{\theta}_{\rm EOS},\mathcal{I})p(\vec{\theta}_{{\rm ex},i}|\mathcal{I})\Big], \end{aligned}$$

where the first step used the conditional probability chain rule. Here, we take $\vec{\theta}_{\mathrm{ex},i}$ to be the extrinsic parameters of $\vec{\theta}_i$, which are $\{\delta\tilde{\Lambda}_i, D_i, \iota_i, \alpha_i, \delta_i, \psi_i, \phi_{\mathrm{ref},i}, t_{\mathrm{ref},i}\}$, and these do not depend on EOS parameters. Technically, $\delta\tilde{\Lambda}$ is an intrinsic tidal deformability parameter which provides additional EOS information. However, we have shown in Sec. 4.3.3 that it is unmeasurable with aLIGO, so we marginalize it out along with the rest of the extrinsic parameters. Because the likelihood $p(d_1, \ldots, d_n, |\vec{\theta}_{\mathrm{EOS}}, \vec{\theta}_1, \ldots, \vec{\theta}_n, \mathcal{H}, \mathcal{I})$ depends on n different BNS events and only depends on the waveform parameters, not the EOS parameters, it can be written as a product of single-event likelihoods like so

$$p(d_1, \ldots, d_n, |\vec{\theta}_{\mathrm{EOS}}, \vec{\theta}_1, \ldots, \vec{\theta}_n, \mathcal{H}, \mathcal{I}) = \prod_{i=1}^{n} p(d_i|\vec{\theta}_i, \mathcal{H}, \mathcal{I}).$$

The variables of integration $d\vec{\theta}_1 \ldots d\vec{\theta}_n$ can also be split up into their extrinsic and intrinsic parts. By then reorganizing the integral, the marginalized posterior can be written

$$\begin{aligned} p(\vec{\theta}_{\mathrm{EOS}}|d_1, \ldots, d_n, \mathcal{H}, \mathcal{I}) &= \frac{1}{p(d_1 \ldots, d_n|\mathcal{H}, \mathcal{I})} \int p(\vec{\theta}_{\mathrm{EOS}}|\mathcal{I}) \\ &\times \left[\prod_{i=1}^{n} p(m_{1,i}, m_{2,i}|\vec{\theta}_{\mathrm{EOS}}, \mathcal{I}) p(\tilde{\Lambda}_i|m_{1,i}, m_{2,i}, \vec{\theta}_{\mathrm{EOS}}, \mathcal{I})\right. \\ &\times \left.\int p(\vec{\theta}_{\mathrm{ex},i}|\mathcal{I}) p(d_i|\vec{\theta}_i, \mathcal{H}, \mathcal{I}) d\vec{\theta}_{\mathrm{ex},i}\right] d\vec{\theta}_{\mathrm{in},1} \ldots d\vec{\theta}_{\mathrm{in},n} \end{aligned}$$

Here, we take $\vec{\theta}_{\mathrm{in},i}$ to be the intrinsic parameters of $\vec{\theta}_i$, which are $\{\tilde{\Lambda}_i, m_{1,i}, m_{i,2}\}$. We now use the fact that the EOS parameters and the mass parameters together determine the tidal parameters to write the prior in $\tilde{\Lambda}$ as

$$p(\tilde{\Lambda}_i|m_{1,i}, m_{2,i}, \vec{\theta}_{\mathrm{EOS}}, \mathcal{I}) = \delta(\tilde{\Lambda}_i - \tilde{\Lambda}(m_{1,i}, m_{2,i}, \vec{\theta}_{\mathrm{EOS}})).$$

The marginalized posterior is now

$$\begin{aligned} p(\vec{\theta}_{\mathrm{EOS}}|d_1, \ldots, d_n, \mathcal{H}, \mathcal{I}) &= \frac{1}{p(d_1 \ldots, d_n|\mathcal{H}, \mathcal{I})} \int p(\vec{\theta}_{\mathrm{EOS}}|\mathcal{I}) \left[\prod_{i=1}^{n} p(m_{1,i}, m_{2,i}|\vec{\theta}_{\mathrm{EOS}}, \mathcal{I})\right. \\ &\times \left.\left[\int p(\vec{\theta}_{\mathrm{ex},i}|\mathcal{I}) p(d_i|\vec{\theta}_i, \mathcal{H}, \mathcal{I}) d\vec{\theta}_{\mathrm{ex},i}\right]_{\tilde{\Lambda}_i = \tilde{\Lambda}(m_{1,i}, m_{2,i}, \vec{\theta}_{\mathrm{EOS}})}\right] \\ &\times dm_{1,1} dm_{2,1} \ldots dm_{1,n} dm_{2,n}. \end{aligned}$$

By realizing that

$$\mathcal{L}(d_i; \vec{\theta}_{\mathrm{in},i}, \mathcal{H}, \mathcal{I}) = \int p(\vec{\theta}_{\mathrm{ex},i}|\mathcal{I}) p(d_i|\vec{\theta}_i, \mathcal{H}, \mathcal{I}) d\vec{\theta}_{\mathrm{ex},i} \tag{5.3.3}$$

is the quasi-likelihood for the intrinsic parameters, the marginalized posterior for the EOS parameters can be written

$$\begin{aligned} p(\vec{\theta}_{\rm EOS}|d_1,\ldots,d_n,\mathcal{H},\mathcal{I}) &= \frac{1}{p(d_1\ldots,d_n|\mathcal{H},\mathcal{I})}\int p(\vec{\theta}_{\rm EOS}|\mathcal{I}) \\ &\times \prod_{i=1}^{n}\Big[p(m_{1,i},m_{2,i}|\vec{\theta}_{\rm EOS},\mathcal{I}) \\ &\times \mathcal{L}(d_i;\vec{\theta}_{{\rm in},i},\mathcal{H},\mathcal{I})|_{\tilde{\Lambda}_i=\tilde{\Lambda}(m_{1,i},m_{2,i},\vec{\theta}_{\rm EOS})}\Big] \\ &\times dm_{1,1}dm_{2,1}\ldots dm_{1,n}dm_{2,n}. \end{aligned} \tag{5.3.4}$$

Estimating $p(\vec{\theta}_{\rm EOS}|d_1,\ldots,d_n,\mathcal{H},\mathcal{I})$ can now be broken into two stages: 1) solve for the quasi-likelihood in Eq. (5.3.3), which is easily estimated by the marginalized posterior samples for each event using the `LALInferenceMCMC` sampler, and 2) solve 5.3.4, which is done using another MCMC routine.

5.3.2 Implementation

The two-stage approach to calculate Eq. (5.3.4) is implemented in the following way:

1. **Stage 1:** Given $d_1,\ldots,d_n$, run each data stream segment through the `LALInferenceMCMC` parameter estimation pipeline. This takes steps in the parameters $\vec{\theta}_i = \{\mathcal{M}_{{\rm c},i}, q_i, \tilde{\Lambda}_i, \delta\tilde{\Lambda}_i, D_i, \iota_i, \alpha_i, \delta_i, \psi_i, \phi_{{\rm ref},i}, t_{{\rm ref},i}\}$ and calculates the likelihood from Eq. (4.3.4) at each point. The output of the MCMC sampler is just a list of parameter points for each segment d_i. The density of the MCMC samples is an estimation of the underlying posterior distribution $p(\vec{\theta}_i|d_i,\mathcal{H},\mathcal{I})$ and can be used to construct this distribution, if desired.

2. Marginalize each posterior over extrinsic parameters, which by definition is calculated through an integration: $p(\mathcal{M}_{{\rm c},i}, q_i, \tilde{\Lambda}_i|d_i,\mathcal{H},\mathcal{I}) = \int p(\vec{\theta}_i|d_i,\mathcal{H},\mathcal{I})d\vec{\theta}_{{\rm ex},i}$, where we group the unmeasurable $\delta\tilde{\Lambda}_i$ with the extrinsic parameters $\vec{\theta}_{{\rm ex},i}$. However, one of the conveniences of using an MCMC algorithm is that this integration is equivalently (but much more simply) accomplished by storing only the information from the intrinsic parameters for each MCMC sample. Thus, no integration is required to find marginalized MCMC samples which can be used to construct $p(\mathcal{M}_{{\rm c},i}, q_i, \tilde{\Lambda}_i|d_i,\mathcal{H},\mathcal{I})$, if desired.

3. Using $\eta = q/(1+q)^2$, perform a coordinate transformation from $q_i \rightarrow \eta_i$ for each marginalized MCMC sample of the intrinsic parameters.

4. Construct $p(\mathcal{M}_{\mathrm{c},i}, \eta_i, \tilde{\Lambda}_i | d_i, \mathcal{H}, \mathcal{I})$ from the density of the marginalized MCMC samples. This is done using a Gaussian kernel density estimator (KDE) on the intrinsic parameter samples. For our case, the function $p(\mathcal{M}_{\mathrm{c},i}, \eta_i, \tilde{\Lambda}_i | d_i, \mathcal{H}, \mathcal{I})$ is equal to $\mathcal{L}(d_i; \vec{\theta}_{\mathrm{in},i}, \mathcal{H}, \mathcal{I})$ of Eq. (5.3.4) because the intrinsic parameter priors are uniform, which will be discussed shortly.

5. **Stage 2:** Given $p(\mathcal{M}_{\mathrm{c},i}, \eta_i, \tilde{\Lambda}_i | d_i, \mathcal{H}, \mathcal{I})$ for each data stream segment d_i, use another MCMC simulation to estimate the integrand of Eq. (5.3.4). We chose the affine-invarient ensemble sampler `emcee` for our analysis [101]. We set up this MCMC sampler to take steps in $4 + 2n$ parameters: 4 EOS parameters (common to each system) and 2 mass parameters (independent for each system). These parameters are $\{\log(p_1), \Gamma_1, \Gamma_2, \Gamma_3, \mathcal{M}_{\mathrm{c},1}, \eta_1, \ldots, \mathcal{M}_{\mathrm{c},n}, \eta_n\}$. We calculate the joint likelihood of each sample by calculating $\{\tilde{\Lambda}_i, \mathcal{M}_{\mathrm{c},i}, \eta_i\}$ from $\{\log(p_1), \Gamma_1, \Gamma_2, \Gamma_3, \mathcal{M}_{\mathrm{c},i}, \eta_i\}$, finding the value of the quasi-likelihood at that point using the function $\mathcal{L}(d_i; \vec{\theta}_{\mathrm{in},i}, \mathcal{H}, \mathcal{I}) = p(\mathcal{M}_{\mathrm{c},i}, \eta_i, \tilde{\Lambda}_i | d_i, \mathcal{H}, \mathcal{I})$ from Step 4, and taking the product of each quasi-likelihood. The priors used are the mass and EOS priors in the integrand of Eq. (5.3.4).

6. Marginalize over the masses to obtain samples from $p(\vec{\theta}_{\mathrm{EOS}} | d_1, \ldots, d_n, \mathcal{H}, \mathcal{I})$. Again, this is done by simply storing only the information from the EOS parameters for each MCMC sample.

7. Construct $p(\vec{\theta}_{\mathrm{EOS}} | d_1, \ldots, d_n, \mathcal{H}, \mathcal{I})$ from the density of the marginalized MCMC samples. This is done using a Gaussian KDE on the intrinsic parameter samples.

The priors used in the Stage-1 MCMC are those outlined in Sec. 4.3.2. However, when we injected 1 $\mathrm{M}_\odot$ NSs, we reduced the lower limit on the component mass priors to be $0.5\ \mathrm{M}_\odot \leq m_2 \leq m_1 \leq 30\ \mathrm{M}_\odot$ and the upper limit of the measurable tidal deformability parameter to be $0 \leq \tilde{\Lambda} \leq 5000$. This was to ensure that our posterior distributions were not affected by the choice of our prior distributions.

The priors used in the "Stage 2" MCMC are as follows. The prior distribution for the EOS parameters are uniform in $33.5 \leq \log(p_1) \leq 34.5$, where p_1 is in cgs units,

cm^{-1} g s^{-2}, $1.4 \leq \Gamma_1 \leq 5$, $1 \leq \Gamma_2 \leq 5$, and $1 \leq \Gamma_3 \leq 5$. Additional restrictions on the EOS parameters are that the speed of light must be greater than the speed of sound ($\sqrt{dp/d\epsilon} < c$) and that the EOS must support the largest observed NS, which we take to be the pulsar J0348+0432 with a 2σ lower-bound mass of 1.93 $\mathrm{M}_\odot$ (conditions 3 and 4 of Sec. 5.2). Lastly, we also require that $\rho_0 \geq 2.63 \times 10^{12}$ g/cm^3, which restricts small values of Γ_1 for large $\log(p_1)$ (see [99]). We also use uniform prior distributions in $1\ \mathrm{M}_\odot \leq m_2 \leq m_1 \leq 3\ \mathrm{M}_\odot$, unless injecting 1 $\mathrm{M}_\odot$ NSs, in which case we use uniform prior distributions in $0.5\ \mathrm{M}_\odot \leq m_2 \leq m_1 \leq 3\ \mathrm{M}_\odot$. A 3 $\mathrm{M}_\odot$ upper limit in component mass (as opposed to the 30 $\mathrm{M}_\odot$ upper limit of the "Stage 1" MCMC) fully contains the major contributions of each posterior as well as the allowed NS masses for all viable EOSs.

5.4 Measuring the NS EOS

We seek to characterize the ability of the Advanced LIGO–Virgo network to measure the NS EOS from detected BNS events. To do so, we simulate a realistic population of coalescing BNS events.

5.4.1 The baseline simulated BNS population

The key properties of our simulated BNS population are as follows.

- **Number of events:** The number of coalescing BNS events accessible to the Advanced LIGO–Virgo network depends on the BNS inspiral rate per Milky Way Equivalent Galaxy (MWEG), the number density of MWEGs, and the observational time. We choose to use the "realistic" BNS inspiral rate and number density from Ref. [53], which are 100 events / Myr / MWEG and 0.0116 MWEGs / Mpc^3 respectively. We also choose an observational time of one full year of data where all three detectors are taking data simultaneously. These three numbers can be used to determine the number of coalescing BNS systems within a volume of radius r through

$$\mathcal{N}_{\mathrm{BNS}}(r) = \left(100\ \frac{\text{BNS events}}{\text{MWEG Myr}}\right)\left(\frac{1}{10^6}\ \frac{\text{Myr}}{\text{yr}}\right)\left(0.0116\ \frac{\text{MWEG}}{\text{Mpc}^3}\right)\left(\frac{4}{3}\pi r^3\right)(1\ \text{yr})\,. \tag{5.4.1}$$

Since we expect detecting a certain number of BNS events to be a Poisson process, we construct a Poisson distribution with mean $\mathcal{N}_{\rm BNS}(r_{\rm max})$, where $r_{\rm max}$ is chosen to overestimate the reach of the Advanced LIGO–Virgo network. We then draw from this Poisson distribution to determine the number of BNS systems to simulate.

- **System parameter distributions:** We distribute the BNS systems uniformly in volume and orientation. We draw the mass of each NS from a uniform distribution between 1.2 $M_\odot$ and 1.6 $M_\odot$, which is chosen to resemble the Gaussian distribution of Ref. [102]. We assumed that the NSs were non-spinning for this analysis.

- **Detector properties:** The detector sensitivity is characterized by their PSDs. We use the Advanced detector PSDs referenced in Sec. 4.3.2 for this analysis. Of the BNS systems simulated ∼120 had $\rho_{\rm net} \geq 8$ and ∼30 had $\rho_{\rm net} \geq 12$, where $\rho_{\rm net} = 12$ is often taken as a rough estimate of the detection threshold for a GW search. We analyzed the loudest (largest $\rho_{\rm net}$) 20 sources whose $\rho_{\rm net}$, calculated by integrating from $f_{\rm min} = 30$ Hz to $f_{\rm ISCO}$, ranged from 63.7 to 13.6.

- **NS EOS:** We choose to use the 4-piece polytropic fit of MPA1 from Ref. [99] as the true EOS for every BNS event in our simulated population. The MPA1 EOS is considered a moderate EOS, and using its fit instead of its true tabulated form separates systematic error effects from using an inexact EOS model and an inexact waveform model, which is discussed later in this chapter.

We injected signals from this baseline population into zero-noise data to separate the effects of statistical fluctuations in noise from our results and estimate the most probable measurement uncertainty of EOS parameters, as described in Sec. 4.3.3. In Fig. 22, we present the 1σ, 2σ, and 3σ credible regions found when combining information from the loudest 20 events to measure the NS EOS. These figures are made in the following way. First, the independent parameter (either ρ or m) is binned, and each bin is assigned a value for the independent parameter (i.e. the midpoint of the bin). Next, the dependent parameter value (p, R, or λ) at a specific bin for each MCMC sample is calculated from the EOS specified by the marginalized EOS parameters and the value of the independent parameter at that bin. The dependent parameter samples for each independent parameter

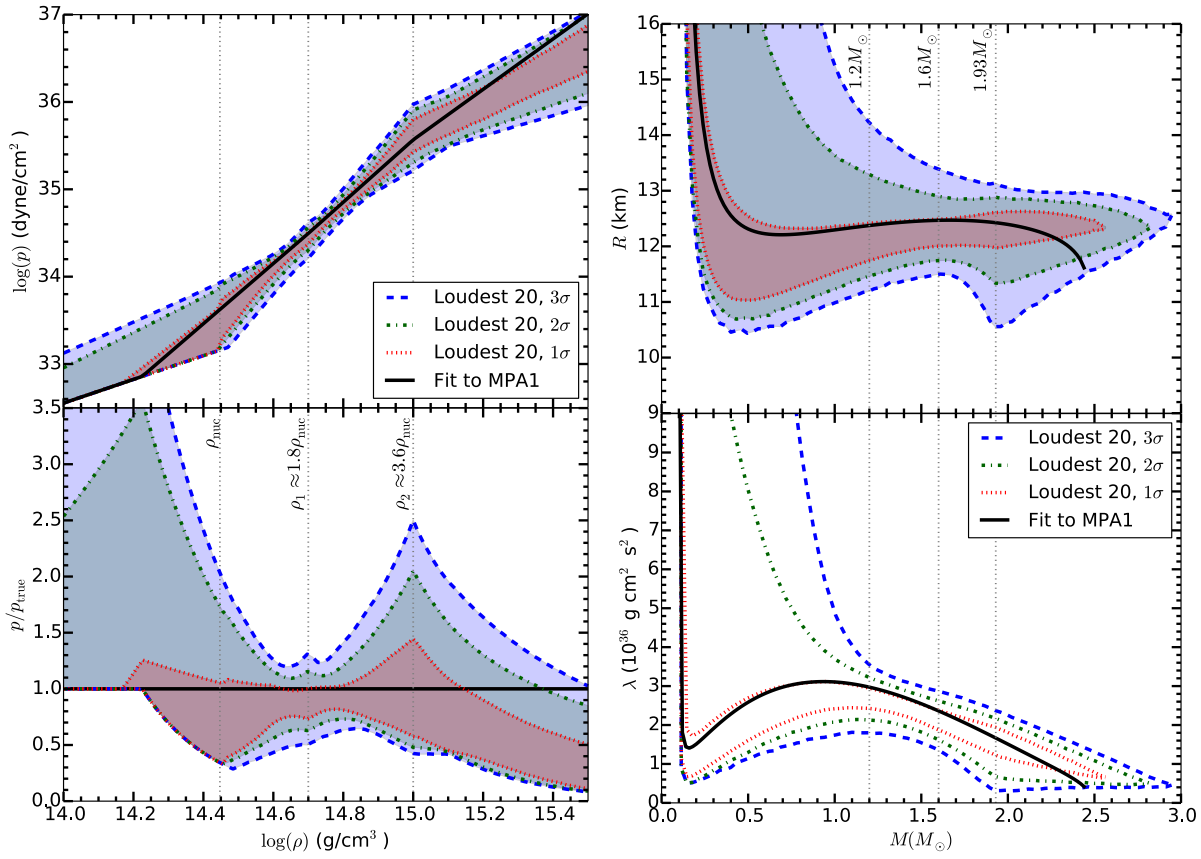

Figure 22 : Measurement uncertainty in the recovered EOS $p(\rho)$, radius $R(m)$, and tidal deformability $\lambda(m)$ for the loudest 20 events of the baseline BNS population. The red, green, and blue shaded regions represent the 1σ, 2σ, and 3σ credible regions respectively. The "true" pressure in the bottom left panel is the pressure of the injected EOS, which in this case is the fit to the MPA1 EOS. In the right panels, the dotted vertical line at 1.93 $M_\odot$ is the mass above which some accepted EOS parameters do not produce a stable NS, and this mass is set by the prior.

bin are histogrammed, and the credible intervals are calculated for each bin. Once this is done for every independent variable bin, the credible intervals in each bin are connected across the full space to become the contours shown. A slight complication arises for the plots binned in component mass. Each proposed EOS has a maximum supported NS mass. When considering mass bins above 1.93 $M_\odot$, not all the EOSs for each MCMC sample formed stable NSs at that mass. Instead, masses above 1.93 $M_\odot$ resulted in black holes for some EOS models, and the radius and tidal deformability distributions became bimodal with delta function peaks at the Schwarzschild radius and $\lambda = 0$. Therefore, the credible intervals in radius and tidal deformability for masses above 1.93 $M_\odot$ represent the fraction of the MCMC samples that produce a NS or a black hole.

Fig. 22 demonstrates the effectiveness of the Advanced LIGO–Virgo network to measure the NS EOS. Combining information from the loudest 20 BNS events in a year of triple-coincident data, radius measurements for NSs between 1–2 $M_\odot$ are achievable with an uncertainty of less than 1 km. Additionally, constraints can be placed on the EOS even for NSs not within this mass range, though these constraints are admittedly not as tight. This would be a great achievement if accomplished.

It is apparent from the $p/p_{\rm true}$ plot in Fig. 22, however, that a large portion of the credible interval in certain density regions is a result of the EOS parameterization. Firstly, there is relatively larger uncertainty in the pressure around the fixed transition densities ρ_1 and ρ_2. A model whose transition densities are free parameters, such as the one presented in [103], would not experience such features. Secondly, the credible interval seem to underestimate $p_{\rm true}$ at large densities. This is where we are running up against the causality limit. The maximum speed of sound for the MPA1 EOS is $v_{\rm s,max} = 0.994$. The 4-piece fit to this EOS overestimates this quantity by roughly 5%. However, since $v_{\rm s,max}$ must be less than c and the corresponding 4-piece fit overestimates $v_{\rm s,max}$, the lower pressure MCMC samples get regularly accepted. Thirdly, the credible intervals are large below nuclear density because there is relatively little mass below nuclear density, and the model provides minimal information for how the core and crust EOSs are joined. This analysis would surely benefit from using a different EOS parameterization, such as the ones presented in Refs. [103] and [104].

5.4.2 Results dependencies

In our hypothetical scenario, we are passed a list of BNS detections made in a year's worth of 3-detector observing segments, and we chose to analyze the loudest 20 signals to put constraints on the NS EOS shown in Fig. 22. How would these results change if we chose more or less signals to analyze? The left plots in Fig. 23 demonstrates how the EOS constraints are affected by the number of signals analyzed. It turns out that the majority of EOS information is provided by the loudest $\sim$5 signals ($\rho_{\rm net} \gtrsim 20$), and the credible intervals do not noticeably improve by including any additional signals.

In Sec. 5.3, we outlined the prior distributions and constraints used in our analysis.

One of the constraints is that the NS EOS must stably support a 1.93 $M_\odot$ NS, which is derived from the observation of the massive pulsar J0348+0432. What if an even more massive NS is observed? To consider this effect, we take PSR B1957+20, which is a black widow pulsar found to have a mass of 2.40 ± 0.12 $M_\odot$, though a more conservative lower limit of 1.66 $M_\odot$ is more appropriate [105], and assume that its mass is 2.4 $M_\odot$. We present our results in the right plots of Fig. 23. The 2σ prior contours for the different maximum mass observations are plotted as dashed lines. By requiring proposed EOS to support NSs at 2.4 $M_\odot$, we find significantly tighter constraints on the lower bound of the pressure above $\rho \sim \rho_1$ and on the lower bound of the NS EOS for large masses. The upper bound for large densities and masses, however, does not change since it is determined by the causality requirement.

The mass distribution of our population was chosen to be uniform between 1.2–1.6 $M_\odot$. What if the true BNS mass distribution were actually higher or lower than expected? We might expect that a population of low-mass NSs would better constrain the EOS at low densities and a population of high-mass NSs would better constrain the EOS at high densities, since a NS's density increases with its mass. This is exactly what we see in the left plots in Fig. 24. Here, we compared four different populations: the baseline population containing NSs with masses uniformly distributed between 1.2–1.6 $M_\odot$, a population of just 1.0 $M_\odot$ NSs, a population of just 1.4 $M_\odot$ NSs, and a population of just 1.8 $M_\odot$ NSs. We analyzed the loudest 5 sources keeping everything else the same. Additionally, we find that the EOS constraints from the population of all 1.4 $M_\odot$ NSs are extremely similar, which suggests that even populations with very narrow mass distributions can provide valuable constraints on the NS EOS.

We also found consistent results to those in Fig. 22 when considering different "true" EOSs. Since these MCMC runs are computationally expensive, we considered parameter estimation on various EOSs using the Fisher Information Matrix (FM). First, we demonstrated a remarkable consistency between MCMC results and FM results. We then considered a handful of candidate EOSs, and showed that they too result in tight EOS constraints and that these constraints are effective at ruling out false EOS models. The results of this analysis can be found in Ref. [95].

5.4.3 Statistical and systematic error

In Sec. 5.4.1, we model the event rate by a Poisson process and determine the number of systems to simulate within a given volume by drowning from a Poisson distribution. What effect does this have on our analysis? In the right plots in Fig. 24, we consider four additional populations with exactly the same properties but a different draw from the Poisson distribution. Our results seem roughly consistent across the different populations.

In each of our results so far, we injected signals into zero-noise to estimate the most probable measurement uncertainty of EOS parameters. How much might individual noise realizations affect our results? In the left plots in Fig. 25, we inject the loudest 5 signals into different realizations of synthetic noise, and we do this 5 different times. Again, our results seem roughly consistent across the different noise realizations, and the statistical error from a given noise distribution will only be washed out more by analyzing additional signals. Also, as expected, the zero-noise results seem to be an average representation of the contours from different noise realizations.

As demonstrated in Sec. 4.5.1, the biggest obstacle to measuring the NS EOS with advanced GW detectors is the systematic error from waveform uncertainty. The right plots in Fig. 25 reiterate the effects of modeling bias in our pN waveforms on EOS parameter estimation. Here we plot the results from three different runs where we inject the loudest 5 signals from our baseline population into zero-noise using the TaylorT1, TaylorF2, and TaylorT4 waveform approximants. For each run, we use TaylorF2 templates for parameter estimation. Since each pN waveform is equally reliable to the same pN order, this models our ignorance of the true waveform. We find that using pN waveforms results in systematic error that is large enough to significantly bias the EOS measurements.

5.5 Conclusion

We have presented a new method to measure the NS EOS through the estimation of the EOS parameters of a 4-piece polytropic model. We have shown through a full Bayesian analysis of a simulated BNS population consistent with "realistic" merger rates that advanced detectors ca measure the NS EOS to better than ± 1 km. If achieved, such

constraints would be an extraordinary achievement.

We also outlined the dependencies and sources of error for our results. We notably find that (*i*) the majority of the information used to constrain the NS EOS when combining many BNS signals comes from the loudest $\sim$5 sources, which roughly correspond to a $\rho_{\rm net} \gtrsim 20$, (*ii*) the incorporation the of the existence of an even heavier NS into the prior distribution can lead to much tighter EOS constraints at large masses and densities but does not affect constraints near small masses and densities, and (*iii*) our results do not depend significantly on the particular realization of the chosen population or the particular noise realizations into which each signal was injected. Our results also reveal error due to the chosen EOS model. An avenue of future development would be to incorporate an EOS model such as the one presented in Ref. [103] or [104] into this analysis. Systematic errors due to waveform uncertainty are still the biggest obstacle to overcome. Accurate waveform models that can be quickly generated and run through a full Bayesian analysis in a reasonable amount of time must be developed and incorporated into our analysis routines in order to make the kind of measurements presented in the chapter.

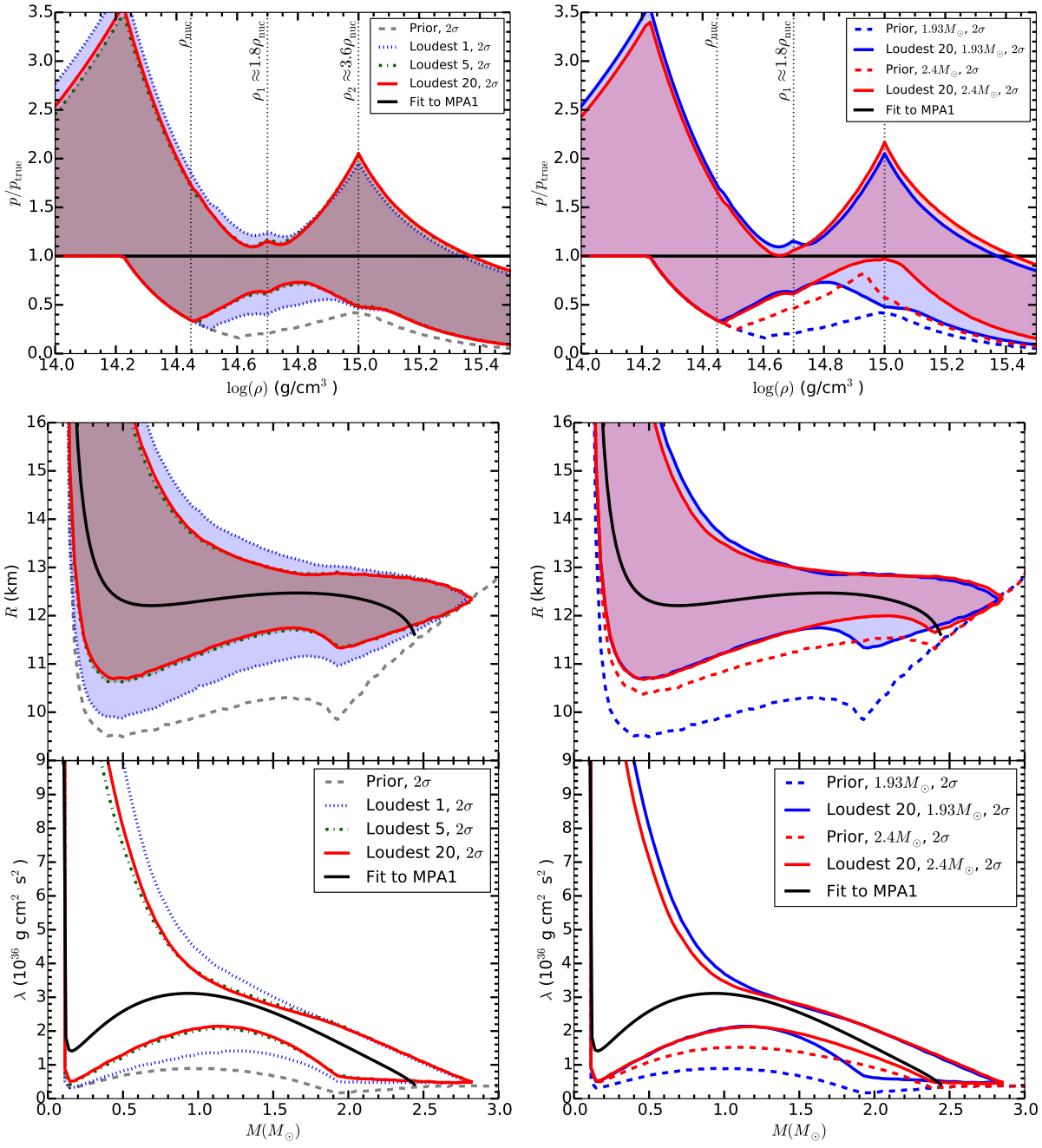

Figure 23 : Measurement uncertainty in the recovered EOS $p(\rho)$, radius $R(m)$, and tidal deformability $\lambda(m)$ with the baseline BNS population. (Left) Contours represent the 2σ credible regions for the loudest 1, 5, and 20 events. The dashed gray line is the lower limit on the 2σ credible region from just the maximum observed mass and causality priors. (Right) Contours represent the 2σ credible regions for the loudest 20 events. The maximum observed NS mass is varied from 1.93 $M_\odot$ (blue) to 2.4 $M_\odot$ (blue).

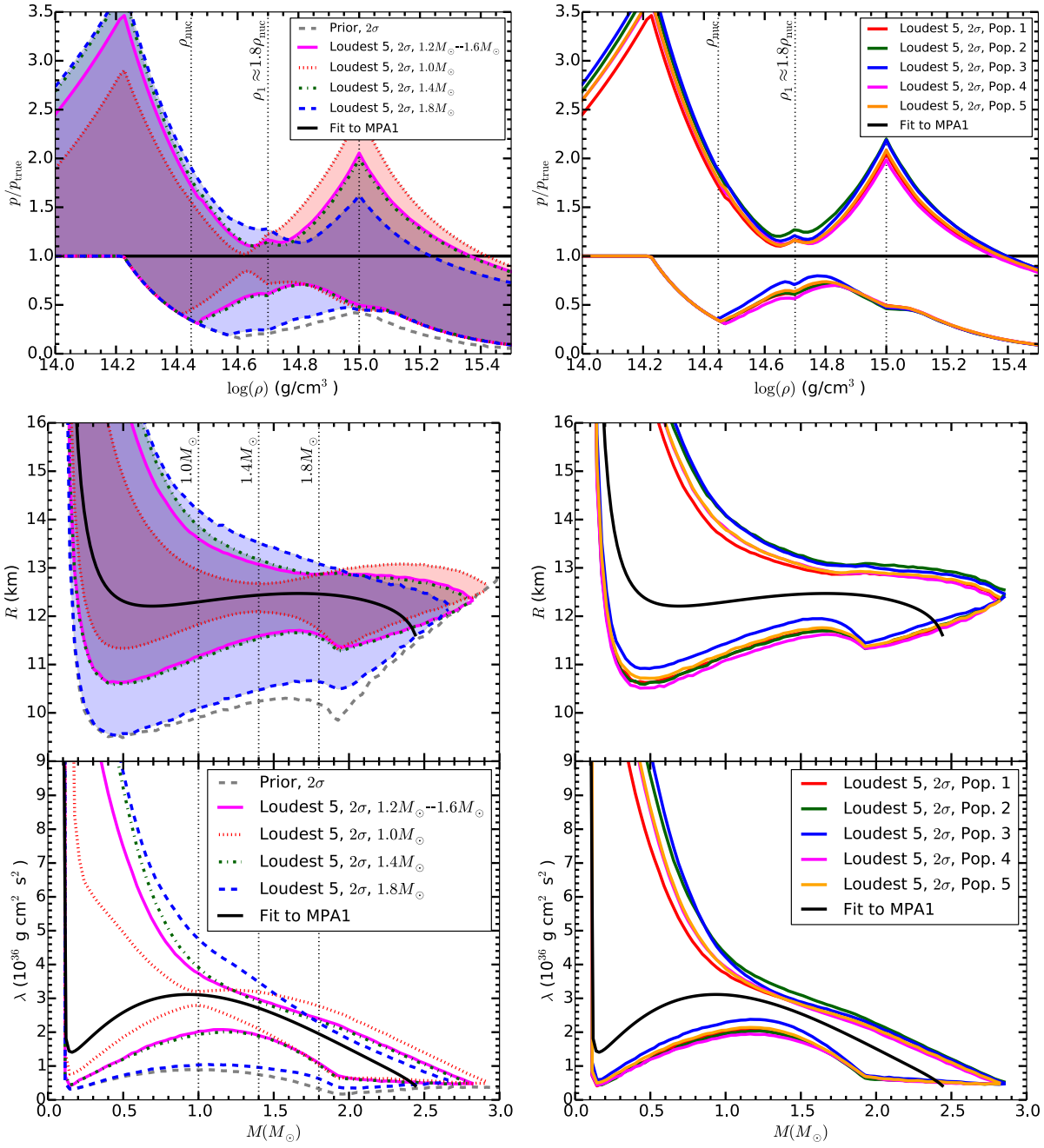

Figure 24 : Measurement uncertainty in the recovered EOS $p(\rho)$, radius $R(m)$, and tidal deformability $\lambda(m)$. (Left) Contours represent the 2σ credible regions for the loudest 5 events. Results use a variation of the baseline population where all parameters are kept the same except the masses are varied to be all 1.0 $M_\odot$ (green dot-dashed), all 1.4 $M_\odot$ (blue dashed), and all 1.8 $M_\odot$ (magenta) and the associated tidal parameters. Also shown is the lower limit of the 2σ credible region from just the maximum observable mass and causality priors. (Right) Contours represent the 2σ credible regions for the loudest 5 events. Results represent five different populations with the same event rate as the baseline population.

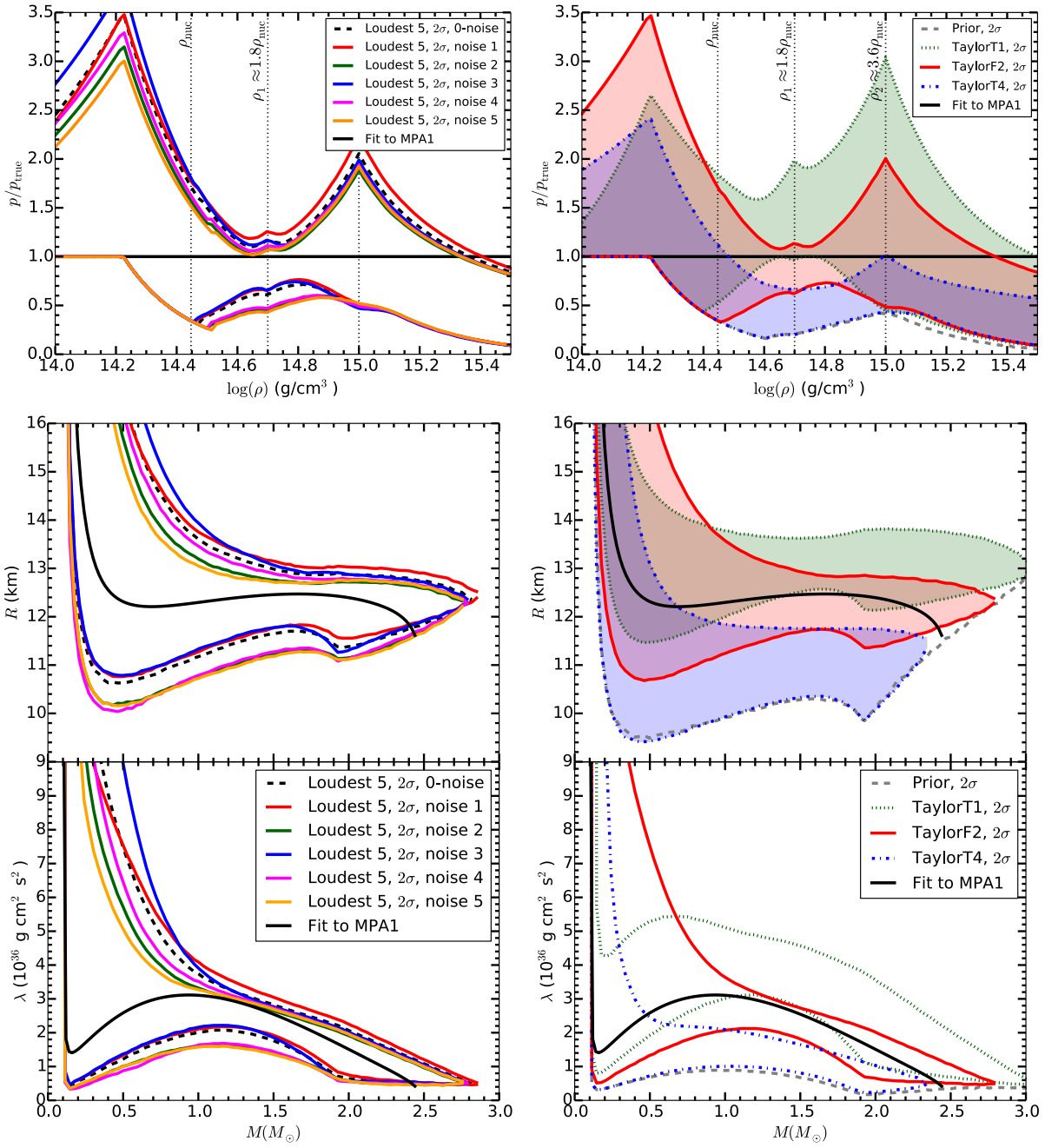

Figure 25 : Measurement uncertainty in the recovered EOS $p(\rho)$, radius $R(m)$, and tidal deformability $\lambda(m)$ with the baseline BNS population. (Left) Contours represent the 2σ credible regions for the loudest 5 events in five different noise realizations. (Right) Contours represent the 2σ credible regions for the loudest 5 events injected using the waveform families labeled in the legend and recovered with TaylorF2 templates. Also shown is the lower limit of the 2σ credible region from just the maximum observable mass and causality priors.

Chapter 6

Conclusion

With the advanced detector era of GW physics rapidly approaching, the first direct detections of gravitational waves are just on the horizon. This dissertation presents work on two promising sources of GWs detectable with advanced detectors: 1) isolated, rotating NSs, and 2) compact binary coalescences.

In Ch. 2, we used a simulated population of isolated, rotating NSs to assess the detectability of the Galactic NS population through detection of their continuous-wave emission and demonstrate how the number of detections can place meaningful constraints on the properties of such a population. To do so, we evolved each star's frequency through a combination of electromagnetic and gravitational emission, which are respectively driven by the star's magnetic field and ellipticity. Since the GW strain depends on both the ellipticity and orbital frequency of the star, which depends on the magnetic field and ellipticity, the number of detections made by aLIGO can place constraints on these parameters. While our simulated population is admittedly primitive, this project was meant to demonstrate how aLIGO can inform us about the magnetic field and ellipticity properties of Galactic NSs. Future work involves upgrading our population to be more realistic by incorporating distributions in magnetic field and ellipticity, for instance.

Ch. 3 discusses the development of a CBC search for IMBHBs. Though the existence of IMBHBs is still uncertain, if they do exist, they could be prime candidates for aLIGO. In fact, advanced GW detectors might just be our best chance at a conclusive IMBH detection. While a burst search for IMBHBs was performed on previous science runs,

we propose to run a CBC search in addition to the burst search due to the improved low-frequency sensitivity of the advanced detectors. IMBHB signals will be in band long enough to warrant a matched filter search using CBC waveform models as filters. In our first MDC, we demonstrated aLIGO's incredible reach to large IMBHB sources, which extends up to ∼1,000 Mpc and probes cosmological scales! However, only non-spinning systems were considered for simplicity. Our second MDC endeavors to test the search's sensitivity to spinning and precessing signals. Preliminary results point to transitioning to an aligned-spin template bank to maintain and even surpass the sensitive distances quoted in MDC1, but more investigations are needed before such a conclusion is definitive. We will also have to explore the search's sensitivity to the entire IMBHB mass parameter space, and we hope to do this in an upcoming engineering run.

Ch. 4 studies the prospect of measuring the tidal interactions of BNS systems as they coalesce. Leading-order and next-to-leading-order tidal corrections to PN waveforms affect the high-frequency portion of the CBC waveform and can be parameterized by a single parameter for each component. We outline the measurability of a linear combination of these two parameters for various mass combinations and a moderate EOS.

The real quantity of interest is not the tidal parameters but the NS EOS. In Ch. 5, we present a method to directly measure the EOS by measuring the parameters of a robust EOS model. This method allows for the combination of information from many BNS detections as well as the easy incorporation of physical and observational prior information that help to improve measurability. We show that advanced detectors at design sensitivity are capable of measuring the radii of NSs with canonical masses to within a kilometer, which would be an extremely tight constraint on the NS EOS if achieved.

The last remaining obstacle to overcome in order to make accurate EOS measurements are models that can generate waveforms quickly enough to be run through a full Bayesian parameter estimation routine but accurately enough to make unbiased measurements. In Chs. 4 and 5, we observe large systematic error in EOS measurements from PN waveforms with leading-order and next-to-leading-order tidal corrections. Such systematic error can only be overcome through the development of waveforms that are more accurate. No

waveforms yet exist that simultaneously satisfy the following two conditions: (*i*) they accurately capture EOS effects at high frequencies, and (*ii*) they are efficient enough in generation to be used in a full Bayesian parameter estimation routine.

By Fall of this year, aLIGO will be coming online. In this dissertation, we have presented work geared toward three capabilities of advanced detectors: 1) The ability to learn more about the Galactic NS population, 2) the possibility of the first conclusive detection of IMBHs, and 3) potential NS EOS constraints as tight as ± 1 km for NSs with canonical masses. With all this and more on the horizon, the next several years promise to be an exciting time to be a gravitational-wave physicist!

Bibliography

[1] Jocelyn S. Read, Benjamin D. Lackey, Benjamin J. Owen, and John L. Friedman. Constraints on a phenomenologically parameterized neutron-star equation of state. *Phys.Rev.*, D79:124032, 2009.

[2] Eanna E. Flanagan and Scott A Hughes. The basics of gravitational wave theory. *New J. Phys.*, 7(204), 2005.

[3] J.M. Weisberg and J.H. Taylor. Relativistic binary pulsar b1913+16: Thirty years of observations and analysis.

[4] B. Abbott et al. Setting upper limits on the strength of periodic gravitational waves from psr j1939+2134 using the first science data from the geo 600 and ligo detectors. *Physical Review D*, 69(8), 2004.

[5] B. Abbott et al. First upper limits from ligo on gravitational wave bursts. *Physical Review D*, 69(10), 2004.

[6] B. Abbott et al. Analysis of ligo data for gravitational waves from binary neutron stars. *Physical Review D*, 69(12), 2004.

[7] B. Abbott et al. Analysis of first ligo science data for stochastic gravitational waves. *Physical Review D*, 69(12), 2004.

[8] J. Aasi et al. Prospects for Localization of Gravitational Wave Transients by the Advanced LIGO and Advanced Virgo Observatories. 2013.

[9] J. D. E. Creighton and W. G. Anderson. *Gravitational-Wave Physics and Astronomy.* Wiley-VCH, Weinheim, Germany, 2011.

[10] Alessandra Buonanno, Bala Iyer, Evan Ochsner, Yi Pan, and B.S. Sathyaprakash. Comparison of post-Newtonian templates for compact binary inspiral signals in gravitational-wave detectors. *Phys.Rev.*, D80:084043, 2009.

[11] Alessandra Buonanno, Yi Pan, John G. Baker, Joan Centrella, Bernard J. Kelly, Sean T. McWilliams, and James R. van Meter. Approaching faithful templates for nonspinning binary black holes using the effective-one-body approach. *Physical Review D*, 76(10), 2007.

[12] A. Buonanno and T. Damour. Effective one-body approach to general relativistic two-body dynamics. *Physical Review D*, 59(8), 1999.

[13] Leslie Wade, Xavier Siemens, David L. Kaplan, Benjamin Knispel, and Bruce Allen. Continuous gravitational waves from isolated galactic neutron stars in the advanced detector era. *Physical Review D*, 86(12), 2012.

[14] C. Misner, K. Thorne, and J. Wheeler. *Gravitation*. W. H. Freeman, 1973.

[15] D. Lorimer and M. Kramer. *Handbook of Pulsar Astronomy*. Cambridge University Press, 2004.

[16] Stephen Hawking and Werner Israel, editors. *300 Years of Gravitation*. Cambridge University Press, Cambridge, 1987.

[17] B. Abbott et al. Coherent searches for periodic gravitational waves from unknown isolated sources and Scorpius X-1: Results from the second LIGO science run. *Phys.Rev.*, D76:082001, 2007.

[18] B. Knispel and B. Allen. Blandford's argument: The strongest continuous gravitational wave signal. *Phys.Rev.D*, 78(4):044031, August 2008.

[19] C. Palomba. Simulation of a population of isolated neutron stars evolving through the emission of gravitational waves. *Monthly Notices of the RAS*, 359:1150–1164, May 2005.

[20] P. Esposito, N. Rea, R. Turolla, G. L. Israel, S. Zane, L. Stella, C. Kouveliotou, S. Mereghetti, A. Tiengo, D. Götz, and E. Göğüş. SGR 0418+5729: a low-magnetic-field magnetar. In M. Burgay, N. D'Amico, P. Esposito, A. Pellizzoni, and A. Possenti, editors, *American Institute of Physics Conference Series*, volume 1357 of *American Institute of Physics Conference Series*, pages 181–184, August 2011.

[21] N. Rea, J. A. Pons, D. F. Torres, and R. Turolla. The Fundamental Plane for Radio Magnetars. *Astrophysical Journal, Letters*, 748:L12, March 2012.

[22] A. Spitkovsky. Pulsar Magnetosphere: The Incredible Machine. In C. Bassa, Z. Wang, A. Cumming, and V. M. Kaspi, editors, *40 Years of Pulsars: Millisecond Pulsars, Magnetars and More*, volume 983 of *American Institute of Physics Conference Series*, pages 20–28, February 2008.

[23] GSL Project Contributors. GSL - GNU scientific library - GNU project - free software foundation (FSF). http://www.gnu.org/software/gsl/, 2010.

[24] R. N. Manchester, G. B. Hobbs, A. Teoh, and M. Hobbs. The Australia Telescope National Facility Pulsar Catalogue. *Astronomical Journal*, 129:1993–2006, April 2005.

[25] D. Shoemaker. *Advanced LIGO anticipated sensitivity curves*. LSC, 2009.

[26] B.P. Abbott et al. Einstein@Home search for periodic gravitational waves in early S5 LIGO data. *Phys.Rev.*, D80:042003, 2009.

[27] R. Diehl, H. Halloin, K. Kretschmer, G. G. Lichti, V. Schönfelder, A. W. Strong, A. von Kienlin, W. Wang, P. Jean, J. Knödlseder, J.-P. Roques, G. Weidenspointner, S. Schanne, D. H. Hartmann, C. Winkler, and C. Wunderer. Radioactive ^{26}Al from massive stars in the Galaxy. *Nature*, 439:45–47, January 2006.

[28] J. A. Pons, J. A. Miralles, and U. Geppert. Magneto-thermal evolution of neutron stars. *Astronomy and Astrophysics*, 496:207–216, March 2009.

[29] S. B. Popov, J. A. Pons, J. A. Miralles, P. A. Boldin, and B. Posselt. Population synthesis studies of isolated neutron stars with magnetic field decay. *Monthly Notices of the RAS*, 401:2675–2686, February 2010.

[30] A. M. Ghez, S. Salim, S. D. Hornstein, A. Tanner, J. R. Lu, M. Morris, E. E. Becklin, and G. Duchêne. Stellar orbits around the galactic center black hole. *ApJ*, 620:744, 2005.

[31] Jerome A. Orosz. Inventory of black hole binaries.

[32] M. Coleman Miller and E.J.M Colbert. Intermediate-mass black holes.

[33] S. Markoff, H. Falcke, and R. Fender. A jet model for the broadband spectrum of xte j1118+480 - synchrotron emission from radio to x-rays in the low/hard spectral state. *Astronomy & Astrophysics*, 372(2):4, 2001.

[34] Giulio Mazzolo. *Search for intermediate mass black hole binaries with networks of ground-based gravitational-wave detectors*. PhD thesis, Von der Fakult at fu r Mathematik und Physik der Gottfried Wilhelm Leibniz Universita t Hannover zur Erlangung des Grades, 2013.

[35] Dheeraj R. Pasham, Tod E. Strohmayer, and Richard F. Mushotzky. A 400-solar-mass black hole in the galaxy m82. *Nature*, 513(7516):74–6, 2014.

[36] P. A. Crowther et al. The r136 star cluster hosts several stars whose individual masses greatly exceed the accepted 150 m stellar mass limit. *MNRAS*, 408(731), 2010.

[37] Krzysztof Belczynski et al. The formation and gravitational-wave detection of massive stellar black hole binaries. *ApJ*, 789(120), 2014.

[38] J. Aasi et al. Search for gravitational radiation from intermediate mass black hole binaries in data from the second ligo-virgo joint science run. *Phys. Rev. D*, 89(122003), 2014.

[39] J. Abadie et al. Search for gravitational waves from intermediate mass binary black holes. *Phys. Rev. D*, 85(102004), 2012.

[40] Bruce Allen, Warren G. Anderson, Patrick R. Brady, Duncan A. Brown, and Jolien D. E. Creighton. Findchirp: An algorithm for detection of gravitational waves from inspiraling compact binaries. *Physical Review D*, 85(12), 2012.

[41] Benjamin J. Owen. Matched filtering of gravitational waves from inspiraling compact binaries: Computational cost and template placement. *Physical Review D*, 60(2), 1999.

[42] Kipp Cannon, Romain Cariou, Adrian Chapman, Mireia Crispin-Ortuzar, Nickolas Fotopoulos, Melissa Frei, Chad Hanna, Erin Kara, Drew Keppel, Laura Liao, Stephen Privitera, Antony Searle, Leo Singer, and Alan Weinstein. Toward early-warning detection of gravitational waves from compact binary coalescence. 07 2011.

[43] Stephen Privitera. *The Importance of Spin for Observing Gravitational Waves from Coalescing Compact Binaries with LIGO and Virgo*. PhD thesis, California Institute of Technology, 2014.

[44] Kipp Cannon, Chad Hanna, and Drew Keppel. Method to estimate the significance of coincident gravitational-wave observations from compact binary coalescence. *Physical Review D*, 88(2), 2013.

[45] Bruce Allen. χ^2 time-frequency discriminator for gravitational wave detection. *Physical Review D*, 71(6), 2005.

[46] Stephen Privitera, Satyanarayan R. P. Mohapatra, Parameswaran Ajith, Kipp Cannon, Nickolas Fotopoulos, Melissa A. Frei, Chad Hanna, Alan J. Weinstein, and John T. Whelan. Improving the sensitivity of a search for coalescing binary black holes with nonprecessing spins in gravitational wave data. *Phys. Rev. D*, 89(024003), January 2014.

[47] LSC algorithm library.

[48] Alessandra Buonanno, Yanbei Chen, and Thibault Damour. Transition from inspiral to plunge in precessing binaries of spinning black holes. *Physical Review D*, 74(10), 2006.

[49] P. Ajith et al. Inspiral-merger-ringdown waveforms for black-hole binaries with nonprecessing spins. *Physical Review Letters*, 106(24), 2011.

[50] Kipp Cannon, Chad Hanna, and Jacob Peoples. Likelihood-ratio ranking statistic for compact binary coalescence candidates with rate estimation. 2015.

[51] L. Wade, J. D. E. Creighton, E. Ochsner, B. D. Lackey, B. F. Farr, T. B. Littenberg, and V. Raymond. Systematic and statistical errors in a bayesian approach to the estimation of the neutron-star equation of state using advanced gravitational wave detectors. *Phys.Rev.D*, 89:103012, May 2014.

[52] Gregory M Harry and the LIGO Scientific Collaboration. Advanced ligo: the next generation of gravitational wave detectors. *Classical and Quantum Gravity*, 27(8):084006, 2010.

[53] J. Abadie et al. Predictions for the Rates of Compact Binary Coalescences Observable by Ground-based Gravitational-wave Detectors. *Class.Quant.Grav.*, 27:173001, 2010.

[54] J. Abadie et al. Search for Gravitational Waves from Low Mass Compact Binary Coalescence in LIGO's Sixth Science Run and Virgo's Science Runs 2 and 3. *Phys.Rev.*, D85:082002, 2012.

[55] J. Aasi et al. Search for Gravitational Waves from Binary Black Hole Inspiral, Merger and Ringdown in LIGO-Virgo Data from 2009-2010. *Phys.Rev.*, D87:022002, 2013.

[56] Marc van der Sluys, Vivien Raymond, Ilya Mandel, Christian Rover, Nelson Christensen, et al. Parameter estimation of spinning binary inspirals using Markov-chain Monte Carlo. *Class.Quant.Grav.*, 25:184011, 2008.

[57] M.V. van der Sluys, C. Roever, A. Stroeer, N. Christensen, Vicky Kalogera, et al. Gravitational-Wave Astronomy with Inspiral Signals of Spinning Compact-Object Binaries. 2007.

[58] J. Aasi et al. Parameter estimation for compact binary coalescence signals with the first generation gravitational-wave detector network. *Phys.Rev.*, D88:062001, 2013.

[59] Eanna E. Flanagan and Tanja Hinderer. Constraining neutron star tidal Love numbers with gravitational wave detectors. *Phys.Rev.*, D77:021502, 2008.

[60] Tanja Hinderer, Benjamin D. Lackey, Ryan N. Lang, and Jocelyn S. Read. Tidal deformability of neutron stars with realistic equations of state and their gravitational wave signatures in binary inspiral. *Phys.Rev.*, D81:123016, 2010.

[61] Jocelyn S. Read, Charalampos Markakis, Masaru Shibata, Koji Uryu, Jolien D.E. Creighton, et al. Measuring the neutron star equation of state with gravitational wave observations. *Phys.Rev.*, D79:124033, 2009.

[62] Francesco Pannarale, Luciano Rezzolla, Frank Ohme, and Jocelyn S. Read. Will black hole-neutron star binary inspirals tell us about the neutron star equation of state? *Phys.Rev.*, D84:104017, 2011.

[63] Jocelyn S. Read, Luca Baiotti, Jolien D. E. Creighton, John L. Friedman, Bruno Giacomazzo, et al. Matter effects on binary neutron star waveforms. *Phys.Rev.*, D88:044042, 2013.

[64] Benjamin D. Lackey, Koutarou Kyutoku, Masaru Shibata, Patrick R. Brady, and John L. Friedman. Extracting equation of state parameters from black hole-neutron star mergers: aligned-spin black holes and a preliminary waveform model. 2013.

[65] Thibault Damour, Alessandro Nagar, and Loic Villain. Measurability of the tidal polarizability of neutron stars in late-inspiral gravitational-wave signals. *Phys.Rev.*, D85:123007, 2012.

[66] Andrea Maselli, Leonardo Gualtieri, and Valeria Ferrari. Constraining the equation of state of nuclear matter with gravitational wave observations: Tidal deformability and tidal disruption. 2013.

[67] Michele Vallisneri. Beyond Fisher: exact sampling distributions of the maximum-likelihood estimator in gravitational-wave parameter estimation. *Phys.Rev.Lett.*, 107:191104, 2011.

[68] Carl L. Rodriguez, Benjamin Farr, Will M. Farr, and Ilya Mandel. Inadequacies of the Fisher Information Matrix in gravitational-wave parameter estimation. *Phys.Rev.*, D88:084013, 2013.

[69] R. O'Shaughnessy, B. Farr, E. Ochsner, Hee-Suk Cho, C. Kim, et al. Parameter Estimation of Gravitational Waves from Nonprecessing BH-NS Inspirals with higher harmonics: Comparing MCMC posteriors to an Effective Fisher Matrix. 2013.

[70] Hee-Suk Cho, Evan Ochsner, Richard O'Shaughnessy, Chunglee Kim, and Chang-Hwan Lee. Gravitational waves from BH-NS binaries: Effective Fisher matrices and parameter estimation using higher harmonics. *Phys.Rev.*, D87:024004, 2013.

[71] Walter Del Pozzo, Tjonnie G. F. Li, Michalis Agathos, Chris Van Den Broeck, and Salvatore Vitale. Demonstrating the feasibility of probing the neutron star equation of state with second-generation gravitational wave detectors. 2013.

[72] Kent Yagi and Nicolas Yunes. Love can be Tough to Measure. 2013.

[73] Marc Favata. Systematic parameter errors in inspiraling neutron star binaries. 2013.

[74] Advanced Virgo Baseline Design. https://wwwcascina.virgo.infn.it/advirgo/docs.html, May 16, 2009. VIR-027A-09.

[75] Stefano Foffa and Riccardo Sturani. Effective field theory methods to model compact binaries. 2013.

[76] Justin Vines, Éanna É. Flanagan, and Tanja Hinderer. Post-1-newtonian tidal effects in the gravitational waveform from binary inspirals. *Phys. Rev. D*, 83:084051, Apr 2011.

[77] Norman K. Glendenning. *Compact Stars: Nuclear Physics, Particle Physics, and General Relativity*. Springer-Verlag, NewYork, second edition, 2000.

[78] Bruce Allen, Jolien D.E. Creighton, Eanna E. Flanagan, and Joseph D. Romano. Robust statistics for deterministic and stochastic gravitational waves in nonGaussian noise. 1. Frequentist analyses. *Phys.Rev.*, D65:122002, 2002.

[79] J. Veitch et al. Parameter estimation for compact binaries with ground-based gravitational-wave observations using the lalinference software library. *Physical Review D*, 91(4), 2015.

[80] C. Messenger and J. Read. Measuring a cosmological distance-redshift relationship using only gravitational wave observations of binary neutron star coalescences. *Phys.Rev.Lett.*, 108:091101, 2012.

[81] Advanced LIGO anticipated sensitivity curves. https://dcc.ligo.org/cgi-bin/DocDB/ShowDocument?docid=2974.

[82] Alessandro Manzotti and Alexander Dietz. Prospects for early localization of gravitational-wave signals from compact binary coalescences with advanced detectors. 2012.

[83] Ilya Mandel, Christopher P L Berry, Frank Ohme, Stephen Fairhurst, and Will M Farr. Parameter estimation on compact binary coalescences with abruptly terminating gravitational waveforms. 2014.

[84] Carl L Rodriguez, Benjamin Farr, Vivien Raymond, Will M Farr, Tyson Littenberg, et al. Basic Parameter Estimation of Binary Neutron Star Systems by the Advanced LIGO/Virgo Network. 2013.

[85] Samaya Nissanke, Daniel E. Holz, Scott A. Hughes, Neal Dalal, and Jonathan L. Sievers. Exploring short gamma-ray bursts as gravitational-wave standard sirens. *Astrophys.J.*, 725:496–514, 2010.

[86] Laura Sampson, Neil Cornish, and Nicolas Yunes. Gravitational Wave Tests of Strong Field General Relativity with Binary Inspirals: Realistic Injections and Optimal Model Selection. *Phys.Rev.*, D87(10):102001, 2013.

[87] Tyson B. Littenberg, John G. Baker, Alessandra Buonanno, and Bernard J. Kelly. Systematic biases in parameter estimation of binary black-hole mergers. *Phys.Rev.*, D87:104003, 2013.

[88] L. Lindblom. Determining the nuclear equation of state from neutron-star masses and radii. *ApJ*, 398:569–573, October 1992.

[89] Lee Lindblom and Nathaniel M. Indik. A Spectral Approach to the Relativistic Inverse Stellar Structure Problem. *Phys.Rev.*, D86:084003, 2012.

[90] Lee Lindblom and Nathaniel M. Indik. Spectral Approach to the Relativistic Inverse Stellar Structure Problem II. 2013.

[91] James M. Lattimer. The nuclear equation of state and neutron star masses. *Ann.Rev.Nucl.Part.Sci.*, 62:485–515, 2012.

[92] David Radice, Luciano Rezzolla, and Filippo Galeazzi. Beyond second-order convergence in simulations of binary neutron stars in full general-relativity. 2013.

[93] Andrew W. Steiner, James M. Lattimer, and Edward F. Brown. The Equation of State from Observed Masses and Radii of Neutron Stars. *Astrophys.J.*, 722:33–54, 2010.

[94] Lee Lindblom. Spectral Representations of Neutron-Star Equations of State. *Phys.Rev.*, D82:103011, 2010.

[95] Benjamin D. Lackey and Leslie Wade. Reconstructing the neutron-star equation of state with gravitational-wave detectors from a realistic population of inspiralling binary neutron stars. *Phys. Rev. D*, 91(4), 2015.

[96] Francesco Pannarale, Emanuele Berti, Koutarou Kyutoku, and Masaru Shibata. Nonspinning black hole-neutron star mergers: a model for the amplitude of gravitational waveforms. *Physical Review D 88,*, 084011, 2013.

[97] L. Lindblom. Determining the nuclear equation of state from neutron-star masses and radii. *ApJ*, 398:569–573, October 1992.

[98] J. M. Lattimer and M. Prakash. Neutron star structure and the equation of state. *The Astrophysical Journal*, 550(1), 2001.

[99] J. S. Read, B. D. Lackey, B. J. Owen, and J. L. Friedman. Constraints on a phenomenologically parametrized neutron-star equation of state. *Phys.Rev.D*, 79(12):124032, June 2009.

[100] W. Del Pozzo, T. G. F. Li, M. Agathos, C. Van Den Broeck, and S. Vitale. Demonstrating the Feasibility of Probing the Neutron-Star Equation of State with Second-Generation Gravitational-Wave Detectors. *Physical Review Letters*, 111(7):071101, August 2013.

[101] D. Foreman-Mackey, D. W. Hogg, D. Lang, and J. Goodman. emcee: The MCMC Hammer. *PASP*, 125:306–312, March 2013.

[102] F. Özel, D. Psaltis, R. Narayan, and A. Santos Villarreal. On the Mass Distribution and Birth Masses of Neutron Stars. *ApJ*, 757:55, September 2012.

[103] A. W. Steiner, J. M. Lattimer, and E. F. Brown. The Equation of State from Observed Masses and Radii of Neutron Stars. *ApJ*, 722:33–54, October 2010.

[104] L. Lindblom. Spectral representations of neutron-star equations of state. *Phys.Rev.D*, 82(10):103011, November 2010.

[105] M. H. van Kerkwijk, R. P. Breton, and S. R. Kulkarni. Evidence for a Massive Neutron Star from a Radial-velocity Study of the Companion to the Black-widow Pulsar PSR B1957+20. *ApJ*, 728:95, February 2011.

Leslie Wade

Education

Period	**September 2009 – Present**
Degree	**Doctor of Philosophy in Physics, expected May 2015**
School	**University of Wisconsin - Milwaukee** Milwaukee, WI

- Dissertation: *Gravitational waves from rotating neutron stars and compact binary systems*
- Advisors: Jolien Creighton and Xavier Siemens
- Ranked #14 for Cosmology/Relativity/Gravity graduate programs by U.S. News & World Report, 2014
- Awards: Student Success Award (for teaching), Research Excellence Award, Chancellor's Grad. Student Award, Physics Grad. Student Award

Period	**September 2005 – May 2009**
Degree	**Bachelor of Science in Physics, with Honors**
School	**Bates College** Lewiston, ME

- Honors Thesis: *Electromagnetically induced transparency*
- Advisor: Lilian Childress
- Honors: *Magna Cum Laude*, Phi Betta Kappa, Sigma Xi, Deans List, NESCAC All-Academic 2008 – 2009
- President of the Society of Physics Students (Fall 2008 – May 2009)

Recent Scientific Employment / Fellowships

Period	**Summer 2012 – Spring 2013, Summer 2014 – Spring 2015**
Fellowship	**Wisconsin Space Grant Consortium Graduate Fellowship**

- Summer 2014 – Spring 2015: *Reconstructing the neutron-star equation of state with gravitational-wave detectors from a realistic population of inspiralling binary neutron stars* (Lackey, Wade, 2014)
- Summer 2012 – Spring 2013: *Continuous gravitational waves from isolated galactic neutron stars in the advanced detector era* (Wade et. al, 2012)

Period	**Summer 2010 – Fall 2012, Spring – Fall 2013, Summer 2014**
Position	**Research Assistant**
School	**University of Wisconsin - Milwaukee** Milwaukee, WI

- Advisors: Jolien Creighton and Xavier Siemens
- For more details, see "Primary Ph.D. Research Experience".

Period	**Fall 2009 – Spring 2010, Fall 2012, Spring 2014, Fall 2014**
Position	**Teaching Assistant**
School	**University of Wisconsin - Milwaukee** Milwaukee, WI

- Primary "Intermediate Algebra" lecturer (Fall 2014)
- Led discussion sessions for "Physics for the Health Professions" (Spring 2014), "Physics in Everyday Life" (Fall 2012), and "General Physics I" (Fall 2009 – Spring 2010)

Teaching Experience

Period **Fall 2014 – Present**
Class **Intermediate Algebra**
Role **Sole Lecturer** UW - Milwaukee

- Lead two lecture sections. My primary responsibilities are chalk-board lecturing, grading, and coordinating with other sections to cover the same material.
- Gained experience with mastery-based education software called ALEKS
- Teaching evaluation scores: N/A (estimated department average: N/A)

Period **Spring 2014**
Class **Physics for the Health Professions**
Role **Discussion Leader** UW - Milwaukee

- Led three discussion sessions. My primary responsibilities were reviewing lecture material in a more engaging and interactive environment, setting up homework problems, and grading homework assignments and exams.
- Teaching evaluation scores: 3.75/4.00 (approx. dept. average: 3.37/4.00)

Period **Fall 2012**
Class **Physics in Everyday Life**
Role **Discussion Leader** UW - Milwaukee

- Led four discussion sessions. My primary responsibilities were to lead a captivating discussion that taught topics from lecture in a more engaging and interactive way.
- Teaching evaluation scores: 3.52/4.00 (approx. dept. average: 3.37/4.00)

Period **Fall 2009 – Spring 2010**
Class **General Physics I (Non-Calc)**
Role **Discussion Leader** UW - Milwaukee

- Led six discussion sections. My main responsibilities were to teach students how to solve problems similar to ones on their homeworks, quizzes, and exams. I also graded homeworks and quizzes.
- Teaching evaluation scores: 3.72/4.00 (approx. dept. average: 3.37/4.00)

Period **Fall 2008**
Classes **Introduction to Quantum Mechanics, Classical Physics**
Role **Tutor** Bates College

- Tutored students in various aspects of Quantum Mechanics and Classical Physics. Helped students set up difficult problems from homework and understand content from class.

Primary Ph.D. Research Experience

Period **Sprint 2014 – Present**
Project **A gravitational-wave search for intermediate mass black hole binaries**
Advisors **Jolien Creighton and Patrick Brady**

Leading the development of a matched filter search for gravitational waves from intermediate mass black hole binaries (IMBHB).

Period	**Spring 2014 – Present**
Project	**Reconstructing the neutron-star equation of state with gravitational-wave detectors from a realistic population of inspiralling binary neutron stars (Submitted to Phys. Rev. D)**
Advisor	**Jolien Creighton**

Demonstrated a new method to improve future neutron star equation of state constraints from gravitational-wave detectors by directly measuring a parameterized equation of state model (Lackey, Wade, 2014).

Period	**Winter 2012 – Present**
Project	**LALInference software development**
Advisor	**Jolien Creighton**

Contributing to the development of the Markov Chain Monte Carlo sampler in LALInference, which is a gravitational-wave data analysis software package used by the LIGO collaboration for Bayesian parameter estimation, by upgrading it to more efficiently measure tidal parameters.

Period	**Winter 2012 – Spring 2014**
Project	**Systematic and statistical errors in a bayesian approach to the estimation of the neutron-star equation of state using advanced gravitational-wave detectors (Published in Phys. Rev. D)**
Advisor	**Jolien Creighton**

Used bayesian simulations to study the measurability of equation-of-state parameters encoded in gravitational waves emitted by binary neutron stars, and demonstrated that the current gravitational waveforms were not yet suitable for estimating these parameters (Wade et. al, 2014).

Period	**Winter 2012 – Spring 2013**
Project	**LALSimulation software development**
Advisor	**Jolien Creighton**

Added first- and second-order tidal corrections to several post-Newtonian compact binary coalescence waveform families in LALSimulation, which is a gravitational-wave data analysis software package used by the LIGO collaboration to simulate gravitational waveforms.

Period	**Summer 2010 – Winter 2012**
Project	**Continuous gravitational waves from isolated galactic neutron stars in the advanced detector era (Published in Phys. Rev. D)**
Advisor	**Xavier Siemens**

Used a simulated neutron star population to assess the detectability of the isolated Galactic neutron star population and constrain its properties (Wade et. al, 2012).

Computer Skills

Languages and Tools	Proficiency in Python, C/C++, LaTeX, LAL, gstlal, GSL, SVN, Git, Vim Familiarity with bash scripting, FORTRAN, Mathematica, SQLite, and XML

Scientific Outreach / Volunteer Activities

Period	**Fall 2014**	
Activity	**Black Hole Bash Volunteer**	Milwaukee, WI
	Volunteered for the "Black Hole Bash" event hosted by the UW-Milwaukee Center for Gravitation, Cosmology, and Astrophysics, which educated the general public on black hole science.	
Period	**Fall 2011 – Fall 2012**	
Activity	**Astronomy Club**	Milwaukee, WI
	Attended and participated in the Astronomy club at the UW-Milwaukee.	
Period	**Fall 2011 – Fall 2012**	
Activity	**Tutor at Grace Fellowship Church of Milwaukee**	Milwaukee, WI
	Tutored elementary through high school aged students in the local community.	
Period	**Summer 2010, Fall 2010**	
Activity	**LIGO Science Monitor**	Hanford, WA
	Spent two weeks training and working as a science monitor at the LIGO Hanford Observatory.	

Publications

Primary Publications:

- B. D. Lackey and **L. Wade**. "Reconstructing the neutron-star equation of state with gravitational-wave detectors from a realistic population of inspiralling binary neutron stars". Phys. Rev. D, 91:043002, Feb 2015. (arXiv:1410.8866)

- J. Veitch, V. Raymond, B. Farr, W. M. Farr, P. Graff, S. Vitale, B. Aylott, K. Blackburn, N. Christensen, M. Coughlin, W. D. Pozzo, F. Feroz, J. Gair, C. J. Haster, V. Kalogera, T. Littenberg, I. Mandel, R. O'Shaughnessy, M. Pitkin, C. Rodriguez, C. Röver, T. Sidery, R. Smith, M. V. D. Sluys, A. Vecchio, W. Vousden, **L. Wade**. "Robust parameter estimation for compact binaries with gravitational-wave observations using LALInference". Phys. Rev. D, 91:042003, Feb 2015. (arXiv:1409.7215)

- **L. Wade**, J. D. E. Creighton, E. Ochsner, B. D. Lackey, B. F. Farr, T. B. Littenberg, and V. Raymond. "Systematic and statistical errors in a bayesian approach to the estimation of the neutron-star equation of state using advanced gravitational-wave detectors". Phys. Rev. D, 89:103012, May 2014. (arXiv:1402.5156)

- **L. Wade**, X. Siemens, D. L. Kaplan, B. Knispel, and B. Allen. "Continuous gravitational waves from isolated galactic neutron stars in the advanced detector era". Phys. Rev. D, 86:124011, Dec 2012. (arXiv:1209.2971)

LIGO Scientific Collaboration publications, of which I am an author:

- The LIGO Scientific Collaboration, the Virgo Collaboration: J. Aasi, et al. "Searching for stochastic gravitational waves using data from the two co-located LIGO Hanford detectors." Phys. Rev. D 91 (2015) 022003.

- The LIGO Scientific Collaboration, the Virgo Collaboration: J. Aasi, et al. "Improved Upper Limits on the Stochastic Gravitational-Wave Background from 2009-2010 LIGO and Virgo Data." Phys. Rev. Lett. 113 (2014) 231101.

- The IceCube Collaboration, The LIGO Scientific Collaboration, the Virgo Collaboration: M.G. Aartsen, et al. "Multimessenger Search for Sources of Gravitational Waves and High-energy Neutrinos: Results of the Initial LIGO-Virgo and IceCube." Phys. Rev. D 90 (2014) 102002.

- The LIGO Scientific Collaboration, the Virgo Collaboration: J. Aasi, et al. "Implementation of an F-statistic all-sky search for continuous gravitational waves in Virgo VSR1 data." Class. Quantum Grav. 31 (2014) 165014.

- The LIGO Scientific Collaboration, the Virgo Collaboration: J. Aasi, et al. "First all-sky search for continuous gravitational waves from unknown sources in binary systems." Phys. Rev. D 90 (2014), 062010.

- The LIGO Scientific Collaboration, the Virgo Collaboration: J. Aasi, et al. "First Searches for Optical Counterparts to Gravitational-wave Candidate Events". ApJS 211 (2014) 7.

- The LIGO Scientific Collaboration, the Virgo Collaboration: J. Aasi, et al. "Constraints on cosmic strings from the LIGO-Virgo gravitational-wave detectors". Phys. Rev. Lett. 112 (2014) 131101.
- The LIGO Scientific Collaboration, the Virgo Collaboration: J. Aasi, et al. "Application from a Hough search for continuous gravitational waves on data from the 5th LIGO science run". Class. Quantum Grav. 31 (2014) 085014.
- The LIGO Scientific Collaboration, the Virgo Collaboration: J. Aasi, et al. "The NINJA-2 project: Detecting and characterizing gravitational waveforms modelled using numerical binary black hole simulations". Class. Quantum Grav. 31 (2014) 115004.
- The LIGO Scientific Collaboration, the Virgo Collaboration: J. Aasi, et al. "Search for gravitational wave ringdowns from perturbed intermediate mass black holes in LIGO-Virgo data from 2005-2010". Phys. Rev D 89 (2014) 102006.
- The LIGO Scientific Collaboration, the Virgo Collaboration: J. Aasi, et al. "Search for gravitational waves associated with gamma-ray bursts detected by the InterPlanetary Network". Phys. Rev. Lett. 113 (2014) 011102.
- The LIGO Scientific Collaboration, the Virgo Collaboration: J. Aasi, et al. "Search for gravitational radiation from intermediate mass black hole binaries in data from the second LIGO-Virgo joint science run". Phys. Rev. D 89 (2014) 122003.
- The LIGO Scientific Collaboration, the Virgo Collaboration: J. Aasi, et al. "Methods and results of a search for gravitational waves associated with gamma-ray bursts using the GEO600, LIGO, and Virgo detectors". Phys. Rev. D 89 (2014) 122004.
- The LIGO Scientific Collaboration, the Virgo Collaboration: J. Aasi, et al. "Search for long-lived gravitational-wave transients coincident with long gamma-ray bursts". Phys. Rev. D 88 (2013) 122004.
- The LIGO Scientific Collaboration, the Virgo Collaboration: J. Aasi, et al. "A directed search for continuous Gravitational Waves from the Galactic Center". Phys. Rev. D 88 (2013) 102002.
- The LIGO Scientific Collaboration, the Virgo Collaboration: J. Aasi, et al. "Parameter estimation for compact binary coalescence signals with the first generation gravitational-wave detector network". Phys. Rev. D 88 (2013) 062001.
- The LIGO Scientific and the Virgo Collaborations: J. Aasi, et al. "Search for Gravitational Waves from Binary Black Hole Inspiral, Merger and Ringdown in LIGO-Virgo Data from 2009-2010". Phys. Rev. D 87 (2013) 022002.
- The LIGO Scientific and the Virgo Collaborations: J. Aasi, et al. "Einstein@Home all-sky search for periodic gravitational waves in LIGO S5 data". Phys. Rev. D 87 (2013) 042001.
- The LIGO Scientific Collaboration. "Enhancing the sensitivity of the LIGO gravitational wave detector by using squeezed states of light". Nature Photonics 7 (2013) 613.
- The ANTARES Collaboration, the LIGO Scientific Collaboration and the Virgo Collaboration: S. Adrian- Martinez, et al. "A First Search for coincident Gravitational Waves and High Energy Neutrinos using LIGO, Virgo and ANTARES data from 2007". JCAP 1306 (2013) 008.

- The LIGO Scientific and the Virgo Collaborations: J. Abadie, et al. "Search for Gravitational Waves from Intermediate Mass Binary Black Holes". Phys. Rev. D 85 (2012) 102004.
- The LIGO Scientific and the Virgo Collaborations: J. Abadie, et al. "All-sky search for gravitational- wave bursts in the second LIGO-Virgo run". Phys. Rev. D 85 (2012) 122007.
- The LIGO Scientific and the Virgo Collaborations: J. Abadie, et al. "Upper limits on a stochastic gravitational-wave background using LIGO and Virgo interferometers at 600-1000 Hz". Phys. Rev. D 85 (2012) 122001.
- J. Aasi, et al. "The characterization of Virgo data and its impact on gravitational-wave searches". Class. Quantum Grav. 29 (2012) 15502.
- P.A. Evans, et al. "Swift follow-up observations of candidate gravitational-wave transient events". ApJS 203 (2012) 28.
- The LIGO Scientific Collaboration, Virgo Collaboration: J. Abadie, et al. "Search for gravitational waves associated with gamma-ray bursts during LIGO science run 6 and Virgo science runs 2 and 3". Astrophys. J. 760 (2012) 12.

Presentations

Invited Talks:

- " Searching for intermediate-mass black-hole binaries and measuring the neutron-star equation of state using advanced gravitational-wave detectors", CIT LIGO seminar, California Institute of Technology (Jan 2015).
- "Measuring the neutron-star equation-of-state using advanced gravitational-wave detectors", CIT LIGO seminar, California Institute of Technology (April 2014).

Contributed Talks:

- "On the feasibility of constraining the neutron star equation of state with advanced gravitational-wave detectors". 22nd Annual Midwest Relativity Meeting, Milwaukee, WI (October 2013)
- "Studying the effects of tidal corrections on parameter estimation". American Astronomical Society (AAS) Annual Meeting, Long Beach, CA (January 2013)
- "Studying the effects of tidal corrections on parameter estimation". 22nd Annual Midwest Relativity Meeting, Chicago, IL (September 2012)
- "Studying the effects of tidal corrections on parameter estimation?". Gravitational Wave Physics and Astronomy Workshop (GWPAW), Hannover, Germany (June 2012)
- "Continuous gravitational-wave sources from galactic neutron stars in the advanced detector era". 21st Annual Midwest Relativity Meeting, Urbana, IL (November 2011)
- "Continuous gravitational-wave sources from galactic neutron stars in the advanced detector era". 20th Annual Midwest Relativity Meeting, Guelph, ON, Canada (November 2010)

Contributed Poster Presentations:

- "A search for intermediate-mass black hole binaries using gstlal". LIGO Scientific Collaboration-Virgo Collaboration Meeting, Stanford, CA (August 2014)
- "Studying the effects of tidal corrections on parameter estimation". 20th International Conference on General Relativity and Gravitation and 10th Amaldi Conference on Gravitational Waves, Warsaw, Poland (July 2013)
- "Studying the effects of tidal corrections on parameter estimation". LIGO Scientific Collaboration-Virgo Collaboration March Meeting, Bethesda, MD (March 2013)
- "Continuous gravitational-wave sources from galactic neutron stars in the advanced detector era". 219th American Astronomical Society (AAS) January Meeting, Austin, TX (January 2012)